NASA Grant NGL-16-001-043

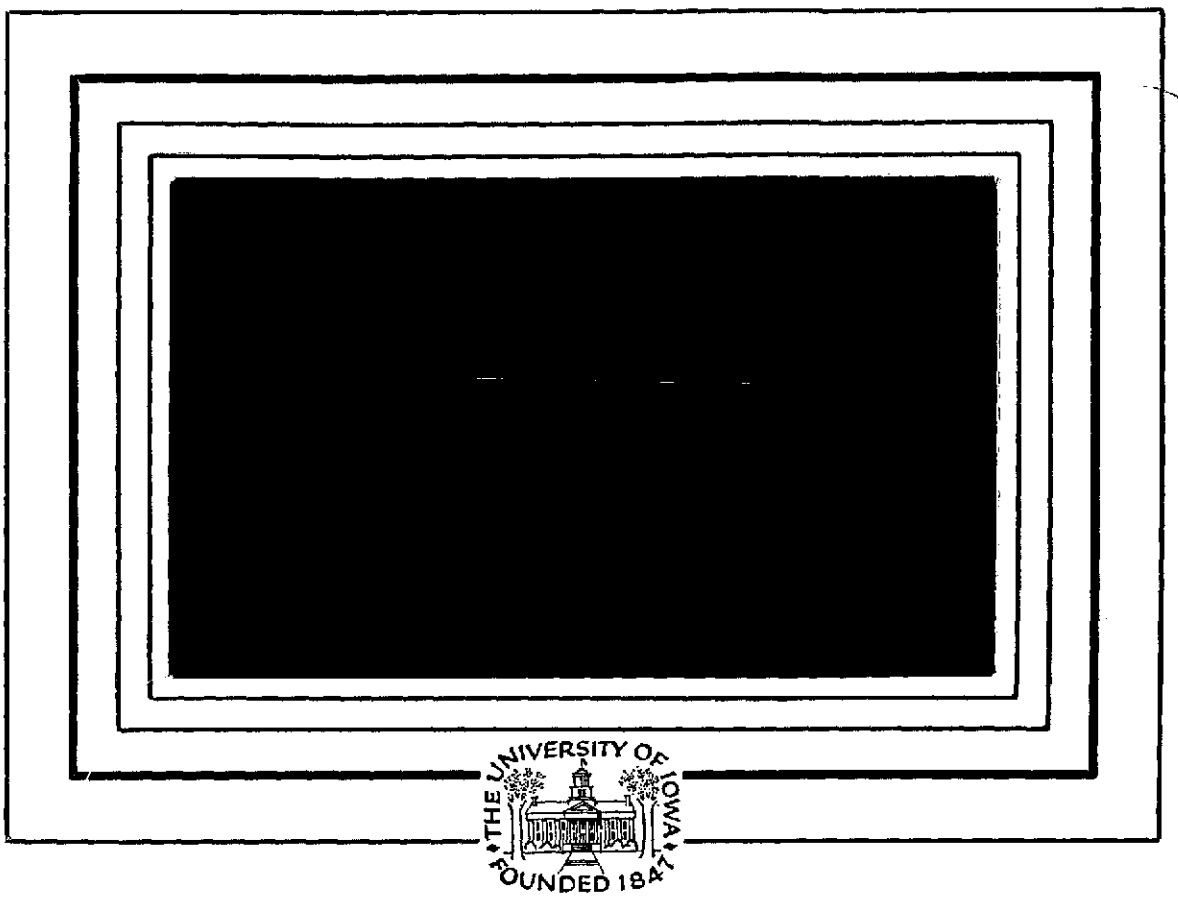

Department of Physics and Astronomy

THE UNIVERSITY OF IOWA

Iowa City, Iowa 52242

EXPERIMENTAL OBSERVATION OF LINEAR AND NONLINEAR ION ACOUSTIC PHENOMENA IN A CYLINDRICAL GEOMETRY

by

Thomas E. Romesser

A thesis submitted in partial fulfillment of the
requirements for the degree of Doctor of Philosophy
in the Department of Physics and Astronomy
in the Graduate College of
The University of Iowa

December, 1974

Thesis supervisor: Associate Professor Noah Hershkowitz

EXPERIMENTAL OBSERVATION OF LINEAR AND NONLINEAR ION ACOUSTIC PHENOMENA IN A CYLINDRICAL GEOMETRY

by

Thomas E. Romesser

An Abstract

Of a thesis submitted in partial fulfillment of the
requirements for the degree of Doctor of Philosophy
in the Department of Physics and Astronomy
in the Graduate College of
The University of Iowa

December, 1974

Thesis supervisor: Associate Professor Noah Hershkowitz

ABSTRACT

Ion acoustic phenomena are studied in a cylindrical geometry for two distinct cases. A large amplitude compressive pulse is seen to evolve into solitons. The evolution of these solitons and their dependence on initial conditions show a similarity to previous work on one dimensional solitons. Dimensionless scaling arguments are used to distinguish between the two cases. In the presence of a steady state uniform cylindrical beam, approximated by a ring in V_r, V_ϕ, an ion-ion beam instability is observed. This instability exists for a limited range of beam velocities and shows a marked similarity to the strictly one dimensional ion-ion beam instability. Solution of the appropriate dispersion relation shows agreement with the observed phenomenon.

Abstract approved: _____, Thesis supervisor

Associate Professor Noah Hershkowitz
Department of Physics and Astronomy

_____ date

Graduate College
The University of Iowa
Iowa City, Iowa

CERTIFICATE OF APPROVAL

PH.D. THESIS

This is to certify that the Ph.D. thesis of

Thomas E. Romesser

has been approved by the Examining Committee for the thesis requirement for the Doctor of Philosophy degree in the Department of Physics and Astronomy at the December, 1974 graduation.

Thesis committee: _____
Thesis supervisor

_____
Member

_____
Member

_____
Member

_____
Member

ACKNOWLEDGMENTS

The author wishes to thank his advisor Dr. Noah Hershkowitz for suggesting these experiments and providing extensive support and insight during their progress. Useful discussions with Dr. Georg Knorr and Dr. Christoph Goertz concerning the ion-ion beam instability were greatly appreciated and without their help the comparison with analytic theory would have been most difficult. The author wishes to thank Dr. David Montgomery for his continued interest and support during these experiments. A special note of thanks and appreciation for his talent goes to Alfred Scheller (Sr. ERD machinist) whose construction of much of the apparatus greatly helped the progress of these experiments. Last, but in no sense least, the author wishes to thank his family; his wife Mary Ann, for her patience and understanding during the duration of these experiments, and his son Michael, for inspiration.

This work was supported in part by NASA grant NGL 16-001-043.

ABSTRACT

Ion acoustic phenomena are studied in a cylindrical geometry for two distinct cases. A large amplitude compressive pulse is seen to evolve into solitons. The evolution of these solitons and their dependence on initial conditions show a similarity to previous work on one dimensional solitons. Dimensionless scaling arguments are used to distinguish between the two cases. In the presence of a steady state uniform cylindrical beam, approximated by a ring in V_r, V_ϕ, an ion-ion beam instability is observed. This instability exists for a limited range of beam velocities and shows a marked similarity to the strictly one dimensional ion-ion beam instability. Solution of the appropriate dispersion relation shows agreement with the observed phenomenon.

TABLE OF CONTENTS

LIST OF FIGURES

LIST OF FIGURES (cont.)

LIST OF FIGURES (cont.)

LIST OF FIGURES (cont.)

I. INTRODUCTION

The investigation of ion acoustic waves has been the subject of extensive study in recent years. With the invention of the double plasma (DP) device at UCLA [Taylor 1969A; Taylor 1972] new and wider areas of investigation were opened. Large amplitude planar waves can be efficiently launched in a plasma with variable electron to ion temperature ratio [Mackenzie 1971]. Steady state large diameter ion beams can also be injected into the plasma.

The initial work with a DP device was an investigation of collisionless electrostatic shocks [Taylor 1969B]. Ramp excitations of variable height and rise time were applied to the plasma. For large amplitude excitations ($\frac{\delta n}{n} \leq .3$) the initial ramp was observed to steepen and form a collisionless electrostatic shock. A small fraction of ions were reflected by the potential jump of the shock forming a double humped ion distribution in front of the shock.

These reflected ions represent a localized ion beam in the plasma. Stern and Decker [1971] report observation of an instability due to these reflected ions. A velocity gradient was established by injecting an ion beam from the target into the driver chamber.

When a large amplitude pulse is launched into the target chamber the reflected ions travel balistically from the point of reflection until the velocity gradient brings the precursors into resonance with the local ion acoustic velocity. A resonant transfer of energy from precursors to noise fluctuations results in the growth of the noise until it engulfs and destroys the original wave.

A similar study of turbulence associated with precursors of ion acoustic shocks by Means et al. [1973] attributes the observed turbulence, in their case, to the three dimensional nature of the instability. With no velocity gradient present there are modes oblique to the direction of the wave front which resonate with the reflected precursors. It is these off axis modes that result in the turbulence. Three qualitatively different effects were observed. For high electron to ion temperature ratios (T_e/T_i) and small amplitude, laminar shocks with no turbulence were observed. For moderate T_e/T_i ratios or amplitude turbulence, restricted to the region occupied by the precursor ions was observed. For low T_e/T_i or large amplitude, the turbulence engulfed the shock and destroyed its structure.

An investigation of the heating of an ion beam was made by Taylor and Coronitti [1972]. A uniform planar ion beam with velocity greater than twice the ion acoustic velocity was injected from the driver chamber into the target chamber. The ion-ion beam instability excited off-axis modes that propagated oblique

to the beam direction. The ion beam is seen to be heated until it forms a quasilinear plateau on the background ion distribution.

The evolution of non-linear compressive pulses that are governed by the Korteweg-de Vries equation was made possible by the DP device. Ikezi, Taylor and Baker [1970] investigated the properties of single solitons. The width, amplitude and velocity were shown to be consistent with the definition of solitons. The interaction of two solitons was also studied. Hershkowitz, Romesser and Montgomery [1972] compared the evolution of an initial condition into multiple solitons with the analytic theory. A similar report has been made by Ikezi [1973] in which both pulse and continuous wave initial conditions are treated.

The objective of the experiments reported in this dissertation was to investigate in a cylindrical geometry two kinds of ion acoustic phenomena. A study of the evolution of weakly non-linear compressive pulses in a cylindrical geometry was made to determine if solitons or soliton-like objects existed. Once their existence was determined a detailed comparison between planar and cylindrical solitons became possible. The second area of investigation is the ion-ion beam instability in a cylindrical geometry. For steady state radially ingoing beams an ion-ion beam instability is expected to occur. The dependence of the instability on beam velocity and beam density has been investigated and compared with the analytic theory for a linear instability.

II. EXPERIMENTAL APPARATUS

The experiments reported here were performed in the University of Iowa double plasma device. A modification was made to allow operation in a cylindrical geometry. The University of Iowa double plasma device (Fig. 1) consists of two aluminum cylinders (length 37 cm; diameter 38 cm) placed end to end but separated by an insulating ring. In each chamber 36 filaments are located symmetrically near the outside wall. Two cylindrical fine mesh screen (200 lines/inch) of radii 10 and 11 cm and length ~ 30 cm are mounted concentrically in one end of the device. Electrons emitted from the filaments which are biased at -40 volts with respect to the wall produce the plasma. The outer cylindrical screen is allowed to float causing it to charge up negatively preventing the flow of electrons between the inner and outer plasma. The inner cylindrical screen is grounded to help determine the plasma potential of the interior plasma. A shield was used to prevent line of sight paths between the outer (driver) plasma and the inner (target) plasma. Typical operating parameters are ion density (n_o) ~ 10^9 cm^{-3}, electron temperature (T_e) 1 - 3.0 eV, and an ion temperature (T_i) $\leq$ .2 eV [Hudis et al. 1968] at a pressure of 3×10^{-4} Torr.

Cooling coils are wrapped around the chamber and attached using Stycast 2850 FT epoxy.* The system is evacuated using a 4 inch oil diffusion pump to an ultimate base pressure of $\sim 5 \times 10^{-7}$ torr after pumping down. This assures us of negligible impurity concentration if data is not taken until the ultimate base pressure is reached.

There are two modes of operation for the DP device. If the potential of the driver chamber wall is raised with respect to the target chamber wall (ground) a uniform symmetric cylindrical beam is launched. The beam energy is adjustable, being a function of the applied potential difference. The beam is detected using a gridded energy analyzer as shown in Fig. 2. The front screen (200 lines/inch) is allowed to float and prevents electrons from entering the analyzer. The collector plate is biased at -67.5 volts to collect ion current. The voltage to the center grid is ramped with a sawtooth voltage. Only those particles with sufficient directed momentum to overcome the barrier represented by the second grid can be collected. This particular design gives directional resolution as will be seen later. From geometrical considerations the analyzer can detect particles in a cone of half angle 16°. The fields generated in the plasma will tend to broaden this. An energy resolution of .1-.2 eV is possible but deterioration of resolution occurs with use and exposure to the plasma. Figure 3 shows typical energy analyzer traces for

*Emerson and Cumings, Inc. Canton, Mass.

several beam energies. The signal represents the flux of particles with energy greater than Φ_s plotted versus Φ_s. If we then differentiate with respect to time (assuming Φ_s is linear with time) we recover the velocity distribution function f(v) plotted versus Φ_s. Figure 4 shows a differentiated energy analyzer trace. The temperature of the background ions is seen to be approximately .2 eV and a well defined beam is seen with energy 3.2 eV. The width of the beam appears slightly wider than that of the background ions. To determine the temperature, however, we must replot the data as f(v) versus v. Figure 5 shows the effect of doing this. The beam as expected will be much colder after being accelerated. To find the beam density we must look at the data that has been replotted as f(v) vs v.

Measurement of electron density is made using a Langmuir probe. To determine the density a large cylindrical probe (length 1 inch; diameter 1/8 inch) is used. For detection of waves a small wire biased above the plasma potential is used to detect electron saturation current.

Before looking at some typical data it must be noted that it is virtually impossible to form truly cylindrical screens. There is most probably a variation in the center of curvature of ~ .5 cm in the screen and for this reason no divergence is observed at r = 0. In addition there is a competition between damping and geometrical growth. Experimentally, they are found to be very closely balanced.

Upon application of a half sine wave pulse to the driver chamber a cylindrically symmetric ingoing wave is launched at r = 10 cm.

The wave propagates inward, converges at the center and emerges as a cylindrically symmetric outgoing wave. If we set the probe at a fixed position and look at the perturbed electron density as a function of time, we see first the ingoing wave and at a later time the wave after it has converged at the center and emerged as an outgoing wave. This is apparent in Figure 6 where the perturbed electron density as a function of time is shown for 1 cm intervals. The ion acoustic velocity as measured from this is 2.16×10^5 cm/sec which indicates an electron temperature of ~ 2.0 eV.

The presence of both ingoing and outgoing waves makes it difficult to make a detailed comparison between cylindrical and planar phenomenon. In order to make this comparison a major modification was made. The cylindrical screens were removed and a rectangular chamber was added to the end plate as in Fig. 7. A deformable separation screen that was adjustable from a plane to a half cylinder of radius 10 cm was used. Then, under nearly identical plasma conditions, a comparison of planar waves and half cylindrical waves was made.

Using a lock-in amplifier* it is possible to take an interferometer trace of a continuous wave excitation. Figure 8 shows the results for a planar separation screen with a frequency of 100 kHz. The lock-in amplifier detects the amplitude of the wave at a given phase with respect to the applied signal. For a plane wave we expect it to have the form:

---

*Par model HR-8.

$$A(r) = \text{Re}\, A_o e^{i(k_r + ik_i)r + i\phi}$$

$$= A_o e^{-k_i r}\, \text{Re}\, e^{i(k_r r + \phi)}$$

$$= A_o e^{-k_i r} \cos(k_r r + \phi)$$

For the case shown in Figure 8 we can measure k_r and k_i. From this we find $\frac{k_i}{k_r} = .044$. From this and assuming ion Landau dumping we can determine T_e/T_i to be approximately 13. This agrees with $T_e \sim 1$ eV and $T_i \sim .1$ eV.

A similar interferometer trace for the case of the separation screen deformed to a half cylinder of radius 10 cm is shown in Figure 9. Unlike the planar case, the wavelength is no longer constant for the cylindrical waves. The received amplitude for the cylindrical waves will be the sum of $J_o(kr)$ and $Y_o(kr)$.

$$A(r) = \text{Re}\{A_o[J_o(kr + \phi) + iY_o(kr + \phi)]\}$$

where $k = k_r + ik_i$. For the case $\phi = 0$ k_r can be expressed as $|k|re^{i\theta}$. Tables of this are available [Nat. Comp. Lab., 1947, 1950].

Figure 10 shows a computed interferometer trace for cylindrical waves using the values k_r and k_i as determined from the planar interferometer traces. The wave length is not constant in this case, though the disparity is much less than is measured from Fig. 9.

Data is taken using a Biomation 610B transient recorder which acts as a fast analog to digital converter. A description of this system is given in the Appendix.

III. SOLITONS

A. Theory

The properties of systems that support soliton solutions has generated a great deal of interest in recent years [Scott et al. 1973]. Extensive work in plasma physics has been carried out since Washimi and Taniuti [1966] showed that weakly non-linear ion acoustic waves are governed by the Korteweg-de Vries (KdV) equation:

$$\frac{\partial n}{\partial t} + n \frac{\partial n}{\partial x} + \frac{1}{2} \frac{\partial^3 n}{\partial x^3} = 0 \qquad (1)$$

Equation 1 is written in a frame moving at the ion acoustic velocity, n is the fractional density perturbation, x is the distance in the moving frame measured in electron Debye lengths $\left[\lambda_{De} = \left(\frac{kT}{4\pi n_o e^2}\right)^{1/2}\right]$ and t is measured in ion plasma periods $\left(\omega_{pi}^{-1} = \sqrt{\frac{m_i}{4\pi n_o e^2}}\right)$.

The asymptotic stationary solution corresponds to a superposition of spatially separated solitary pulses, solitons.

$$n(x, t) = \sum_j 2\epsilon_j \, \mathrm{Sech}^2\left[\left(\frac{\epsilon_j}{3}\right)^{1/2} (x - 2\epsilon_j c_s t/3)/\lambda_{De} + \phi_j\right]$$

c_s is the ion acoustic velocity $\sqrt{\frac{kT_e}{m_i}}$, ϵ_j and ϕ_j are constants

determined by the solution of an appropriate time independent Schrödinger equation with a potential well that is proportional to -1 times the initial spatial density perturbation [Hershkowitz et al. 1972]. The asymptotic stationary soliton solution arises from a competition between non-linearity and dispersion.

There are several properties of one dimensional solitons that can be used to identify them. Among them are: 1) Arbitrary positive (compressive) density perturbations evolve after sufficient time into a superposition of spatially separated solitons, or solitary pulses; 2) The number and amplitude of the solitons is determined by the solution of an appropriate time independent Schrödinger equation; 3) The soliton velocity is given by $[1 + \frac{1}{3} (\frac{\delta n}{n})_{max}]c_s$ where $(\frac{\delta n}{n})_{max}$ is the maximum density perturbation of the soliton; 4) The spatial width of the soliton, is proportional to $[(\frac{\delta n}{n})_{max}]^{-1/2}$ which implies that the product of the square of the maximum amplitude multiplied by the width is a constant; 5) Solitons retain their identity upon collision with other solitons. Experimentally these properties have been verified by Ikezi et al. [1970] and Hershkowitz et al. [1972].

Maxon and Viecelli [1974A] have reported the first work on solitons of dimensionality greater than one. They considered spherically symmetric perturbations and derived a modified KdV equation appropriate to a spherical geometry:

$$\frac{\partial n}{\partial t} + \frac{n}{t} + n\frac{\partial n}{\partial x} + \frac{1}{2}\frac{\partial^3 n}{\partial x^3} = 0$$

This equation is valid except in a region near the origin. A similar equation can be derived for cylindrical coordinates [Maxon and Viecelli 1974B] starting with the fluid equations appropriate for a cylindrical geometry with no z or ϕ dependence.

$$\frac{\partial n}{\partial t} + \frac{\partial}{\partial r}(nv) + \frac{nv}{r} = 0 \qquad \text{Continuity equation} \qquad (2)$$

$$\frac{\partial v}{\partial t} + v\frac{\partial v}{\partial r} = -\frac{\partial \Phi}{\partial r} \qquad \text{Momentum equation} \qquad (3)$$

$$\frac{\partial^2 \Phi}{\partial r^2} + \frac{1}{r}\frac{\partial \Phi}{\partial r} = e^{\Phi} - n \qquad \text{Poisson's equation} \qquad (4)$$

In these equations Φ is in units of $\frac{kT_e}{e}$, n in units of n_o, r in units of λ_{De}, t in units of ω_{pi}^{-1} and v is in units of c_s.

We now make the transformation to a frame moving inward at the ion acoustic velocity.

$$\xi = -\epsilon^{1/2}(r + t)$$

$$\eta = \epsilon^{3/2} t$$

where ϵ is a small parameter that will be used for expansion. The scaling used in the transformation is chosen to be the same as that of a soliton. We now expand the potential density and velocity in powers of ϵ.

$$n = 1 + \epsilon n^{(1)} + \epsilon^2 n^{(2)}$$

$$v = \epsilon v^{(1)} + \epsilon^2 v^{(2)}$$

$$\Phi = \epsilon \Phi^{(1)} + \epsilon^2 \Phi^{(2)}$$

The time and space derivatives transform to

$$\frac{\partial}{\partial t} = \frac{\partial \xi}{\partial t} \frac{\partial}{\partial \xi} + \frac{\partial \eta}{\partial \eta} \frac{\partial}{\partial \eta} = -\epsilon^{1/2} \frac{\partial}{\partial \xi} + \epsilon^{3/2} \frac{\partial}{\partial \eta}$$

$$\frac{\partial}{\partial r} = \frac{\partial \xi}{\partial r} \frac{\partial}{\partial \xi} + \frac{\partial \eta}{\partial \eta} \frac{\partial}{\partial \eta} = -\epsilon^{1/2} \frac{\partial}{\partial \xi}$$

From the transformation we find that

$$r = -\epsilon^{-3/2}(\epsilon\xi + \eta)$$

Equations 2, 3 and 4 then transform to the following equations respectively:

$$\epsilon^{5/2}\frac{\partial}{\partial\eta}[n^{(1)} + \epsilon n^{(2)}] - \epsilon^{3/2}\frac{\partial}{\partial\xi}[n^{(1)} + \epsilon n^{(2)}]$$

$$- \epsilon^{3/2}\frac{\partial}{\partial\xi}[1 + \epsilon n^{(1)} + \epsilon^2 n^{(2)}][v^{(1)} + \epsilon v^{(2)}]$$

$$- \frac{\epsilon^{5/2}[1 + \epsilon n^{(1)} + \epsilon^2 n^{(2)}][v^{(1)} + \epsilon v^{(2)}]}{\xi\epsilon + \eta} = 0 \qquad (5)$$

$$\epsilon^{5/2}\frac{\partial}{\partial\eta}[v^{(1)} + \epsilon v^{(2)}] - \epsilon^{3/2}\frac{\partial}{\partial\xi}[v^{(1)} + \epsilon v^{(2)}]$$

$$- \epsilon^{5/2}[v^{(1)} + \epsilon v^{(2)}]\frac{\partial}{\partial\xi}[v^{(1)} + \epsilon v^{(2)}]$$

$$= \epsilon^{3/2}\frac{\partial}{\partial\xi}[\Phi^{(1)} + \epsilon\Phi^{(2)}] \qquad (6)$$

$$\epsilon^2 \frac{\partial^2}{\partial \xi^2} [\Phi^{(1)} + \epsilon \Phi^{(2)}] + \frac{\epsilon^3}{(\epsilon\xi + n)} \frac{\partial}{\partial \xi} [\Phi^{(1)} + \epsilon \Phi^{(2)}]$$

$$= \epsilon \Phi^{(1)} + \epsilon^2 \Phi^{(2)} + \frac{\epsilon^2 \Phi^{(1)2}}{2} - \epsilon n^{(1)} - \epsilon^2 n^{(2)} \tag{7}$$

We can now collect terms of various orders of ϵ.

$O(\epsilon)$ from Eq. 6.

$$\Phi^{(1)} - n^{(1)} = 0$$

$O(\epsilon^{3/2})$

$$\frac{\partial n^{(1)}}{\partial \xi} + \frac{\partial v^{(1)}}{\partial \xi} = 0$$

$$\frac{\partial v^{(1)}}{\partial \xi} + \frac{\partial \Phi^{(1)}}{\partial \xi} = 0$$

for $n^{(1)}$, $v^{(1)}$, $\Phi^{(1)} \to 0$ as $|\xi| \to \infty$

Then we obtain

$$n^{(1)} + v^{(1)} = 0$$

$$v^{(1)} + \Phi^{(1)} = 0$$

$$\therefore \quad n^{(1)} = \Phi^{(1)} = -v^{(1)}$$

To find the differential equation governing $n^{(1)}$, $\Phi^{(1)}$ and $v^{(1)}$ we must go to higher order.

$O(\epsilon^2)$

$$\frac{\partial^2 \Phi^{(1)}}{\partial \xi^2} = \Phi^{(2)} + \frac{\Phi^{(1)^2}}{2} - n^{(2)} \tag{8}$$

To this point we have not had to account for contributions arising from terms with $\frac{1}{r}$ dependence. The $\frac{1}{r}$ factor gives rise to a factor of the form

$$\frac{\epsilon^{3/2}}{\epsilon\xi + \eta}$$

The order of this term depends upon the denominator. If $|\epsilon\xi| \ll |\eta|$

this is of $O(\epsilon^{3/2})$ while if $|\eta| \ll |\epsilon\xi|$ this is of $O(\epsilon^{1/2})$. The former will be assumed and its implications will be discussed later.

$O(\epsilon^{5/2})$

$$\frac{\partial n^{(1)}}{\partial \eta} - \frac{\partial n^{(2)}}{\partial \xi} - \frac{\partial}{\partial \xi}\left[n^{(1)}v^{(1)}\right] - \frac{\partial \xi}{\partial \xi}\left[v^{(2)}\right] - \frac{v^{(1)}}{\eta} = 0 \qquad (9)$$

$$- \frac{\partial v^{(2)}}{\partial \xi} + \frac{\partial v^{(1)}}{\partial \eta} - v^{(1)}\frac{\partial v^{(1)}}{\partial \xi} = \frac{\partial \Phi^{(2)}}{\partial \xi} \qquad (10)$$

Solving Eq. 8 for $n^{(2)}$ and Eq. 10 for $\frac{\partial v^{(2)}}{\partial \xi}$ and substituting these results into Eq. 9 we obtain:

$$\frac{\partial \Phi^{(1)}}{\partial \eta} + \Phi^{(1)}\frac{\partial \Phi^{(1)}}{\partial \xi} + \frac{\Phi^{(1)}}{2\eta} + \frac{1}{2}\frac{\partial^3 \Phi^{(1)}}{\partial \xi^3} = 0$$

which is the modified KdV equation appropriate for cylindrically symmetric ingoing perturbation.

In deriving this it was assumed that $|\epsilon\xi| \ll |\eta|$. To understand the implications of this we must consider how the initial condition is entered into the problem. The initial condition is centered at $\xi = 0$ in the moving frame,

$$\xi = -\epsilon^{1/2}(r_o + t_o) = 0$$

$$\therefore \quad r_o = -t_o$$

$$\eta_o = -\epsilon^{3/2} r_o$$

where r_o is the radius at which the initial perturbation is applied. The initial condition is then specified as $n(\xi, \eta_o)$. The initial time is negative and time increases as the pulse propagates inward. The time $\eta = 0$ at which $|\epsilon\xi| \ll |\eta|$ cannot possibly hold is the time for an ion acoustic wave to propagate to the origin where an expansion in orders of ϵ would not be valid in any case.

The value of ξ represents the distance traveled in the moving frame. The solitons have a velocity that is dependent upon the amplitude and in addition we expect an approximately $\frac{1}{\sqrt{r}}$ growth. Assuming this we can approximately describe the soliton velocity as:

$$v = A \left.\frac{\delta n}{n}\right|_o \left(\frac{r_o}{r_o - c_s t'}\right)^{1/2} c_s$$

where $t' = 0$, where $r = r_o$ and $\left.\frac{\delta n}{n}\right|_o$ is the soliton amplitude at

$r = r_o$. The constant A describes the detailed velocity amplitude dependence and is of order 1. The distance in the moving frame is then given by

$$\xi = A \frac{\delta n}{n}\Big|_o \left(\frac{r_o}{r_o - c_s t'} \right)^{1/2} c_s t'$$

The quantity η is given by

$$\eta = t' - t_o = t' - \frac{R_o}{c_s}$$

The relation

$$|\epsilon\xi| \ll |\eta|$$

then becomes

$$A \frac{\delta n}{n}\Big|_o \left(\frac{r_o}{r_o - c_s t'} \right)^{1/2} c_s t' \ll \frac{R_o}{c_s} - t'$$

We can now choose representative values for t' and evaluate the inequality. For $t' = \frac{r_o}{2c_s}$ which represents the time for an ingoing linear wave to propagate half the distance to the origin we obtain:

$$A \left.\frac{\delta n}{n}\right|_o \sqrt{2} \ll 1$$

which is true for moderate $\left.\frac{\delta n}{n}\right|_o$.

For $t' = \frac{3r_o}{4c_s}$

we obtain

$$A \left.\frac{\delta n}{n}\right|_o \ll \frac{1}{6}$$

Because of the presence of damping the criterion is less stringent, since a $\frac{1}{r}$ growth is not observed.

The evolution of a weakly non-linear compressive pulse in the cylindrically symmetric geometry should be governed by the derived equation. This equation differs from the equation appropriate to spherical geometry in the factor of 1/2 associated with the $\frac{\Phi}{\eta}$ term.

B. Presentation of Measurements

The propagation of low amplitude pulses in the fully symmetric geometry has already been noted. For low amplitude pulses the ingoing wave and outgoing wave are similar in shape and width to the applied pulse. As the amplitude is increased this is no longer true. Figure 11 shows the received signal detected at $r = 0.5$ cm as the height of the applied pulse is increased. For low

amplitudes a linear ion acoustic wave is launched. As the amplitude is increased the wave grows in amplitude, steepens and forms into an object that can be identified as a soliton [Hershkowitz and Romesser 1974]. For still higher applied voltages the soliton decreases in amplitude and a new faster pulse appears. This new pulse is a burst of particles, or a pseudowave [Alexeff et al. 1968], traveling balistically through the plasma with energy equal to the applied potential pulse. For pulse amplitudes less than $\sim \frac{kT_e}{e}$ no pseudowave is launched.

Figure 12 shows a comparison of the propagation of a linear $(\frac{\delta n}{n} < 1\%)$ ion acoustic wave and a large amplitude non-linear $(\frac{\delta n}{n} \sim 17\%)$ wave. At r = 9 cm for the linear pulse we see first in time an ingoing wave that closely resembles the applied half sine wave pulse, followed at a later time by a similar outgoing pulse. As the probe is moved closer to the center the ingoing and outgoing pulse appear closer in time and finally merge at r = .5 cm. At this point the received signal again closely resembles the applied half sine wave pulse. For the large amplitude pulse at r = 9 cm the ingoing wave again closely resembles a half sine wave pulse. The outgoing wave which has had a longer time to evolve has evolved into what can be identified as 3 solitons. The evolution into these solitons is shown in the remaining traces. The increased velocity with respect to an ion acoustic wave is evident from the trace at r = 0.5 cm. The average velocity of the largest ingoing soliton is found to be approximately 1.17 c_s.

The probe was left in one position and the width of the applied pulse varied to determine if the number of solitons was dependent upon the applied pulse width. Fig. 13 shows the received signal at .5 cm and at r = 6 cm as the width is varied. For very narrow applied pulses a single soliton is observed. As the width is increased the first soliton increases in amplitude, speeds up and becomes narrower, a second soliton is seen to form. As the width is further increased the solitons continue to increase in amplitude and velocity. The second soliton merges with the first soliton and for very wide applied pulses no individual soliton is observable though the applied pulse has noticeably steepened. From the data shown for r = 0.5 cm an estimate of the product of the width of the soliton multiplied by the square root of the maximum amplitude shows it to be constant within 10% for the first 4 traces.

To determine the velocity amplitude relationship of the solitons, use was made of the fact that for very narrow applied pulses where a single soliton was found the soliton amplitude depends on the width of the applied pulse. The soliton amplitude can be varied from ~ 1% to 10% while maintaining essentially a single soliton. By following the propagation of the pulse the velocity can be determined. The propagation of the point of maximum amplitude was followed at 1 cm intervals for several soliton amplitudes. These results were least squares fit to give the results shown in Fig. 14. From this the velocity amplitude relationship for cylindrical solitons was found to be:

$$V = [1 + (1.05 \pm .2) \frac{\partial n}{n}|_{max}]c_s$$

The measurement of the velocity-amplitude relationship was simplified by the fact that over most of the ingoing trajectory the competition between geometrical growth and damping balanced (see Fig. 12). The soliton amplitude was essentially constant over the ingoing portion of the trajectory. For a purely ingoing linear wave we would expect a $(r_o/r)^{1/2}$ growth to occur. After accounting for this geometrical increase the ion acoustic pulse is calculated to have damped by a factor of 3 in propagating 9 cm. Making the same correction for the soliton in Fig. 12 we calculate a damping of a factor of 1.5 in traveling 9 cm. It must be remembered that the $(r_o/r)^{1/2}$ growth should hold only for the linear wave. The observed differences may be due to either differences in damping or differences from non-geometrical growth.

C. Discussion

We can summarize the properties of two dimensional solitons be stating that compressive density perturbations evolve into solitons. The number of solitons is determined by the width and amplitude of the initial density perturbation. Rarefactive density perturbations do not evolve into solitons. The solitons retain their identity after converging (colliding) at the center. All of these

agree with the well known properties of one dimensional solitons. In addition, we find that the soliton width multiplied by the square root of the soliton amplitude is approximately constant even though the amplitude, width and velocity are functions of time. The velocity is greater than the velocity of a corresponding one dimensional soliton. Both of these additional properties held for three dimensional solitons and the first also holds for one dimensional solitons.

It has been seen from these data that the properties of cylindrically symmetric solitons are remarkably similar to those of one dimensional solitons. Since no analytic theory exists for solutions of the modified KdV equation it was of great interest to investigate very carefully the detailed differences and similarities that occur.

It was very difficult to state when the propagating pulse had reached a final assymptotic state from which to evaluate properties. To overcome this the scaling properties of the ordinary KdV and then the modified KdV equation were investigated. This was first considered by Berezin and Karpman [1967].

The ordinary KdV equation is written as:

$$\frac{\partial n}{\partial t} + n \frac{\partial n}{\partial x} + \frac{1}{2} \frac{\partial^3 n}{\partial x^3} = 0$$

We wish to consider a class of initial conditions of the form

$$n(x, o) = \frac{\delta n}{n} f(\frac{x}{L})$$

where $\frac{\delta n}{n}$ is the amplitude of the initial perturbation and L is the width. $f(\lambda)$ is the functional form of the initial perturbation, e.g., square pulse, half sine wave pulse, etc. We now transform to a new set of variables where the transformation depends upon the initial condition according to

$$\tilde{x} = \frac{x}{L} \qquad \tilde{n} = \frac{n}{\delta n/n} \qquad \tilde{t} = \frac{t}{A}$$

Upon substituting into the KdV equation and simplifying we obtain

$$\frac{\partial \tilde{n}}{\partial \tilde{t}} + \frac{\delta n}{n} \frac{A}{L} \tilde{n} \frac{\partial \tilde{n}}{\partial \tilde{x}} + \frac{1}{2} \frac{A}{L^3} \frac{\partial^3 \tilde{n}}{\partial \tilde{x}^3} = 0$$

We have the freedom to choose A such that the coefficient of the second term vanishes. Upon simplifying we obtain

$$\frac{\partial \tilde{n}}{\partial \tilde{t}} + n \frac{\partial \tilde{n}}{\partial \tilde{x}} + \frac{1}{2\sigma^2} \frac{\partial^3 \tilde{n}}{\partial \tilde{x}^3} = 0 \qquad \text{where } \sigma^2 = L^2 \frac{\delta n}{n}$$

This was obtained using the following transformation

$$\tilde{x} = \frac{x}{L} \qquad \tilde{n} = \frac{n}{\delta n/n} \qquad \tilde{t} = \frac{\delta n}{n}\frac{t}{L}$$

Under the given transformation all initial conditions are transformed to a unit depth-unit width initial condition. Conditions with the same numerical values for σ evolve identically in the scaled coordinate system even though the evolution in the laboratory may be quite different. The number of solitons which evolve is determined by the numerical value of σ.

There exists a very wide variety of initial conditions for which the evolution in this scaled coordinate system is identical. The number of solitons in each case must be identical. It comes, then, as no real surprise that the dimensionless scaling of the time independent Schrödinger equation is the same as the scaling for the ordinary KdV equation. The verification of this scaling for planar excitations and measurements of the scaling for the cylindrical case is of interest and has not been considered before. In order to carry this out the deformable screen DP device was used.

The importance of the dimensionless scaling method is that it applies for all time and not only in an asymptotic region. The known analytic theory provides a connection between the initial condition and the final assymptotic state where the solitons are

spatially separated. The use of the dimensionless scaling method allows a direct comparison of soliton formation during the evolution from the initial condition. It is only needed to be able to identify a point in the evolution process that is easily identifiable for all initial conditions. This point in the evolution must also be able to be measured quite accurately. The point of emergence of the first soliton from the remaining envelope was chosen. As can be seen from Fig. 15 the formation of the local minimum between the first soliton and the remaining envelope of the initial condition occurs quite quickly. It is easily and accurately measured and appears for all initial conditions that evolve into solitons.

A large number of data points have been measured for a wide variety of initial conditions. The dimensionless time, τ, has been calculated as has the value of the dimensionless scaling parameter σ. These data are plotted in Fig. 16. The points represent both planar and cylindrical initial conditions. Both initial conditions are uniformly distributed, so no distinction is made between them. The points are distinguished by varying values of $\frac{\delta n}{n}\Big|_o$ of the initial condition. A systematic variation with $\frac{\delta n}{n}\Big|_o$ is seen. Larger amplitude initial conditions require a longer time to evolve in the scaled coordinates than an initial condition with identical value of σ but a smaller amplitude initial condition. While we do not know the analytic form to be expected we do expect the points to fall on a smooth curve if the scaling holds.

There are several sets of data that were taken for fixed initial condition amplitude and varying the width. These are shown in Fig. 17 where a differentiation is made between planar and cylindrical initial conditions. The same functional dependence is observed for all sets of planar data. The slope in each case is nearly identical but there is a consistent deviation with the initial value of $\frac{\delta n}{n}$. The cylindrical solitons, however, do not display the same functional dependence as is evident from the figure.

Differences do exist for the scaling of the modified KdV equation for a cylindrical geometry. The presence of $\frac{n}{2\eta}$ term does not affect the transformation used as it will scale the same as the $\frac{\partial n}{\partial \eta}$ term.

The presence of the $\frac{n}{2\eta}$ term, however, restricts the choice of initial conditions. For the ordinary KdV equation a transformation of the type

$$x' = x + a$$

$$t' = t + a$$

leaves the form of the equation invariant. We can then define $n(x, o)$ to be an initial condition centered at $x = 0$ at time $t = 0$. Making the substitution $x = \xi, t = \eta$ and using the above translation the form of the modified KdV equation becomes

$$\frac{\partial n}{\partial t'} + n \frac{\partial n}{\partial x'} + \frac{1}{2} \frac{\partial^3 n}{\partial x'^3} + \frac{n}{2(t' - a)} = 0$$

which is no longer the initial equation.

If we consider the class of initial conditions of the form

$$n(x, t_o) = \frac{\delta n}{n} f(\frac{x}{L})$$

the scaling then converts the modified KdV equation into

$$\frac{\partial n}{\partial t} + n \frac{\partial n}{\partial x} + \frac{1}{2\sigma^2} \frac{\partial^3 n}{\partial x^3} + \frac{n}{2t} = 0$$

The initial condition becomes a unit width-unit depth initial condition but since r scales as r/L it is situated at r_o/L. Figure 18 shows graphically the effect of the transformation for the ordinary KdV equation and the modified cylindrical KdV equation. In the scaled coordinate system the initial radius of the perturbation depends upon the width of the initial condition since the initial radius r_o, in Debeye lengths, is approximately constant for all data. The importance of the $\frac{n}{2t}$ term depends upon the initial radius in the scaled coordinate system. For this reason we would not expect

identical values of σ to exhibit the functional dependence as the width is varied to change σ. This is in agreement with the data in Fig. 17.

There exists a wide variety of equations that support soliton solutions, included in these are attempts to modify the ordinary KdV equation to include more realistic plasma effects. Tappert [1972] has included finite ion temperatures. Ott has included damping due to ion-neutral collisions [1971] and Ott and Sudan have treated Landau damping [1970].

Schamel [1973] has derived a modified KdV equation that allows for trapped electrons

$$\frac{\partial n}{\partial t} + b\, n^{1/2} \frac{\partial n}{\partial x} + \frac{1}{2} \frac{\partial^3 n}{\partial x^3} = 0$$

where b is a parameter that is the measure of electron trapping. Under the transformation

$$\tilde{x} = \frac{x}{L} \quad , \qquad \tilde{t} = \frac{\delta n / n^{1/2} t}{L} \quad , \qquad \tilde{n} = \frac{\delta n}{n}$$

we obtain

$$\frac{\partial \tilde{n}}{\partial \tilde{t}} + \tilde{n}^{1/2} \frac{\partial \tilde{n}}{\partial \tilde{x}} + \frac{1}{2\sigma^2} \frac{\partial^3 \tilde{n}}{\partial \tilde{x}^3} = 0$$

where

$$\sigma = [\frac{\delta n}{n}^{1/2} L^2]^{1/2}$$

Recomputing τ and σ and assuming b = constant does not significantly improve the results. The value for b is determined by the electron trapping. Only a weak dependence on $\frac{\delta n}{n}$ is allowed so the assumption of constant b is reasonable. This modified KdV appears insufficient to explain the deviations in Fig. 17.

Tran and Hirt [1974] have investigated the effect of a two species plasma deriving a modified KdV equation

$$2 \frac{\partial n}{\partial \eta} + \gamma n \frac{\partial n}{\partial \xi} + \frac{\partial^3 n}{\partial \xi^3} = 0$$

The value of γ is a very sensitive function of the relative concentration and mass ratio of the second species which can arise from impurities in the plasma. A 2% concentration of hydrogen in an argon plasma changes γ from 1 to .067. The dimensionless time and scaling parameter appropriate to the equation are:

$$\tau = \frac{\gamma \ \delta n/n \ t}{L} \qquad \sigma = [\gamma \ \delta n/n \ L^2]^{1/2}$$

Both τ and σ are functions of γ. One could attempt to explain the systematic deviation with $\frac{\delta n}{n}$ in Fig. 17 from this. It would not be consistent with the manner in which the experiment was performed however. Much of the data was taken with identical plasma and vacuum conditions. Increasing the amplitude and decreasing the width to obtain the same value of σ yielded a different dimensionless time for the evolution. Several measurements were taken within a short time interval.

If we choose the time scaling of the ordinary KdV equation and search for a functional form of σ that gives a smooth curve we obtain the results shown in Fig. 19. The value for σ is found to be

$$\sigma = [(\frac{\delta n}{n})^{-3} L^2]^{1/2}$$

No equation has been found that will yield this scaling. It may be necessary to change the scaling of both σ and τ.

IV. CYLINDRICAL ION-ION BEAM INSTABILITY

A. Experimental Measurements

It has already been seen that by applying a DC potential between target and driver plasma a steady state radially ingoing ion beam can be established (Fig. 4). For a limited range of beam velocity a coherent ion-ion beam instability is produced [Hershkowitz et al. 1974]. This is the result of cylindrical standing waves resonating with ingoing and outgoing beams. This experiment differs from those in a conventional DP device in that the boundaries play a very important role. The inner grounded screen requires vanishing potential on its surface.

The instability is detected by a positively biased Langmuir probe which collects electron saturation current. The signal is then analyzed using a spectrum analyzer.* The power spectrum for various beam velocities is shown in Fig. 20. For beam velocities greater than those shown the instability abruptly ceases as it does for beam velocities slightly less than those shown. The beam velocities are determined by digitizing the energy analyzer for each beam velocity. The digitized traces for a given beam velocity are added 64 times to reduce the level of fluctuations due to the instability. The averaged traces are then least squares fit to the

---

*Tektronix 1L5 plug in unit.

sum of two Gaussians with the width restricted to be the same. A typical fit is shown in Fig. 21. In this manner the beam velocity can be accurately determined even in the region where the beam is not resolved.

The instability manifests itself as a series of discrete frequencies that are approximately harmonically related as was seen from the power spectrum. A simultaneous comparison of detected signals at different positions using the two probes showed the oscillations to be in phase everywhere. This suggests cylindrical standing waves. To verify this the power spectrum was observed at several radial positions. The results are shown in Fig. 22. The lowest mode amplitude decreases monotonically as the probe is moved from the center to the outside. The second mode, however, shows a node at r = 7 cm and an investigation of the third mode shows 2 nodes between the center and the outside. This further enforces the identification of the instability as cylindrical standing waves.

From Fig. 20 it is apparent that instability frequency depends upon beam velocity. A plot of this is shown in Fig. 23 where we see that the frequency is linearly proportional to beam velocity for the lowest 3 modes seen. For the lowest mode we obtain from Fig. 23

$$\omega = .66\ v_B k$$

Before attempting to compare these results with theory we must determine the distribution function appropriate for the beam. This is accomplished using two energy analyzers; one oriented in the radial direction and the other in the azimuthal direction. A beam is observable by the radial energy analyzer for all radial positions. The azimuthal analyzer can detect a beam in a region near the center of the chamber. The size of the region was seen to depend upon the energy of the beam. Figure 24 shows a comparison of radial and azimuthal energy analyzer traces for a beam of energy 6.0 eV. The change in amplitude of the background plasma as the radial analyzer approaches the cylindrical screen is due to depletion of the plasma in the region between the analyzer and the screen. This depletion arises from the blocking of ion trajectories by the energy analyzer. Ions that would normally pass through the region occupied by the analyzer and reflect from the region near the screen can no longer do so. The radial energy analyzer detects a beam for all radii while the azimuthal analyzer detects a well identified beam for radii less than 4 cm. If we decrease the beam energy the radial analyzer shows similar traces. For a beam of 3.0 eV the azimuthal analyzer detects a well established beam for radii less than 5 cm as can be seen from Fig. 25. For still smaller beam energies which appear as barely resolved the azimuthal and radial energy analyzers detect similar distribution functions for $r \leq 7.0$ cm.

When the beam is accelerated the width in energy remains constant. This implies that the ~~temperature~~ width in velocity space is drastically reduced. This allows one to approximate the beam by a delta function. For the observed distribution function we can approximate it by

$$f_B(v) = \frac{1}{2\pi v_B}\,\delta\,(v - v_B) \qquad v = (v_r^2 + v_\phi^2)^{1/2}$$

where we are in cylindrical coordinate velocity space.

The beam is represented by a ring of particles of energy E_B in velocity space. The particles enter the target plasma with energy E_B but the velocities are distributed over an angle. The envelope traced out by the angular spread over all points on the cylinder represents the boundary over which the ring distribution should hold. This is shown graphically in Fig. 26.

There are two possible causes of the angular spread of the beam as it enters the plasma. The incoming ions have a finite ion temperature of $\sim .2$ eV. The ratio v_B/c_i represents the tangent of the angle where 2θ is the angular spread, where $c_i = \sqrt{\frac{kT_i}{m_i}}$. For a two volt beam

$$v_B/c_i = \tan\theta = \sqrt{10}$$

For the system used we would expect the region to have a radius of 3 cm. A further increase in the angular spread can arise from the passage through and between the two fine mesh cylindrical screens. If a particle passes through the sheath surrounding one of the screen wires it will be attracted or repelled depending upon the potential of the wire. Conservation of angular momentum allows only those ions with small impact parameter or velocity to be captured by the wire. The particle will follow this perturbed orbit in the region between the screens and undergo another randomizing passage through the inner cylindrical screen. In both of these mechanisms the lower the beam velocity the greater the angular spread will be.

B. Discussion

In order to predict the instability and its dependence upon beam velocity the Vlasov equation in cylindrical coordinates was used:

$$\frac{\partial f}{\partial t} + v_r \frac{\partial f}{\partial r} + \frac{v_\phi}{r} \frac{\partial f}{\partial \phi} + \left(\frac{e}{m} E_r + \frac{v_\phi^2}{r} \right) \frac{\partial f}{\partial v_r} + \left(\frac{e}{m} E_\phi - \frac{v_r v_\phi}{r} \right) \frac{\partial f}{\partial v_\phi} = 0$$

We now look at the restrictions on the distribution functions for a stationary homogenous equilibrium by setting $\frac{\partial}{\partial t} = 0$, $\frac{\partial}{\partial x} = 0$, $E = 0$ to verify the restrictions will be compatible with the ring distribution function. We obtain

$$\frac{v_\phi}{r}\left(v_\phi \frac{\partial f_o}{\partial v_r} - v_r \frac{\partial f_o}{\partial v_\phi} \right) = 0$$

The solution to this requires that f_o be a function of $v = \sqrt{v_r^2 + v_\phi^2}$ only, i.e.

$$f_o(\bar{v}) = f_o(v) = f_o\left(\sqrt{v_r^2 + v_\phi^2}\right)$$

This restriction holds trivially for the background ion and electron Maxwellians. The ring distribution also satisfies this condition since it depends only on $\delta(v - v_B)$ where $v = \sqrt{v_r^2 + v_\phi^2}$. Under these conditions we have a stationary homogenous state, with no zero order electric field, about which we can perturb.

We have observed the ring distribution function to exist over a region the size of which is determined by the beam energy. The instabilities observed typically occur for beam energies of less than 2 eV. For these energies the ring distribution function is observed to hold in a region that extends to within 3 cm of the boundary.

We can project the ring distribution function onto one axis in velocity space to see if it corresponds to an unstable distribution unlike the shell distribution function which projects to a

stable distribution function. The ring distribution in cartesian coordinates can be represented as:

$$f_B(v) = \frac{1}{2\pi v_B}\,\delta(v - v_B) \qquad v = \sqrt{v_x^2 + v_y^2}$$

Integrating out the v_y dependence we obtain projection onto the v_x axis as

$$F_B(v_x) = \int_{-\infty}^{\infty} \frac{1}{2\pi v_B}\,\delta\left(\sqrt{v_x^2 + v_y^2} - v_B\right) dv_y$$

evaluating we obtain

$$F_B(v_x) = \frac{1}{2\pi}\,\frac{1}{\sqrt{v_B^2 - v_x^2}} \qquad \text{for } |v_x| < v_B$$

$$= 0 \qquad |v_x| > v_B$$

This is plotted in Fig. 27. For very large beam velocities $F_B'(\omega/k) = 0$ for low frequency oscillation so the system will be linearly stable. For very small v_B we again expect linear stability. For a range of v_B we expect the system to be linearly unstable.

To investigate this we perturb the plasma by writing

$$f(\vec{r}, \vec{v}, \vec{t}) = n_o f_o(v) + f(\vec{r}, \vec{v}, t) \quad .$$

Then

$$\frac{\partial f_1}{\partial t} + v \cdot \nabla f_1 - \frac{e}{m} \nabla \Phi \cdot \frac{\partial f_o}{\partial v} = 0$$

We can solve this by integrating along the characteristics from $t = 0$ to time t.

$$f_1(\vec{r}, \vec{v}, t) = \int_o^t \frac{e}{m} \nabla \Phi \frac{\partial f_o}{\partial v} \, d\tau$$

where the integral will follow the characteristics. Initially we will work in cartesian coordinates using plane waves as a complete set in which to expand. Here the characteristics are given by

$$x_o = x - v_x(t - \tau)$$

$$y_o = y - v_y(t - \tau)$$

if we expand $\Phi(\vec{r}, t)$ in plane waves and look at one mode.

$$\Phi(\vec{r}, t) = \Phi_o \quad e^{i(ax + by) - i\omega t}$$

then substituting we obtain

$$f_1(\vec{r}, \vec{v}, t) = \frac{ie}{m} \Phi(r, t) \int_o^t ds\, e^{-i(av_x + bv_y - \omega)s}$$

$$x \quad (av_x + bv_y) \frac{1}{v} \frac{\partial f_o}{\partial v} \qquad \text{where } s = t - \tau$$

letting $t \to \infty$ we have a contribution if $\omega_i > 0$ and then

$$f_1(\vec{r}, \vec{v}, t) = - \frac{ie}{m} \Phi(r, t) \frac{av_x + bv_y}{-i(av_x + bv_y - \omega)} \frac{1}{v} \frac{\partial f_o}{\partial v}$$

To make the connection to cylindrical geometry, we compute the first order density fluctuations.

$$n(r, t) = \int f_1 (\vec{r}, \vec{v}, t) d\vec{v}$$

substituting and using the identities

$$x = r \cos \theta \qquad y = r \sin \theta$$

$$v_x = v \cos \phi \qquad v_y = v \sin \phi$$

$$a = k \cos \alpha \qquad b = k \sin \alpha$$

we obtain

$$n(r, t) = \frac{e}{m} \Phi(r, t) \int v dv \int d\phi \frac{kv \cos (\phi - \alpha)}{kv \cos (\phi - \alpha) - \omega} \frac{1}{v} \frac{\partial f_o}{\partial v}$$

defining

$$G(\frac{\omega}{k}, f_o) = k^{-2} \int_o^\infty v dv \int_o^{2\pi} d\phi \frac{\cos \phi}{\cos \phi - \frac{\omega}{kv}} \frac{1}{v} \frac{\partial f_o}{\partial v}$$

we have

$$n(r, t) = \frac{e}{m} \Phi(r, t) k^2 G(\frac{\omega}{k}, f_o)$$

A specific form was previously chosen for $\Phi(r, t)$. We now choose Φ_o to depend on α according to:

$$\Phi_o = \frac{\Phi_\nu}{\pi} e^{i\nu\pi/2} e^{i\nu\alpha}$$

We can recover cylinder functions for the perturbed density by using the identity

$$Z_\nu(kr) = \frac{1}{\pi} \int_{\omega_o}^{\omega_1} d\omega \; e^{i(kr \cos \omega)} e^{i\nu(\omega - \pi/2)} e^{i\nu\phi} \quad .$$

The explicit cylinder function obtained depends upon the path chosen to evaluate the integral. For the boundary conditions of the experiment $\Phi = 0$ on the inner cylinder we obtain $\nu = 0$ and $kr = \alpha_{o\mu}$ where $\alpha_{o\mu}$ is the μth zero of the Bessel function $J_o(\rho)$. To obtain the dispersion relation we substitute the density

$$n(\tilde{r}, t) = \frac{e}{m} \Phi_o \, J_o(kr) k^2 G\left(\frac{\omega}{k}, f_o\right)$$

into Poisson's equation

$$\nabla^2 \Phi = - 4\pi \sum_j e_j n_j$$

which yields

$$D(k, \omega) = 1 - \sum_j \omega_{pj}^2 G_j \left(\frac{\omega}{k}, f_{oj}\right)$$

$$= 1 - \sum_j \omega_{pj}^2 k^2 \int_o^\infty v dv \int_o^{2\pi} d\theta \frac{kv \cos\theta}{kv \cos\theta - \omega} \frac{1}{v} \frac{\partial f_{oj}(v)}{\partial v} .$$

The terms for background electrons and ions can be reduced to derivaties of Fried-Conte functions

$$D(k, \omega) = 1 - \frac{1}{2} \frac{k_e^2}{k^2} Z'\left(\frac{\omega}{\sqrt{2}\, k c_e}\right) - \frac{1}{2}(1 - n_B) \frac{k_i^2}{k^2} Z'\left(\frac{\omega}{\sqrt{2}\, k c_i}\right)$$

$$- \frac{n_B \omega_{pi}^2}{k^2} \int_o^\infty v dv \int_o^{2\pi} d\theta \frac{kv \cos\theta}{kv \cos\theta - \omega} \frac{1}{v} \frac{\partial f_{oB}}{\partial v}$$

an explicit form for the beam contribution due to a delta function region velocity space can be calculated for

$$|v_B| < \left|\frac{\omega}{k}\right|$$

$$D(k, \omega) = 1 - \frac{1}{2}\frac{k_e^2}{k^2} Z'\left(\frac{\omega}{\sqrt{2}kc_e}\right) - \frac{1 - n_B}{2}\frac{k_i^2}{k^2} Z'\left(\frac{\omega}{\sqrt{2}kc_i}\right)$$

$$- n_B\omega_{pi}^2 \omega\left[\frac{1}{\left(\omega^2 - k^2 v_B^2\right)^{3/2}}\right]$$

For $|v_B| > |\frac{\omega}{k}|$ we must make an analytic continuation of the dispersion relation for real ω. The contribution would be zero otherwise. This is analogous to the deformation of the contour used to evaluate the Fried-Conte functions for $\gamma < 0$.

Using the UCSB (University of California at Sata Barbara) on-line computer system the dispersion relation with a fluid equation contribution for the ion and electron term has been solved by iteration. The value of k is held fixed and the iteration is performed for a wide range of beam velocities. This is repeated for several beam densities. Figure 28 shows a plot of ω vs v_B and γ vs v_B for the lowest mode with $n_B = .3$. A maximum in the growth rate is observed for a beam velocity of 1.4×10^5 cm/sec. The ion acoustic velocity is 1.5×10^5 cm/sec for this case. In the region of maximum growth rate the next part of the frequency is proportional to $v_B k$ with

$$\omega = .61\, v_B k$$

If we express the dependence of the instability frequency on beam velocity as

$$\omega = \alpha v_B k$$

we find the parameter α remains approximately constant as the beam density is changed. This is shown in Fig. 30. The experimental value of .66 falls well within the observed range of α.

V. CONCLUSION

In a cylindrical geometry compressive ingoing ion acoustic pulses have been seen to evolve into "cylindrical solitons". The properties of these cylindrical solitons have been found to be consistent with those of one dimensional solitons (previously predicted and observed) and three dimensional solitons (previously seen in numerical solutions). The number of solitons is determined in a manner similar to the one dimensional case. A detailed investigation of the evolution of both planar and cylindrical solitons showed that differences exist during the evolutionary phase. For planar solitons the scaling of the Korteweg-de Vries equation was found to be insufficient to explain the observed scaling. However, the scaling has the same functional form for all cases. Detailed scaling arguments were found to be difficult to apply to the evolution of cylindrical solitons.

An ion-ion beam instability was observed in the presence of steady state beams for a limited range of beam velocities. The beam was found to be a ring in velocity space. As the beam velocity was increased from zero there was an abrupt onset of the instability. The instability manifested itself as cylindrical standing waves. The frequency of the instability was seen to depend upon the beam velocity and an upper limit was found for the beam

velocity above which the instability was not observed. Numerical solution of the dispersion relation appropriate for the standing waves yielded good agreement with the observed instability.

Figure 1 Cylindrical double plasma device with two insulated concentric plasmas. The inner plasma is produced in the right half of the device. DC beams can be controlled by varying Φ_B. If Φ_B is pulse a wave can be launched.

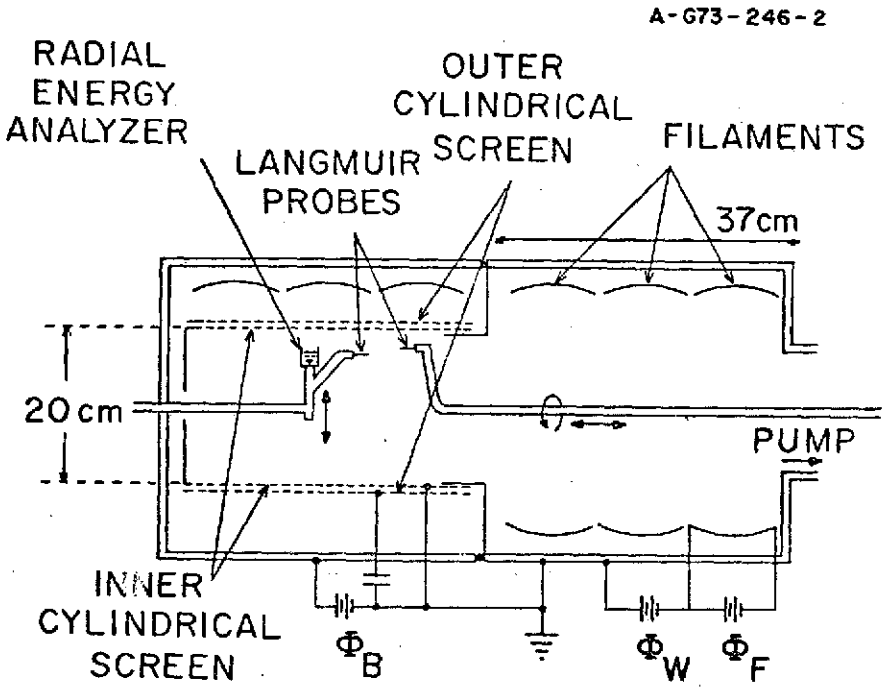

Φ_F – FILAMENT SUPPLY VOLTAGE

Φ_W – FILAMENT TO WALL VOLTAGE

Φ_B – APPLIED BIAS VOLTAGE

T_e = 1.0 e.V.

$T_i \lesssim .2$ e.V

$N_o = 10^8 - 10^9$ CM^{-3}

2×10^{-4} TORR

Figure 1

Figure 2 Schematic diagram of the ion energy analyzer. Two grids and a collector are used. The first grid is allowed to float negative. The second grid is ramped positive while the collector is biased at -65 volts. Ground shields are placed between the grids and the collector to prevent capacitive pickup between various elements.

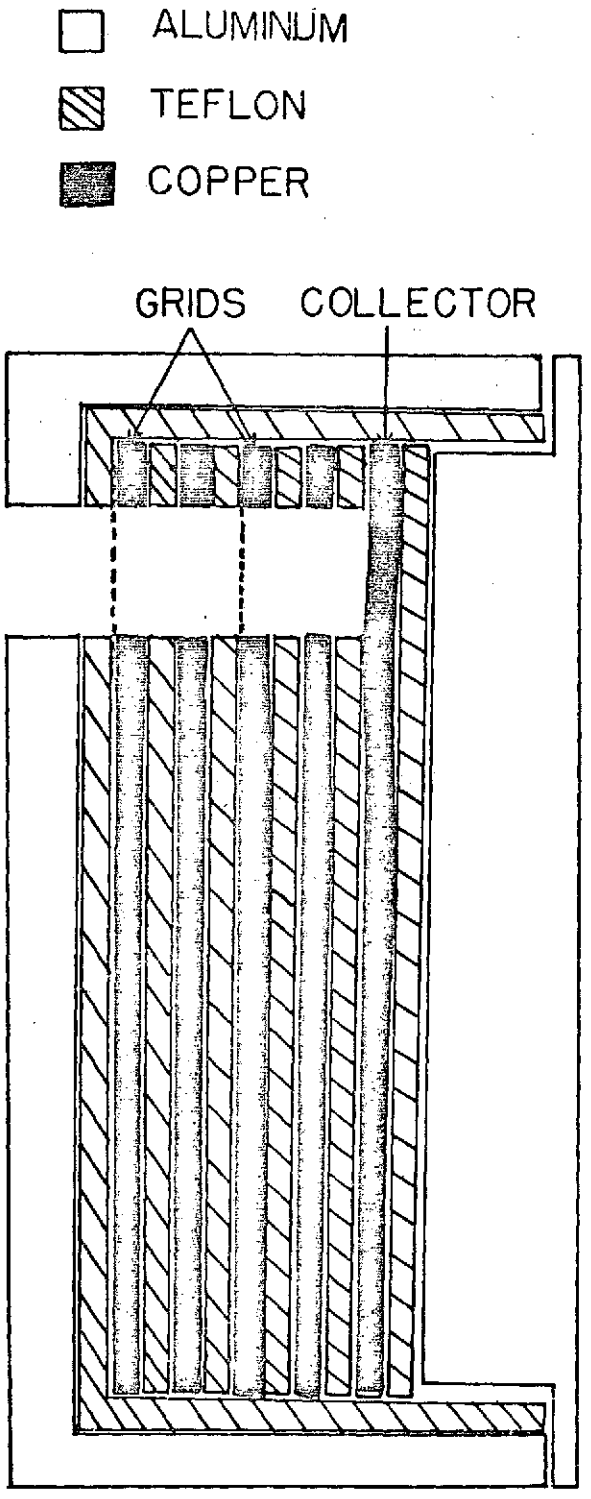

Figure 2

Figure 3 Current collected by the energy analyzer is displayed versus the voltage applied to the retarding grid for several different beam energies. The vertical scale is arbitrary and the horizontal scale is 2 volts per division.

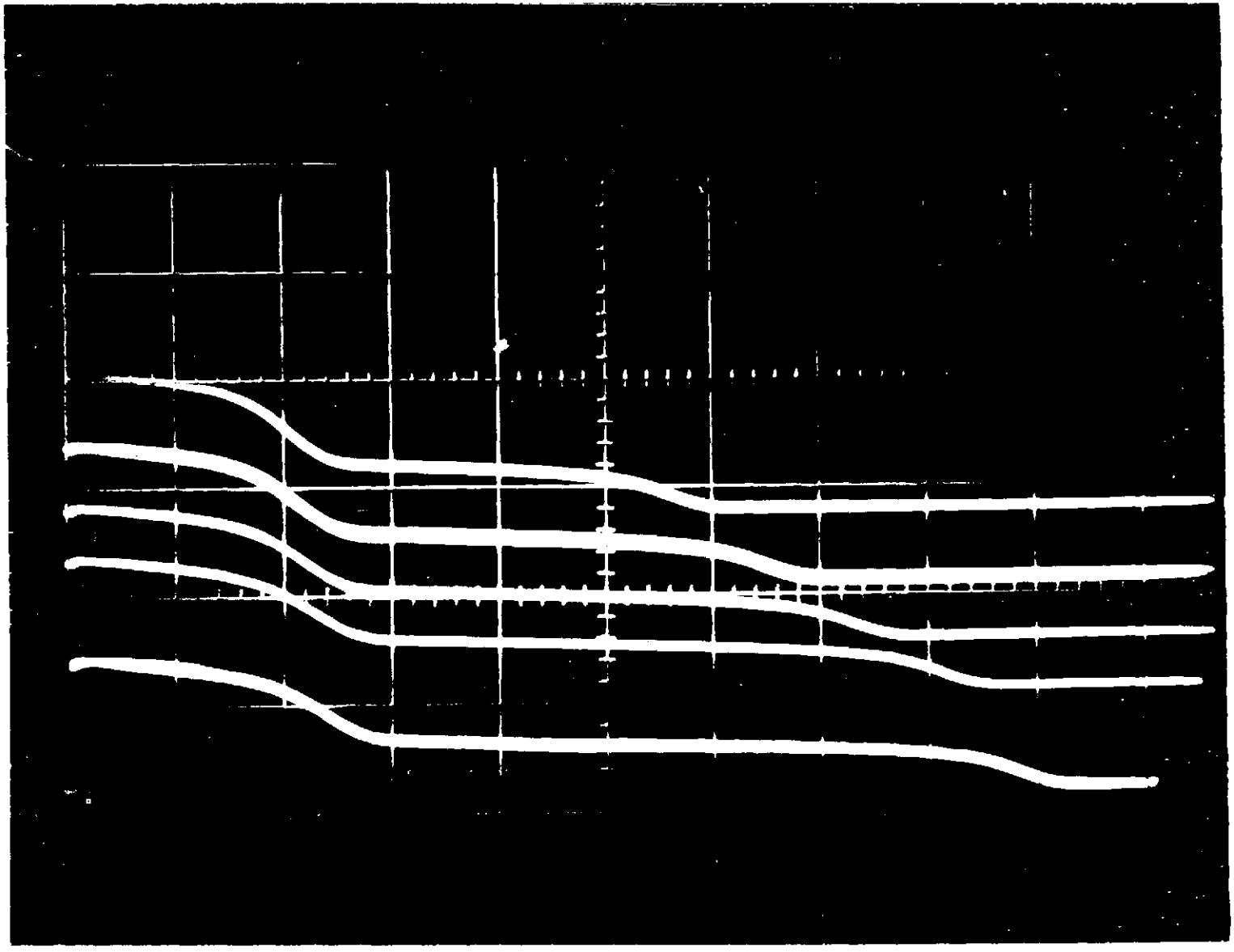

Figure 3

Figure 4 Power spectrum of the electron saturation current (top) and a differentiated energy analyzer trace (bottom). For the bottom trace the vertical scale represents the ion distribution function f(v) plotted versus the energy to the retarding grid (1 volt per division).

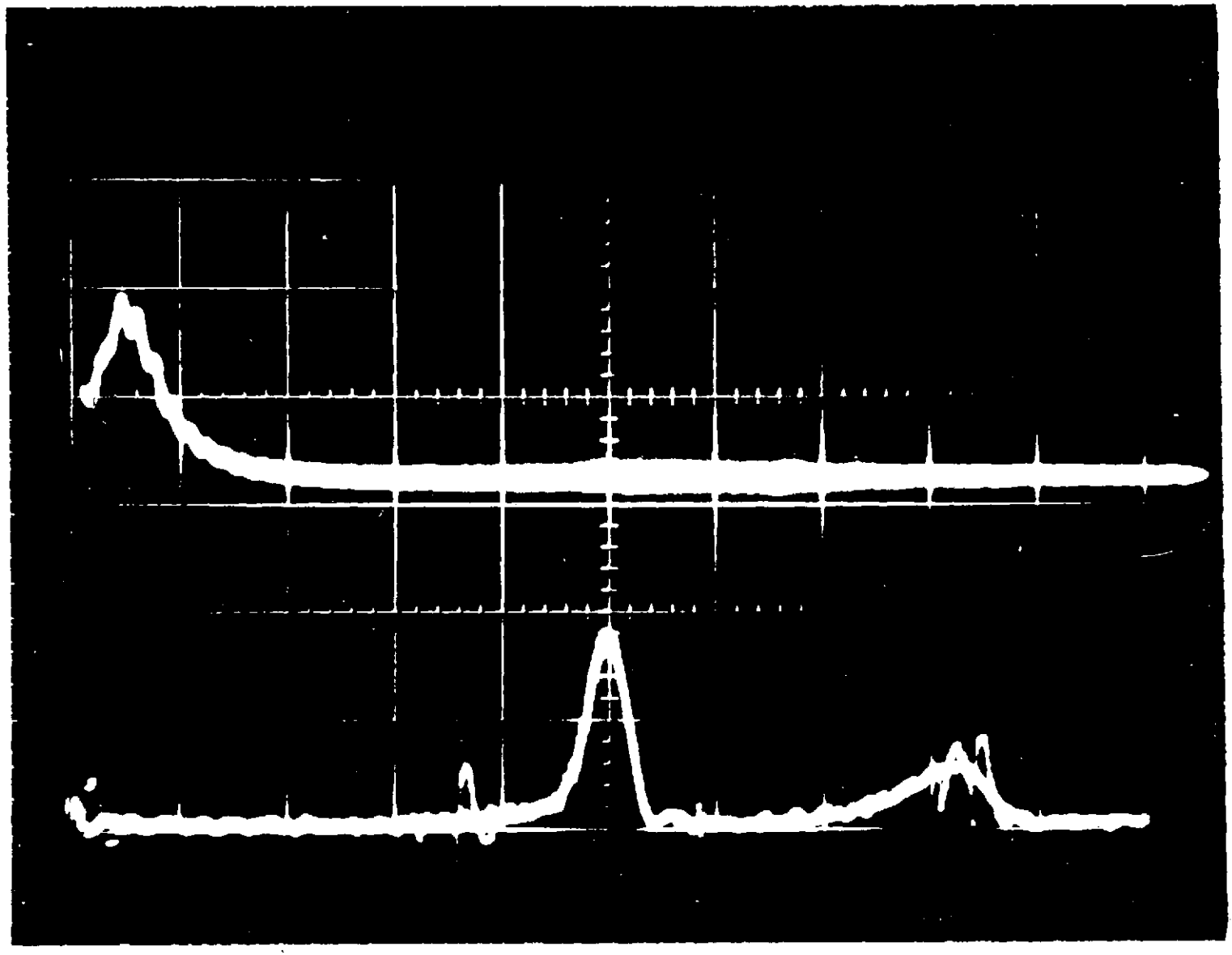

Figure 4

Figure 5 A comparison of the ion distribution function as seen by an energy analyzer when plotted versus the voltage to the retarding grid (top) and when plotted versus the ion velocity v (bottom). When plotted versus E the density and "apparent" temperature are equal. When replotted versus v we see that in fact the beam density is much less and the beam has effectively cooled by its acceleration.

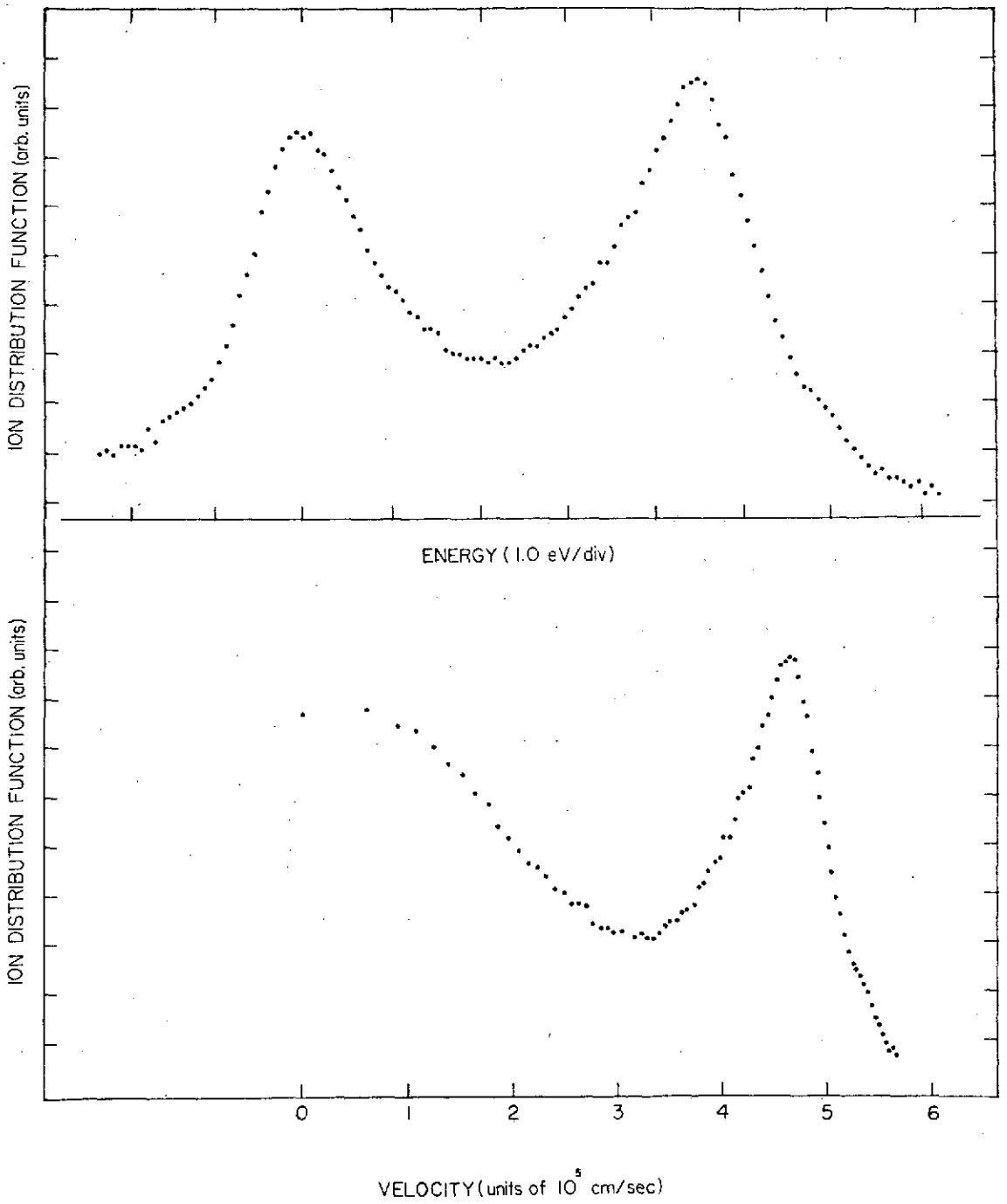
ION DISTRIBUTION FUNCTION (arb. units)
ENERGY (1.0 eV/div)
ION DISTRIBUTION FUNCTION (arb. units)
0
1
2
3
4
5
6
VELOCITY (units of 10^5 cm/sec)

Figure 5

Figure 6 Propagation of a low amplitude ion acoustic wave in a fully cylindrical geometry. The vertical scale is perturbed electron number density (arbitrary units) as a function of time (the horizontal). The width is 200 μsec. The top trace is taken at r = 9 cm and suceeding traces are at 1 cm intervals.

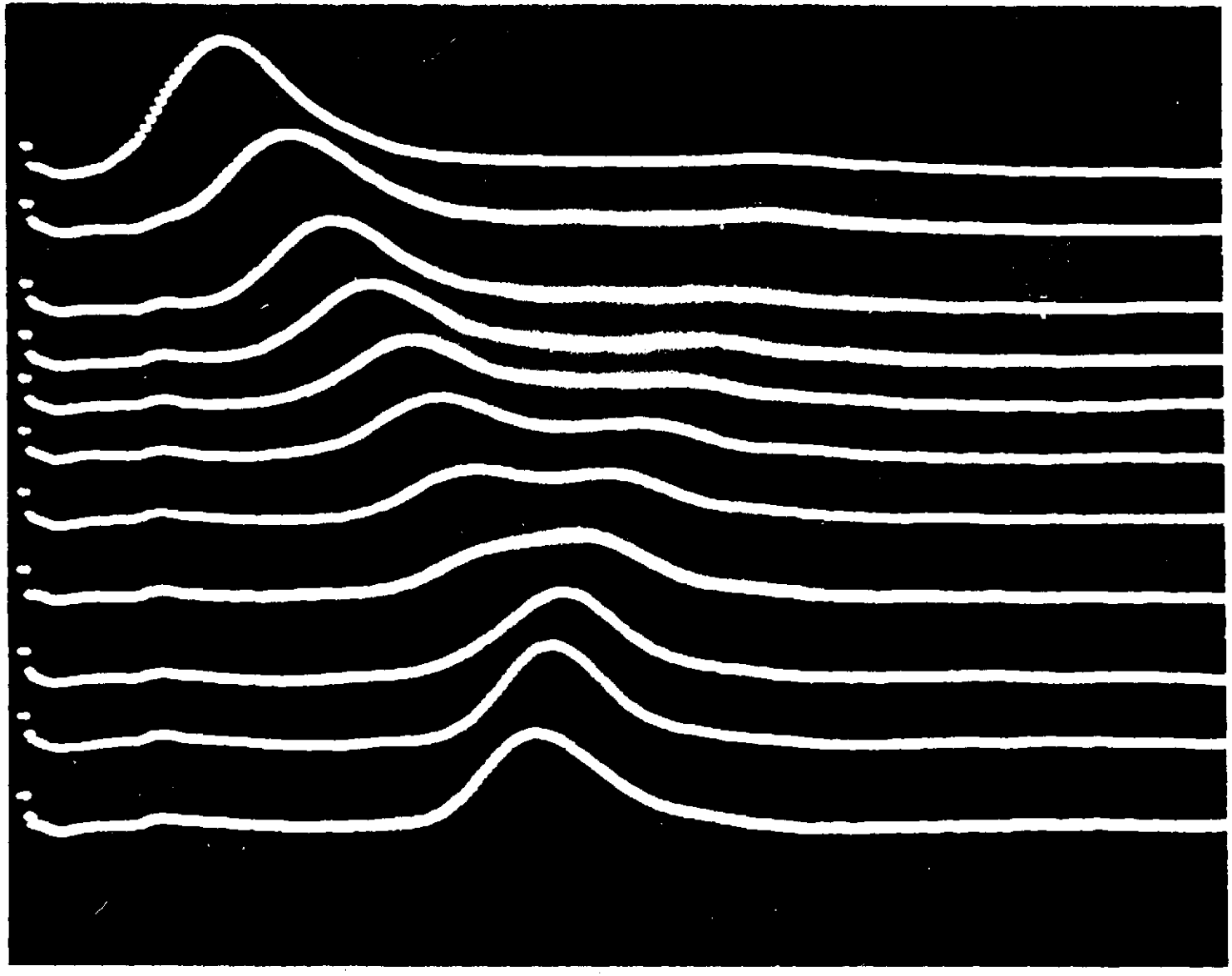

Figure 6

Figure 7 Schematic of the modified double plasma device. The separation screen shown here as a half cylinder is continuously deformable (from the exterior) to a plane separation screen. The discharge is maintained by filaments in both chambers as in a conventional DP device.

A-G74-505

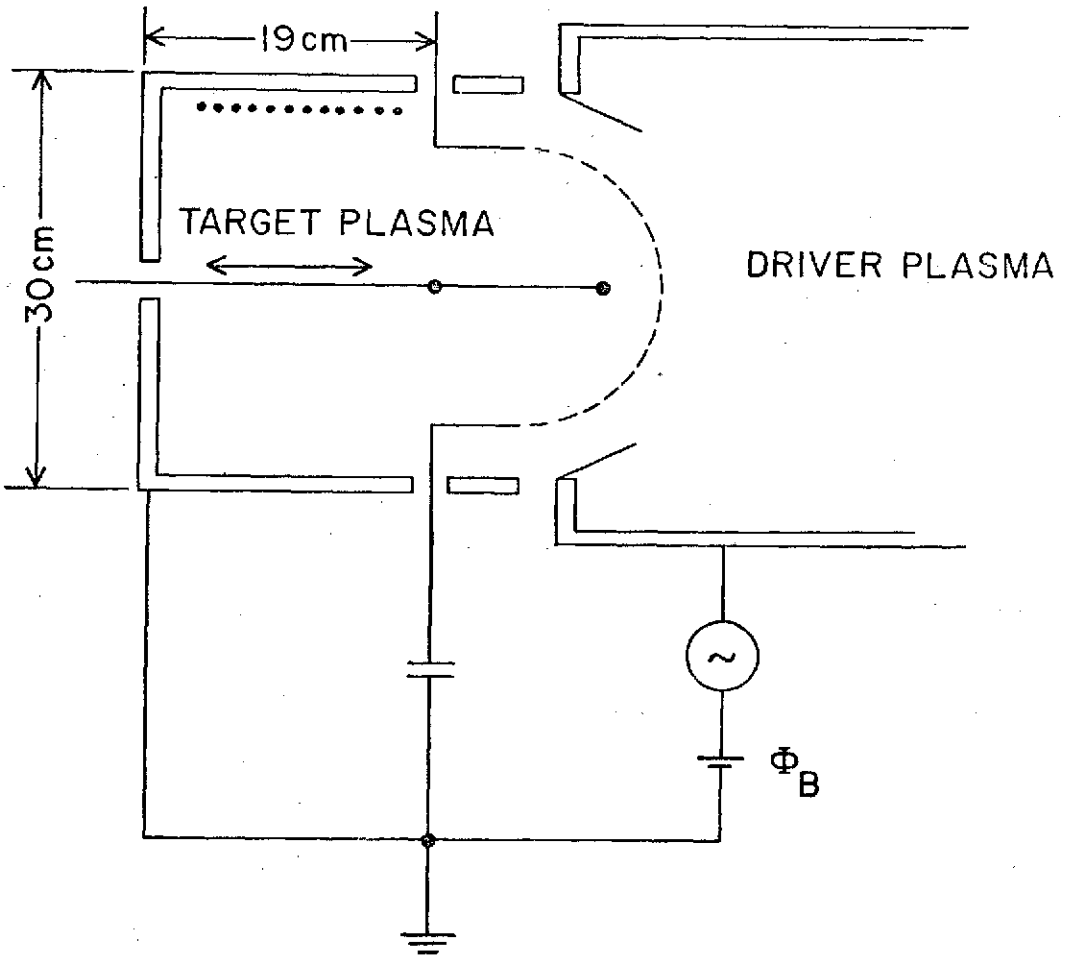

$T_e = 1 \rightarrow 3$ e.V.

$T_i \lesssim 0.2$ e.V.

$n_o = 10^8 - 10^9$ cm^{-3}

2×10^{-4} TORR

Figure 7

Figure 8 Interferometer trace for a planar separation screen. The wave amplitude with respect to a fixed phase of a reference signal is plotted as a function of distance.

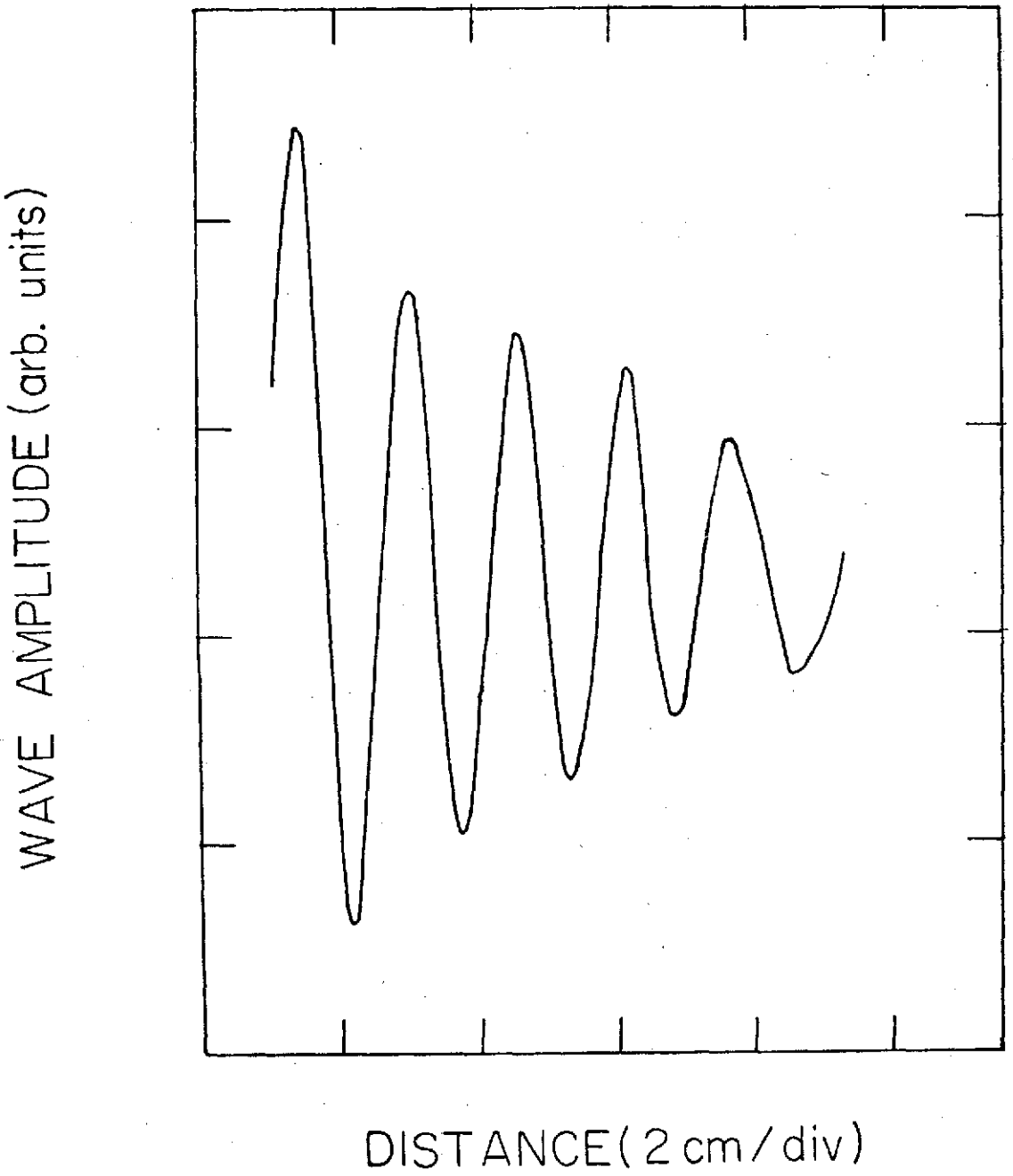

Figure 8

Figure 9 Interferometer trace for a half cylinder separation screen with radius 10 cm.

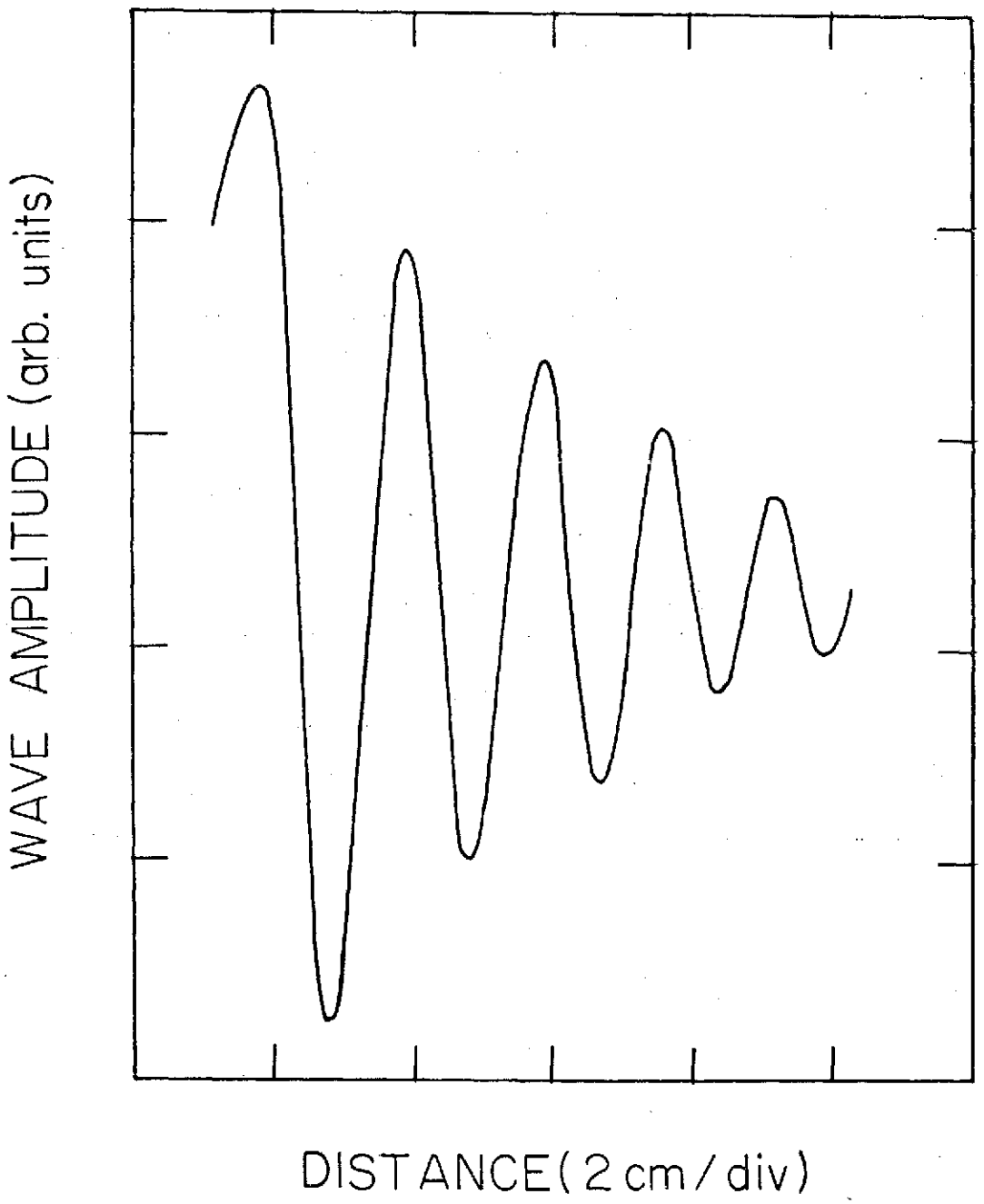

Figure 9

Figure 10 Computed interferometer trace for half cylindrical wave. The values of k_r, k_i from the planar case of Fig. 8 were used. The amplitude of the appropriate Hankel function was computed and plotted versus distance.

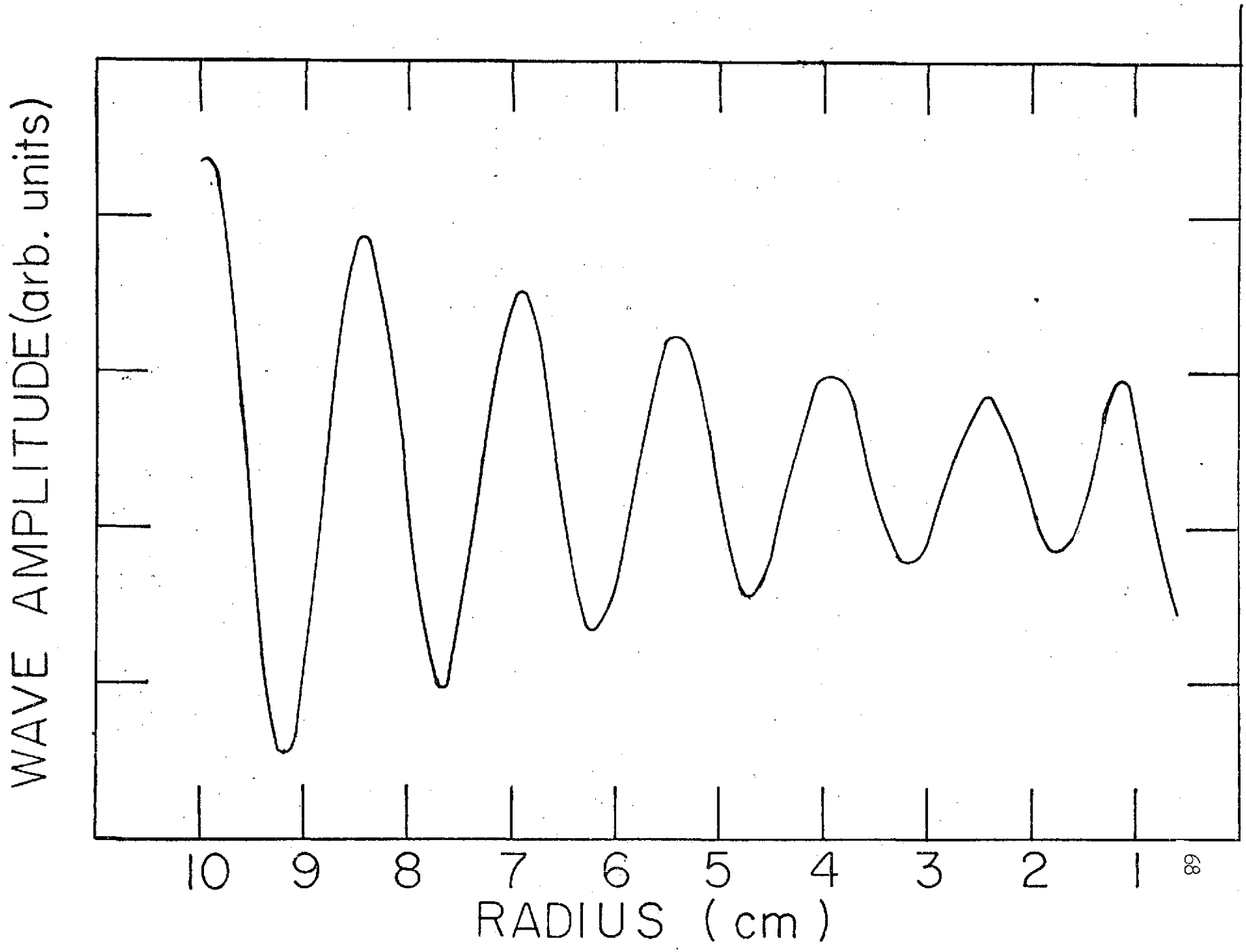

Figure 10

Figure 11 Electron density as a function of time at r = 0.5 cm, following the application of a half sine wave pulse. Signals are labeled by applied pulse amplitudes.

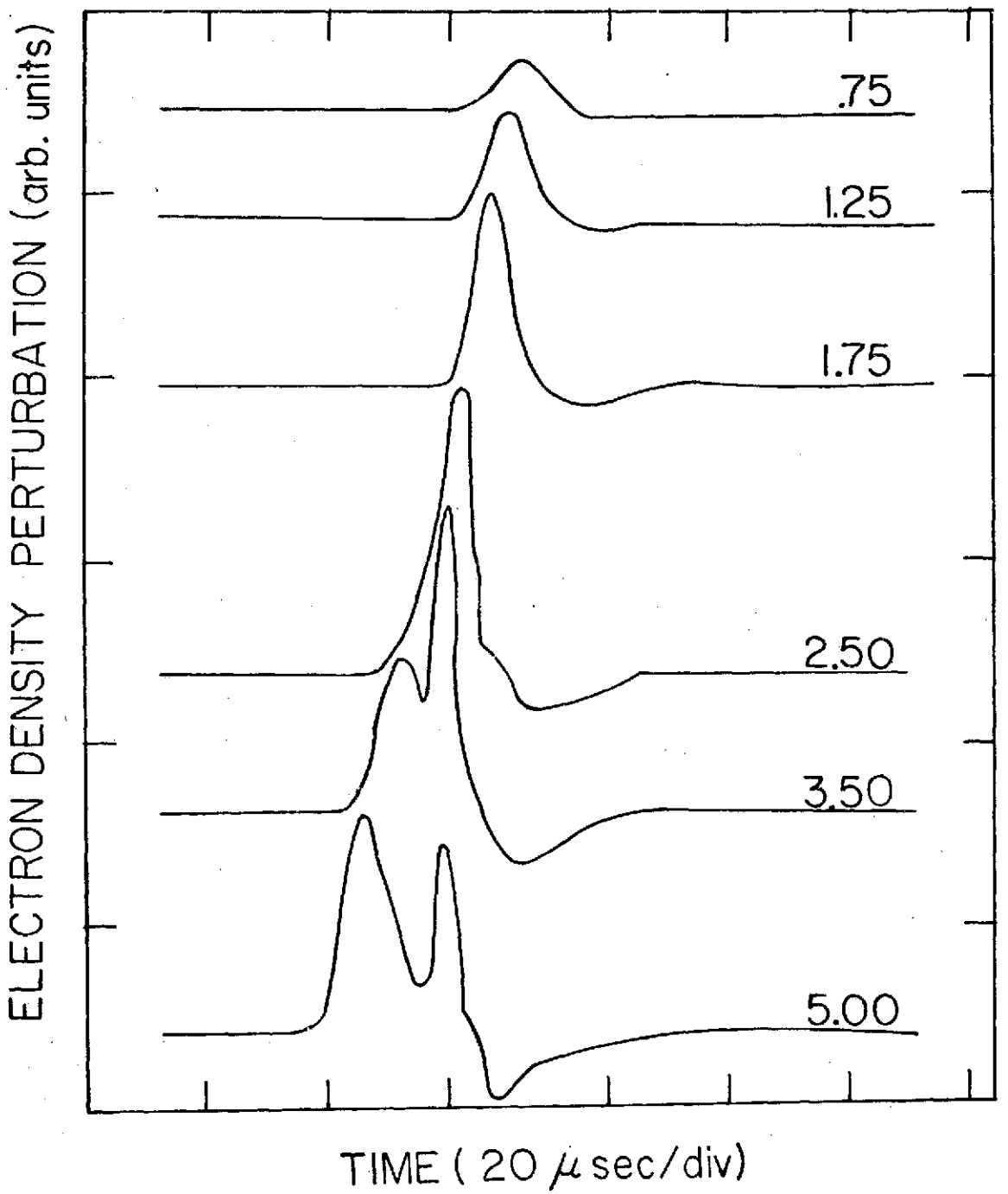
ELECTRON DENSITY PERTURBATION (arb. units)
.75
1.25
1.75
2.50
3.50
5.00
TIME (20 μ sec/div)

Figure 11

Figure 12 Perturbed electron number density as a function of time at several radial positions. The dotted traces represent linear ($\frac{\delta n}{n} < 1\%$) ion acoustic pulses (with amplitude adjust for comparison). The solid traces represent nonlinear pulses propagating, steepening and breaking into solitons.

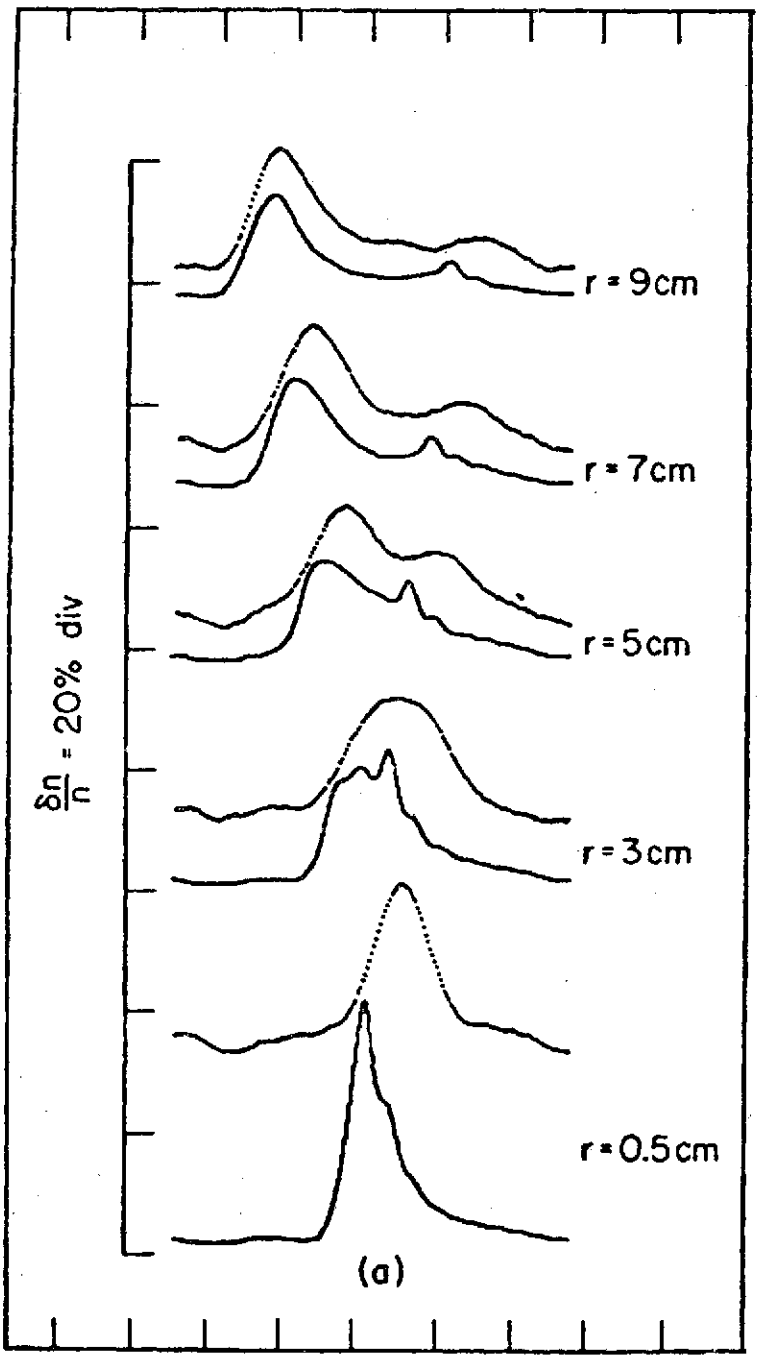

Figure 12

Figure 13 The left portion shows the perturbed electron number density detected at r = 0.5 cm versus time. The right hand side shows the received signal versus time at r = 6 cm. The traces are labeled by applied pulse widths.

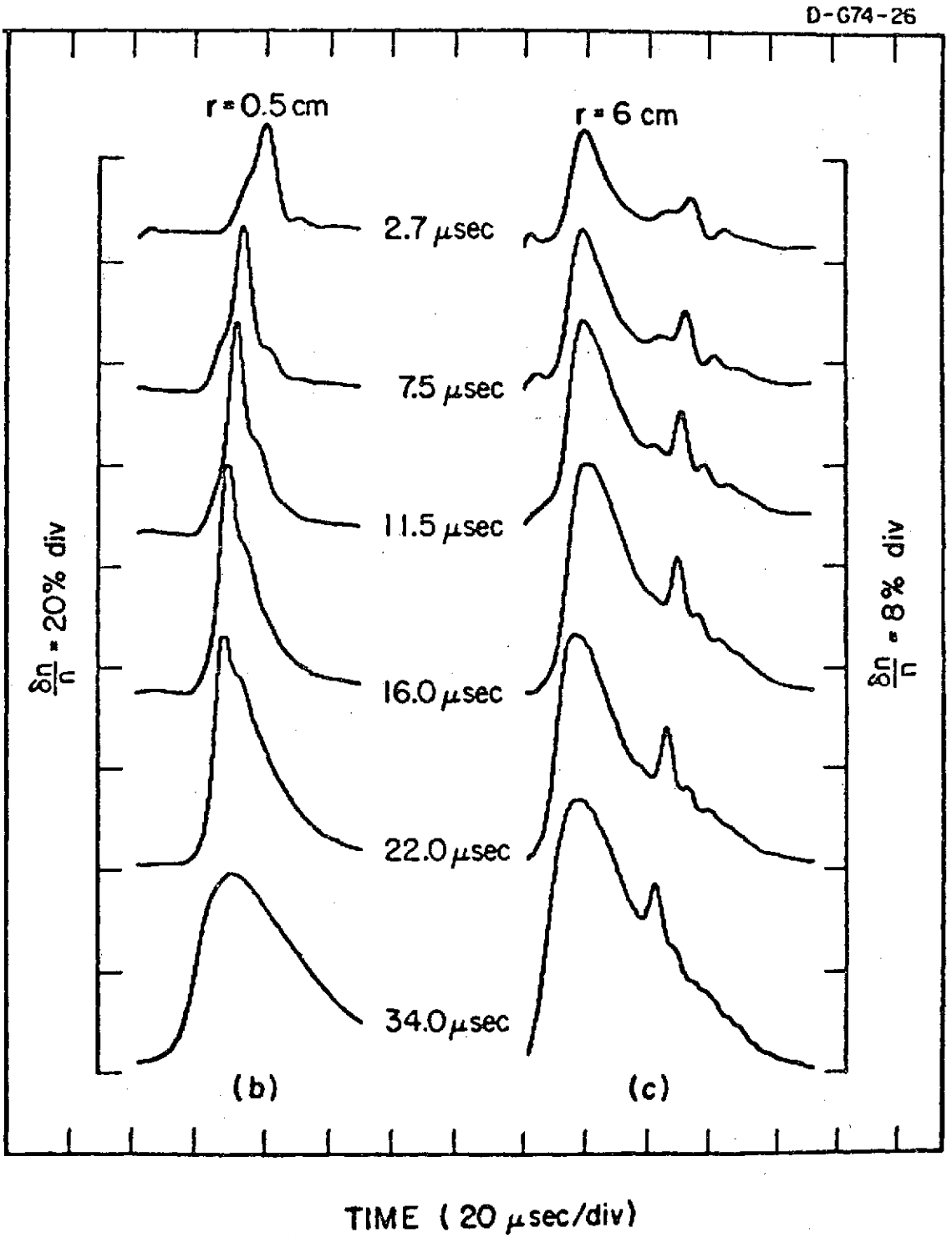
D-G74-26
r = 0.5 cm
r = 6 cm
2.7 μsec
7.5 μsec
11.5 μsec
16.0 μsec
22.0 μsec
34.0 μsec
δn/n = 20% div
δn/n = 8% div
(b)
(c)
TIME (20 μsec/div)

Figure 13

Figure 14 Velocity of a single soliton as a function of the maximum soliton amplitude.

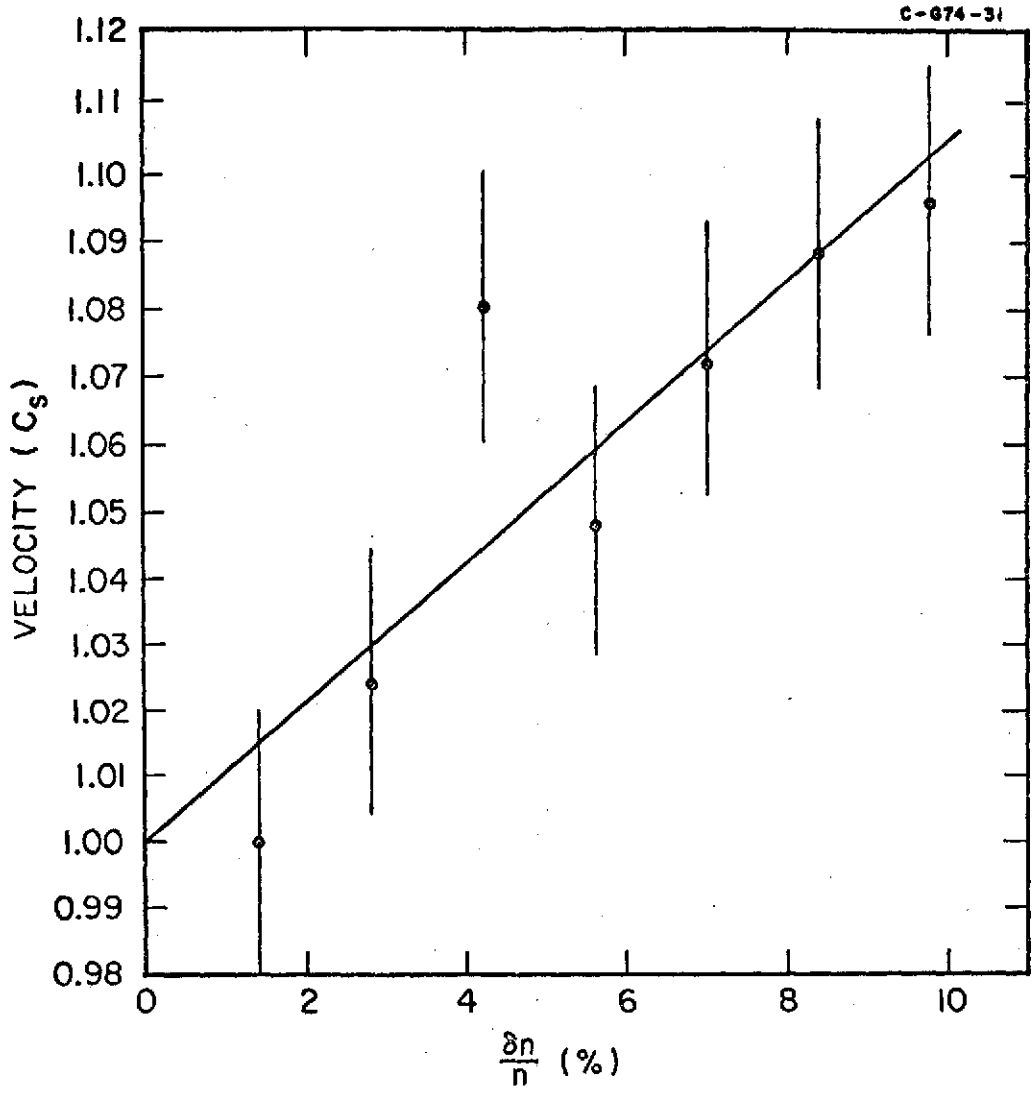
C-674-31
1.12
1.11
1.10
1.09
1.08
1.07
1.06
1.05
1.04
1.03
1.02
1.01
1.00
0.99
0.98
VELOCITY (C_s)
0
2
4
6
8
10
$\frac{\delta n}{n}$ (%)

Figure 14

Figure 15 Perturbed electron number density as a function of time at 1 cm intervals. A local minimum is seen to form between the first soliton and the remaining packet 8 cm from the screen.

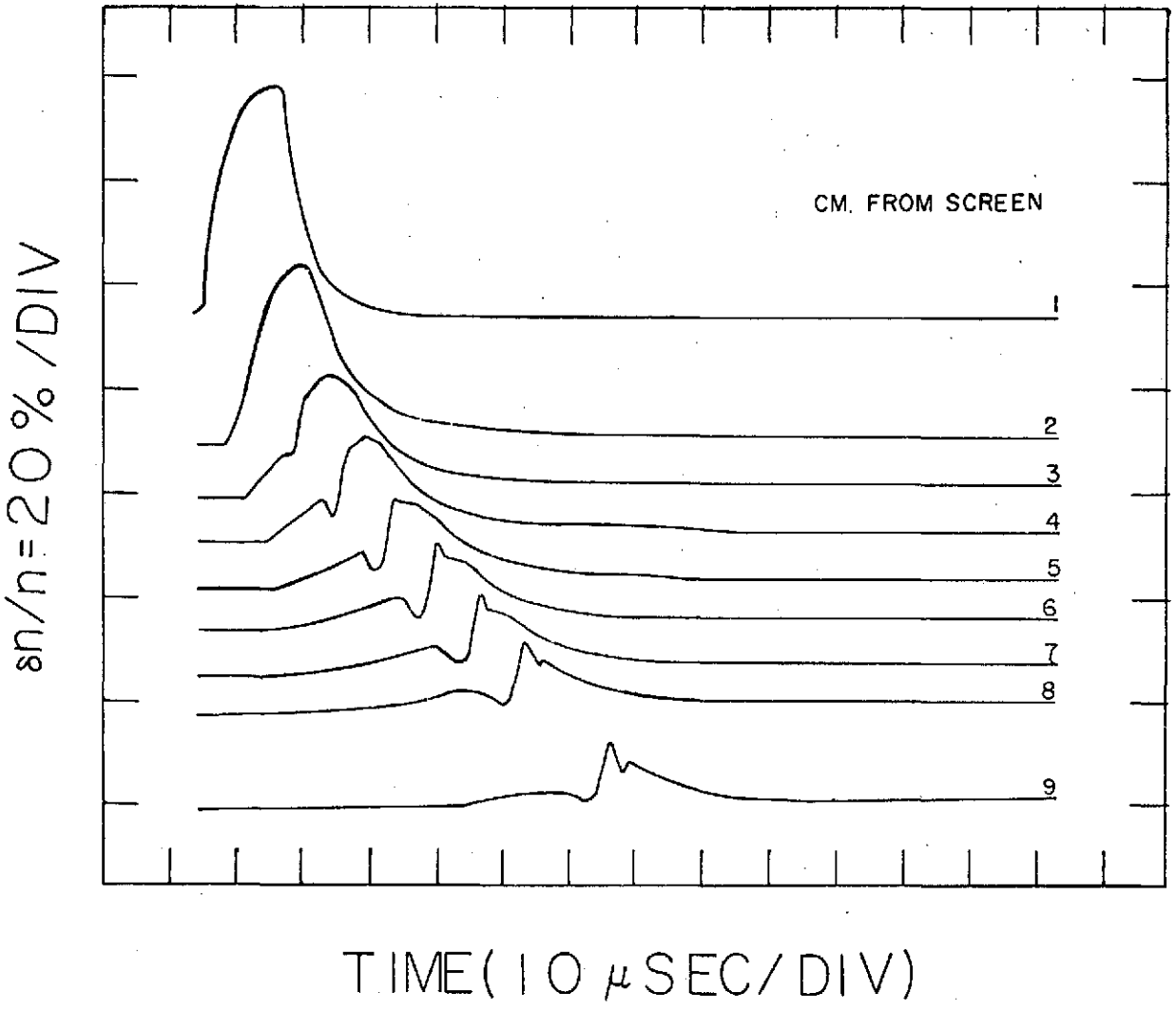

Figure 15

Figure 16 The dimensionless time $\tau = \frac{\delta n}{n} t/L$ plotted versus the dimensionless scaling parameter $\sigma = (\frac{\delta n}{n} L^2)^{1/2}$. Points for both planar and half cylindrical initial conditions are plotted and both are distributed uniformly over the graph.

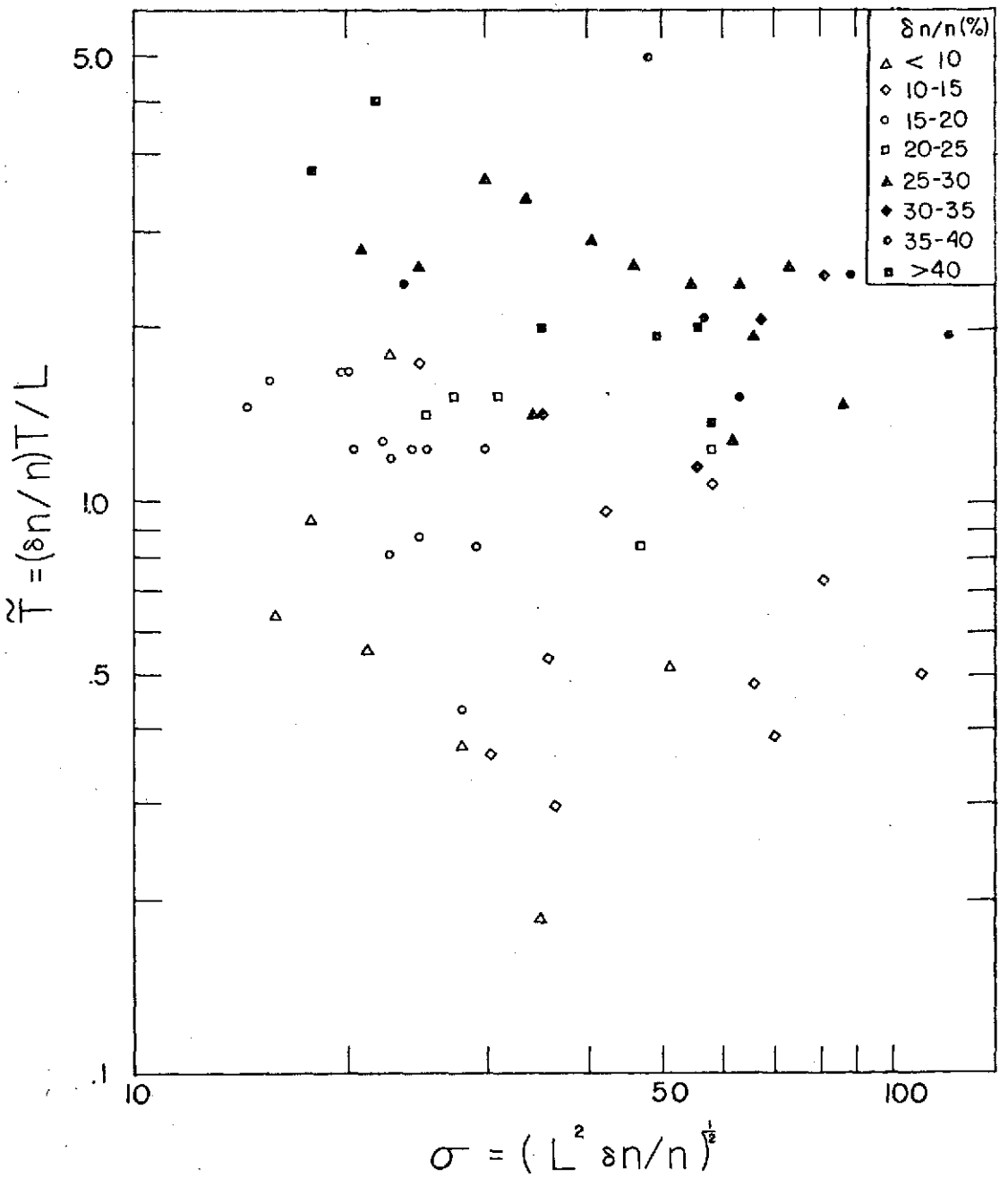
δn/n(%)
< 10
10-15
15-20
20-25
25-30
30-35
35-40
>40
5.0
1.0
.5
.1
10
50
100
$\tilde{T} = (\delta n/n)T/L$
$\sigma = (L^2 \delta n/n)^{\frac{1}{2}}$

Figure 16

Figure 17 The dimensionless time is plotted versus the dimensionless scaling parameter for several sets of data. In each set the initial amplitude is held constant and the width of the applied pulse is changed to vary the value of σ.

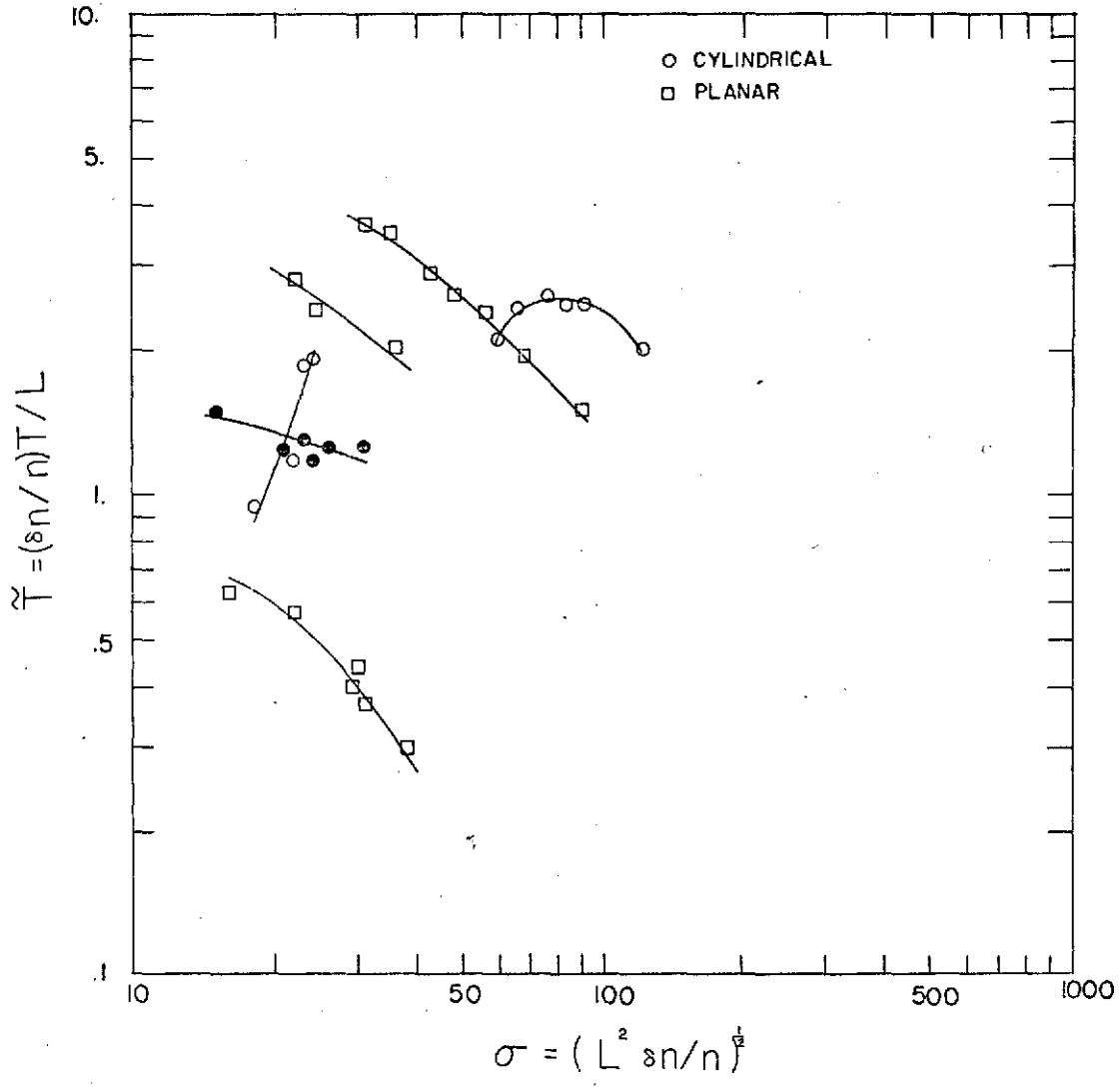
10.
5.
1.
.5
.1
10
50
100
500
1000
O CYLINDRICAL
□ PLANAR
$\tilde{T} = (\delta n/n)T/L$
$\sigma = (L^2 \delta n/n)^{\frac{1}{2}}$

Figure 17

Figure 18 The effect of the scaling transformation is shown graphically for both the ordinary KdV equation and the cylindrical KdV equation. For the ordinary KdV equation all initial conditions may be transformed to a unit width-unit depth initial condition at the origin. The cylindrical KdV equation, however, transforms to a unit width-unit depth initial condition located at a radius determined by the initial radius in the lab and the width of the applied pulse.

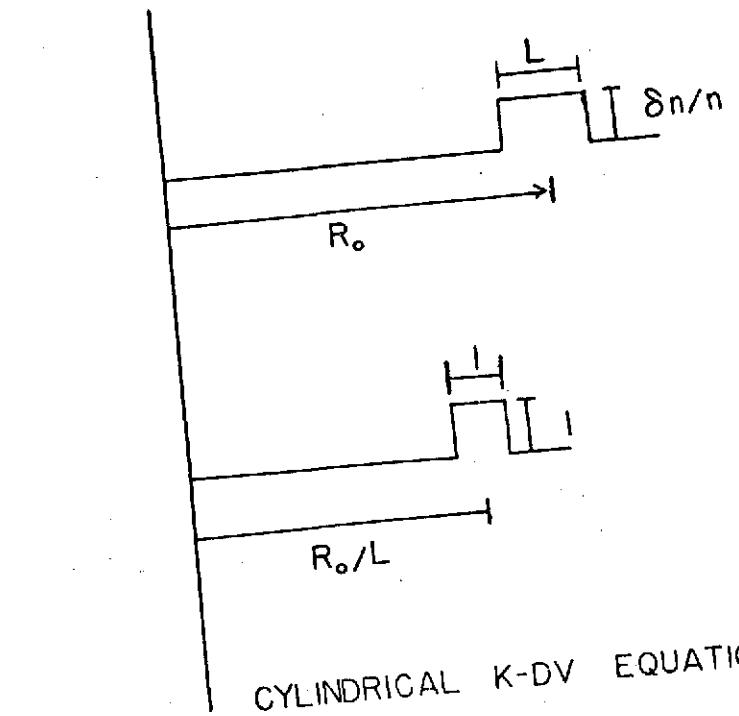

CYLINDRICAL K-DV EQUATION

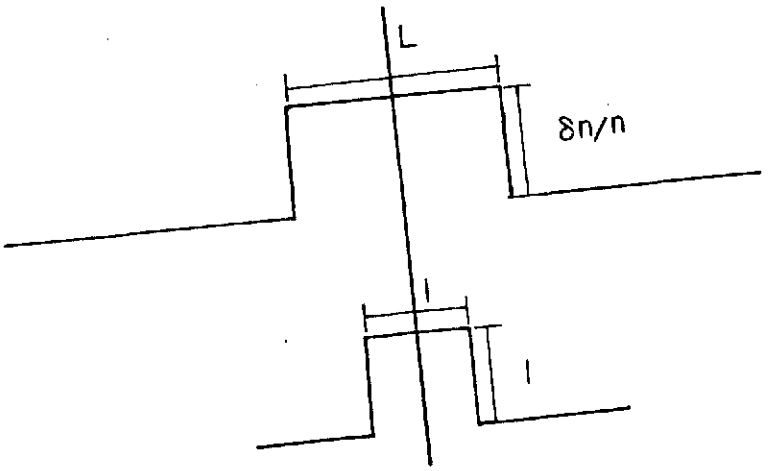

ORDINARY K-DV EQUATION

Figure 18

Figure 19 The dimensionless time is plotted versus a fit scaling parameter. The function form of the scaling parameter was chosen to yield a smooth curve.

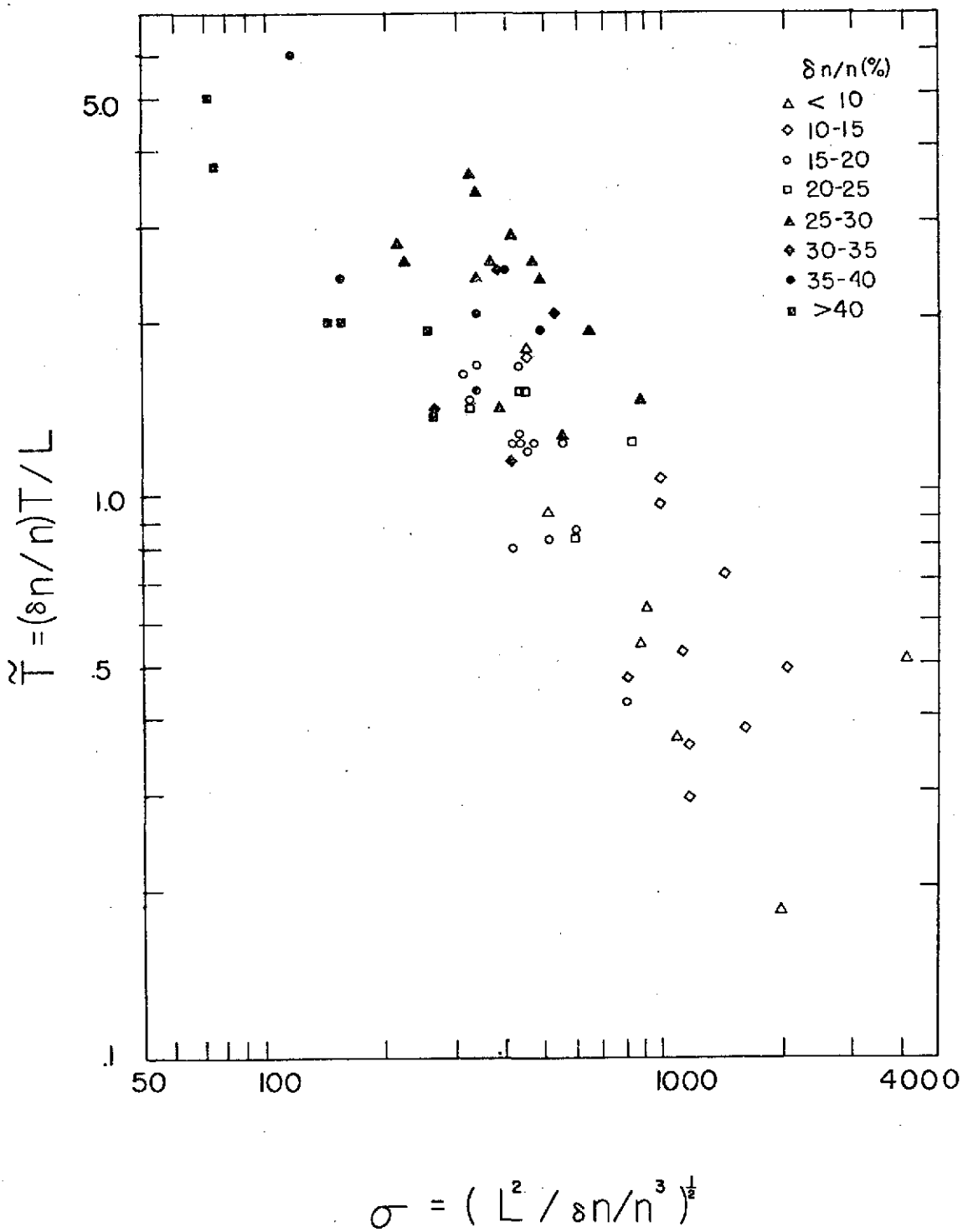
δn/n(%)
< 10
10-15
15-20
20-25
25-30
30-35
35-40
>40
5.0
1.0
.5
.1
50
100
1000
4000
$\tilde{T} = (\delta n/n)T/L$
$\sigma = (L^2/\delta n/n^3)^{\frac{1}{2}}$

Figure 19

Figure 20 Power spectrum of detected electron saturation current during instability, showing the first 3 harmonics as a function of beam velocity.

Figure 21 A comparison of the detected energy analyzer trace and a fit to the sum of two Gaussians. This is used to determine the beam energy very precisely, even in the region where beam and plasma are not well separated.

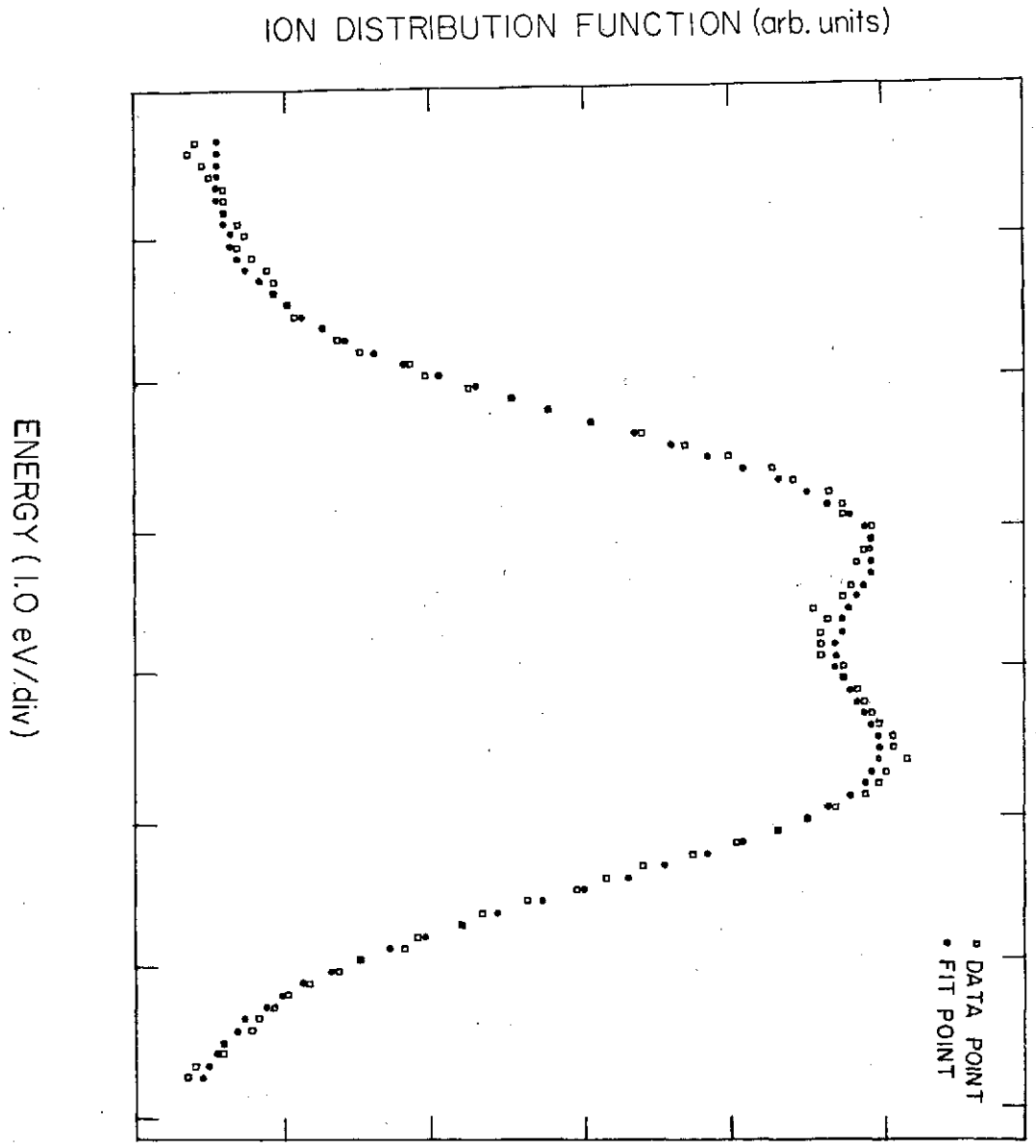
ION DISTRIBUTION FUNCTION (arb. units)
ENERGY (I.O eV/div)
□ DATA POINT
• FIT POINT

Figure 21

Figure 22 Power spectrum for the lowest 2 modes shown at varying radial positions.

A-G73-784

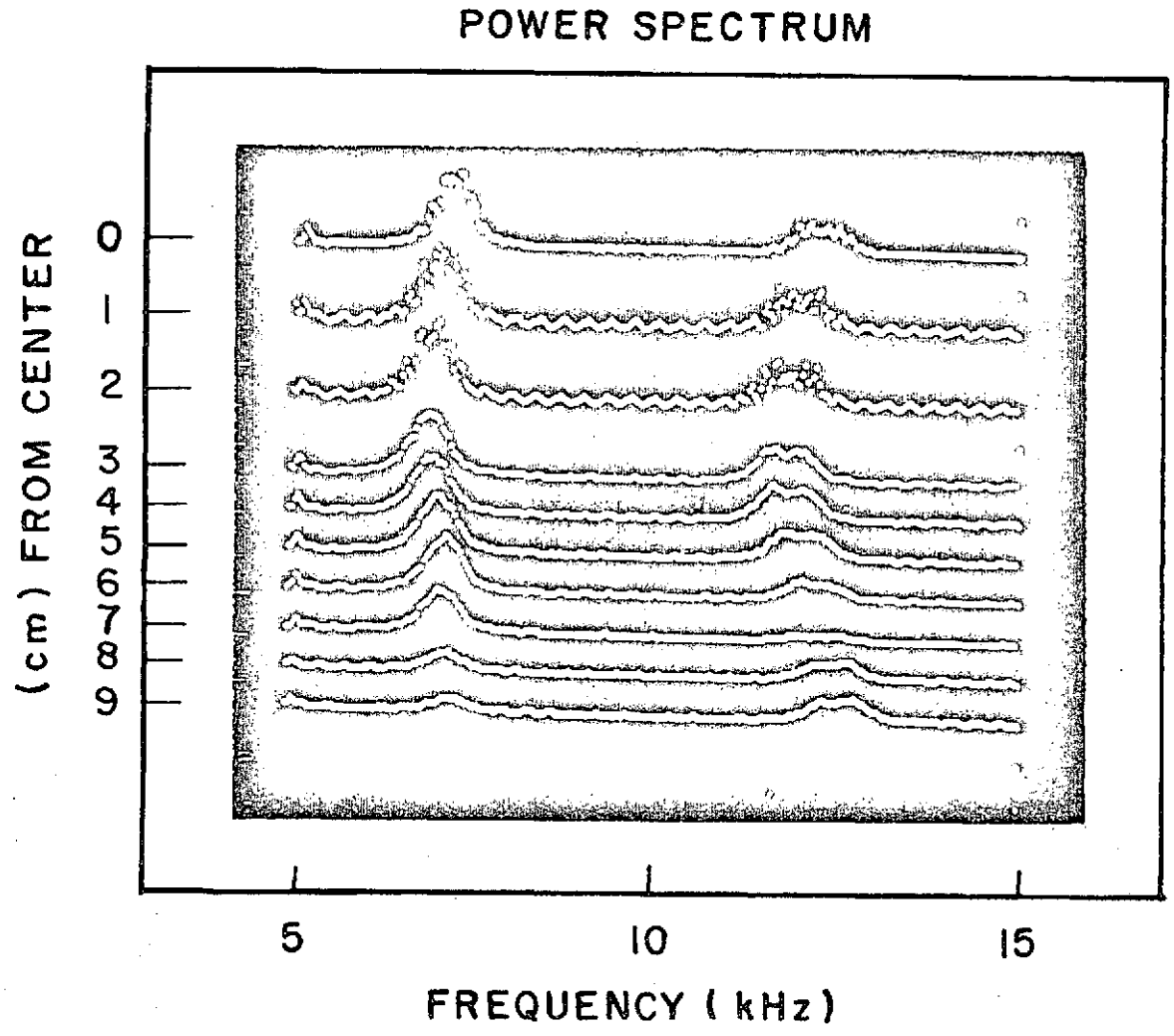

Figure 22

Figure 23 Frequency versus beam velocity for the lowest 3 harmonics. No unstable modes are observed for $v_B < 0.9 \times 10^5$ cm/sec or $v_B > 2.2 \times 10^5$ cm/sec.

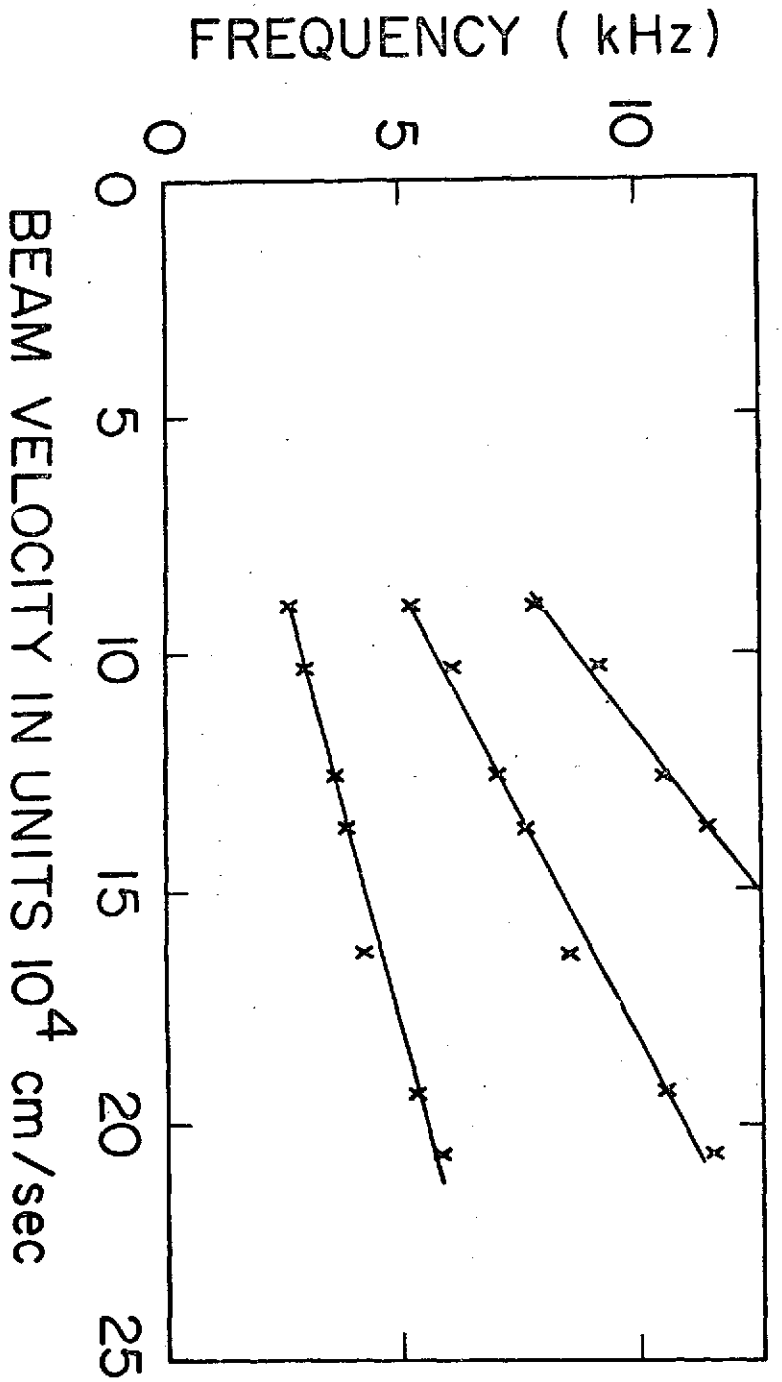
FREQUENCY (kHz)
0
5
10
0
5
10
15
20
25
BEAM VELOCITY IN UNITS 10^4 cm/sec

Figure 23

Figure 24(a) Ion distribution function versus voltage applied to the retarding grid for the radial energy analyzer. Traces are labeled by radial positions. The beam is clearly visible for all radial positions.

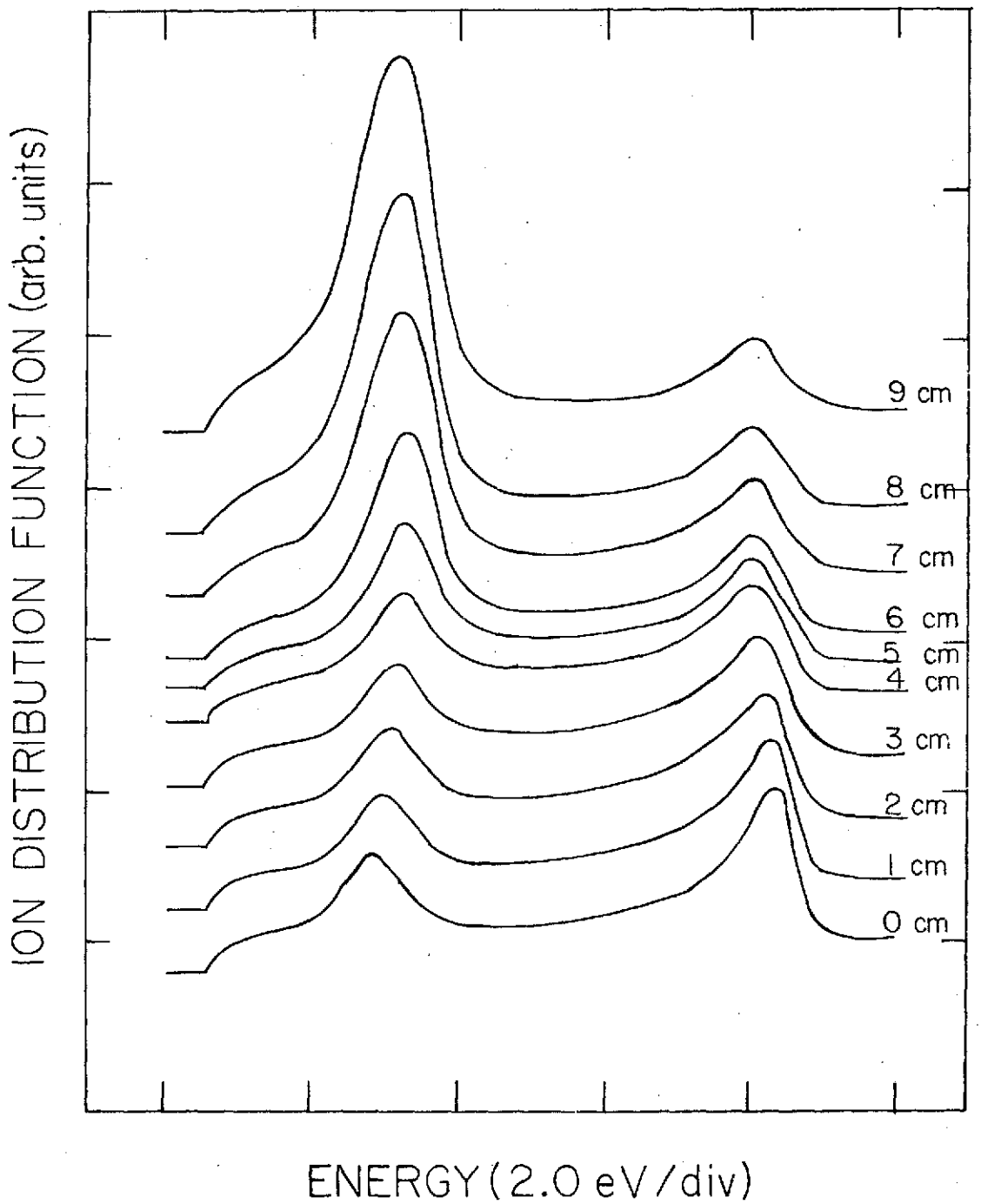
ION DISTRIBUTION FUNCTION (arb. units)
9 cm
8 cm
7 cm
6 cm
5 cm
4 cm
3 cm
2 cm
1 cm
0 cm
ENERGY (2.0 eV/div)

Figure 24(a)

Figure 24(b) Ion distribution function versus voltage applied to the retarding grid for the azimuthal energy analyzer. Traces are labeled by radial position and beam energy is identical with that of Fig. 24(a). The beam appears as well resolved at r = 4 cm.

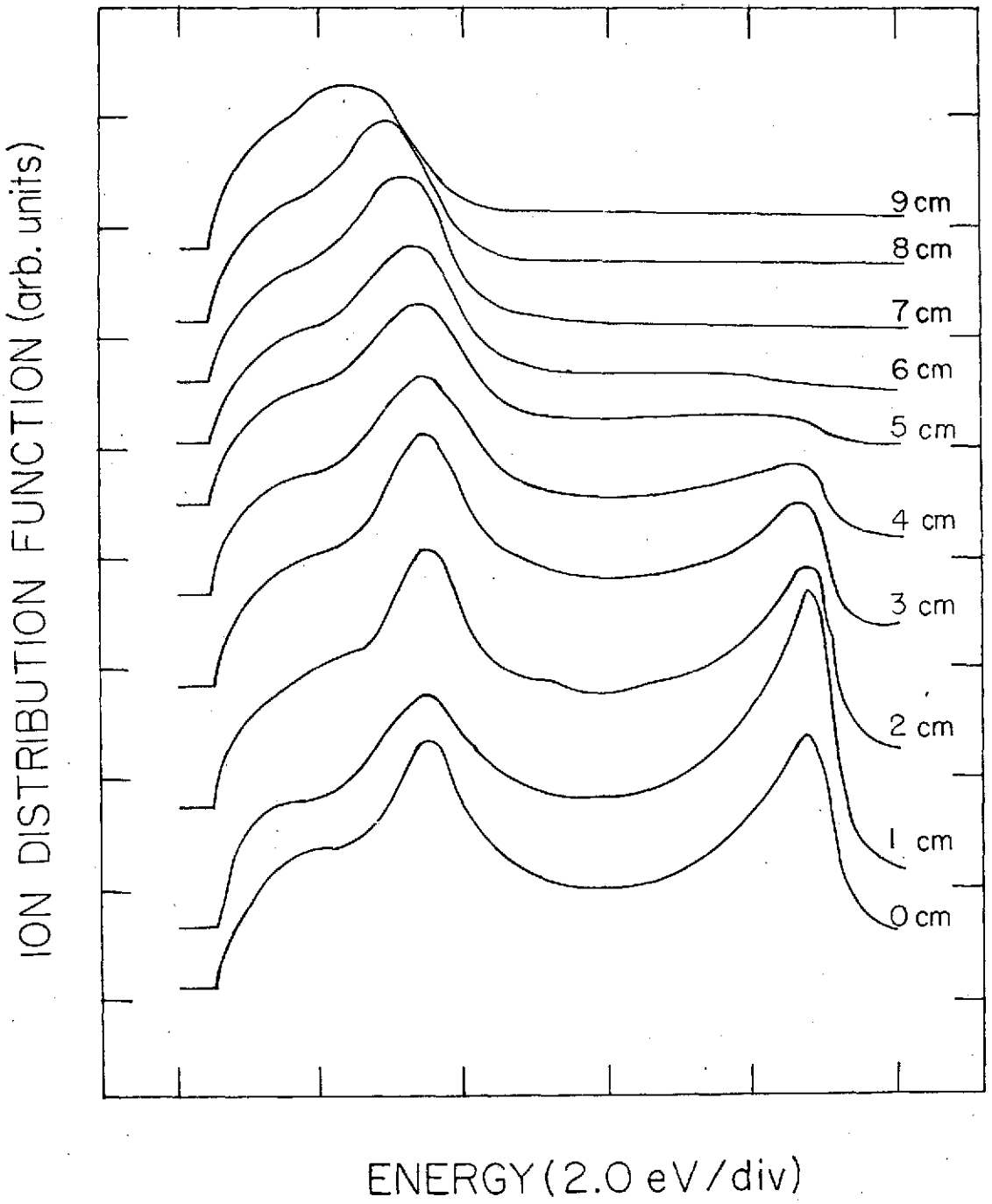
ION DISTRIBUTION FUNCTION (arb. units)
9 cm
8 cm
7 cm
6 cm
5 cm
4 cm
3 cm
2 cm
1 cm
0 cm
ENERGY (2.0 eV/div)

Figure 24(b)

Figure 25 Azimuthal energy analyzer traces for a 2.5 eV beam. The beam appears well resolved at r = 5 cm.

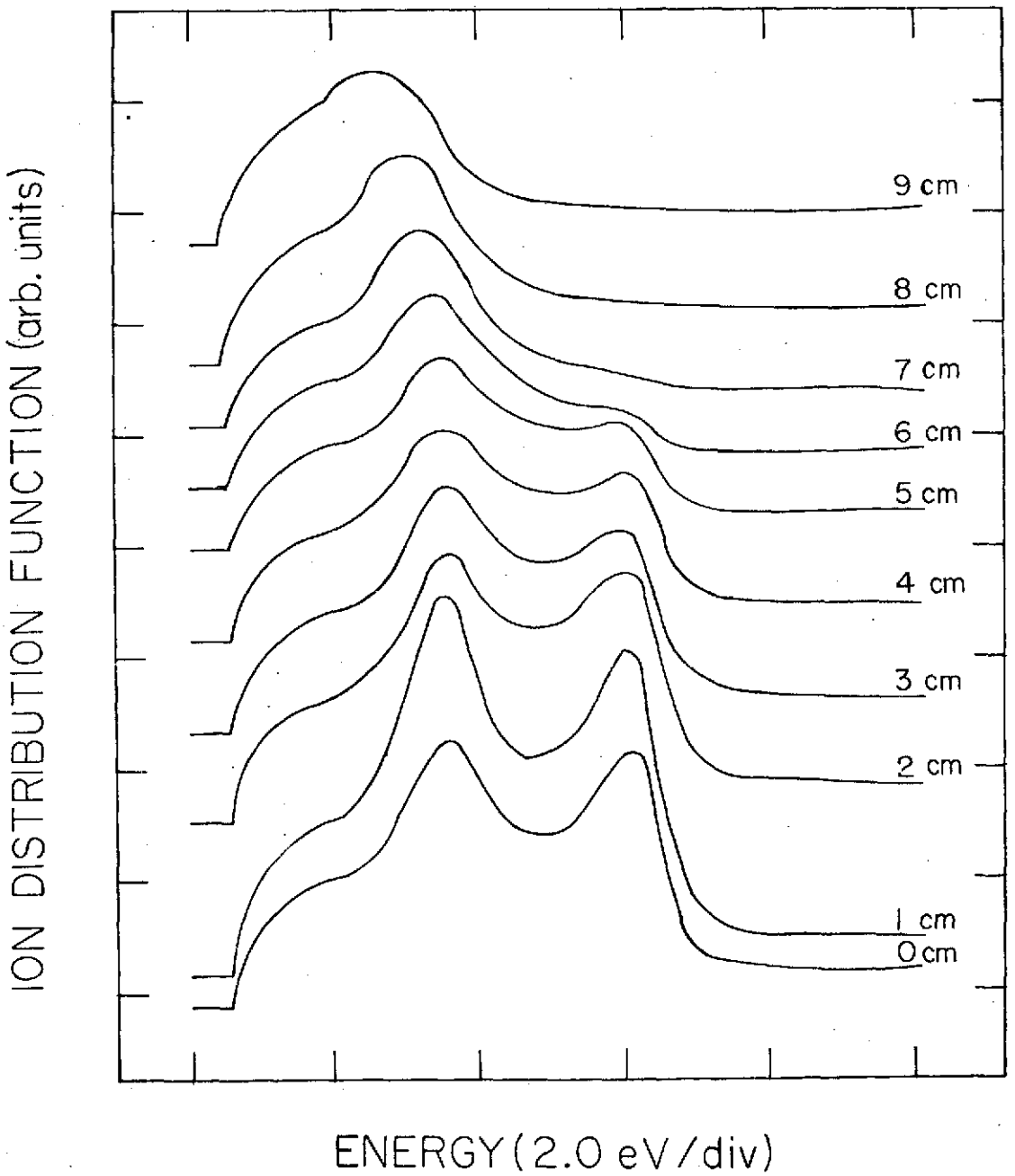
ION DISTRIBUTION FUNCTION (arb. units)
9 cm
8 cm
7 cm
6 cm
5 cm
4 cm
3 cm
2 cm
1 cm
0 cm
ENERGY (2.0 eV/div)

Figure 25

Figure 26 Graphical representation of how a radial beam with an angular spread of 2θ gives rise to a uniform density and ring distribution function in a region centered about the origin.

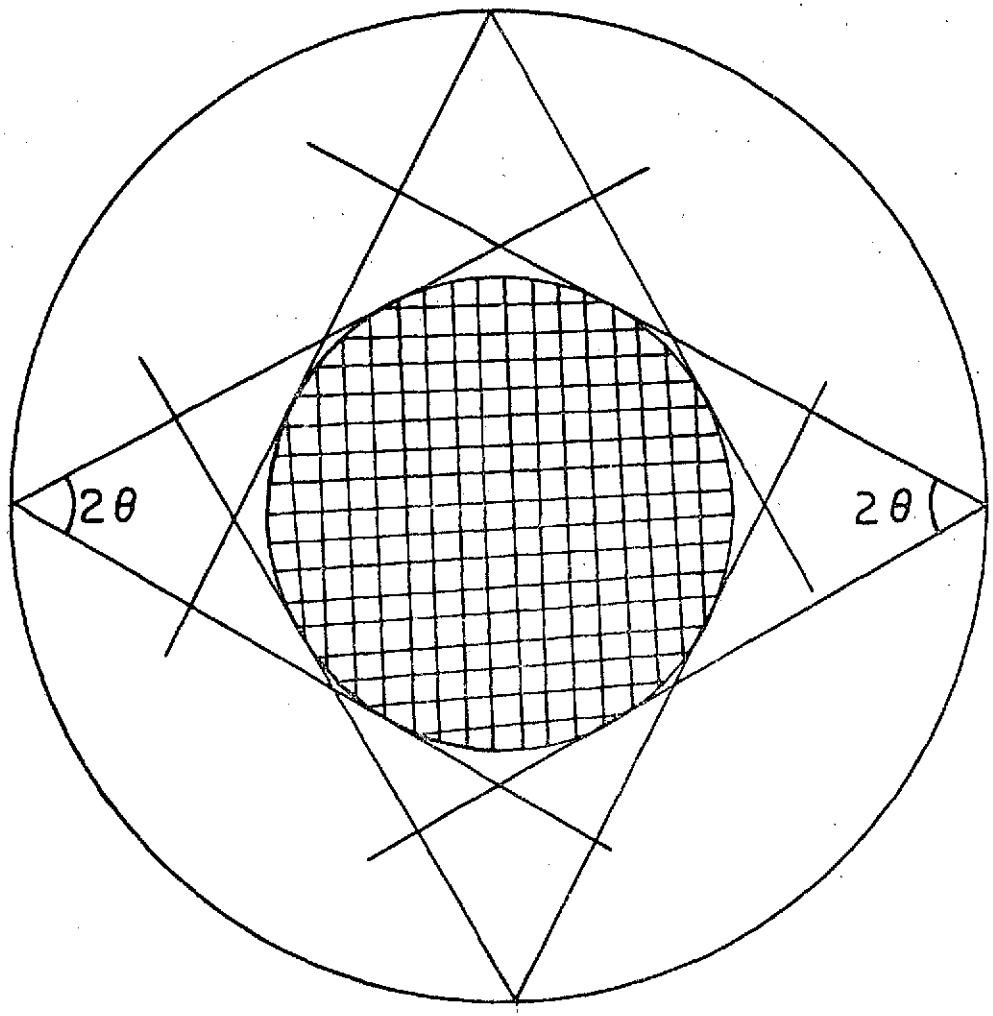

Figure 26

Figure 27 The projection of the ring distribution function onto one axis. An integrable sigularity occurs at $v = \pm v_B$.

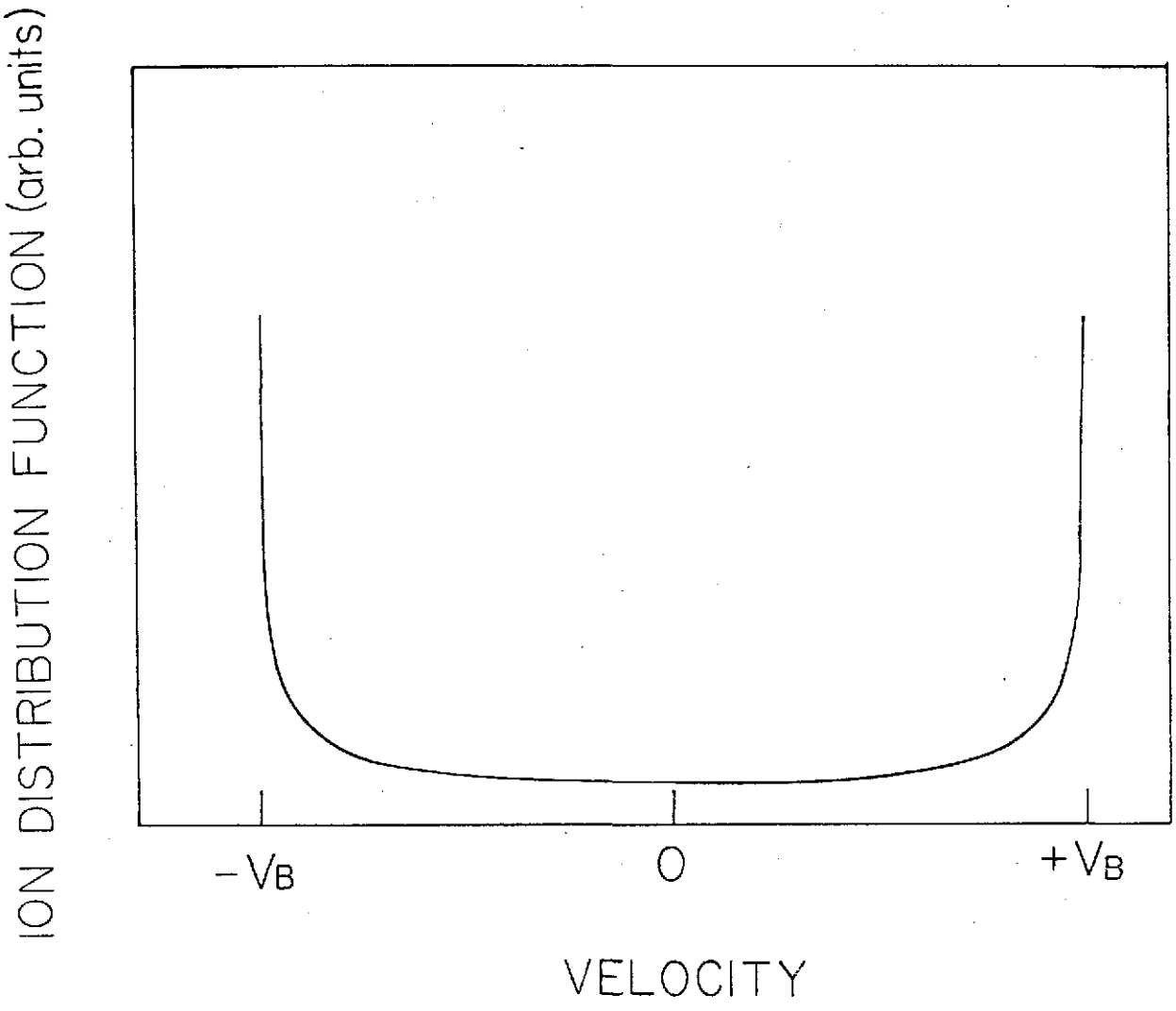

Figure 27

Figure 28 Frequency (ω) versus beam velocity and growth rate γ versus beam velocity for $\frac{n_B}{n_i} = .3$. In the region of maximum growth rate $\omega = \alpha v_B k$ where $\alpha = .645$. This plot arises from solution of the dispersion relation.

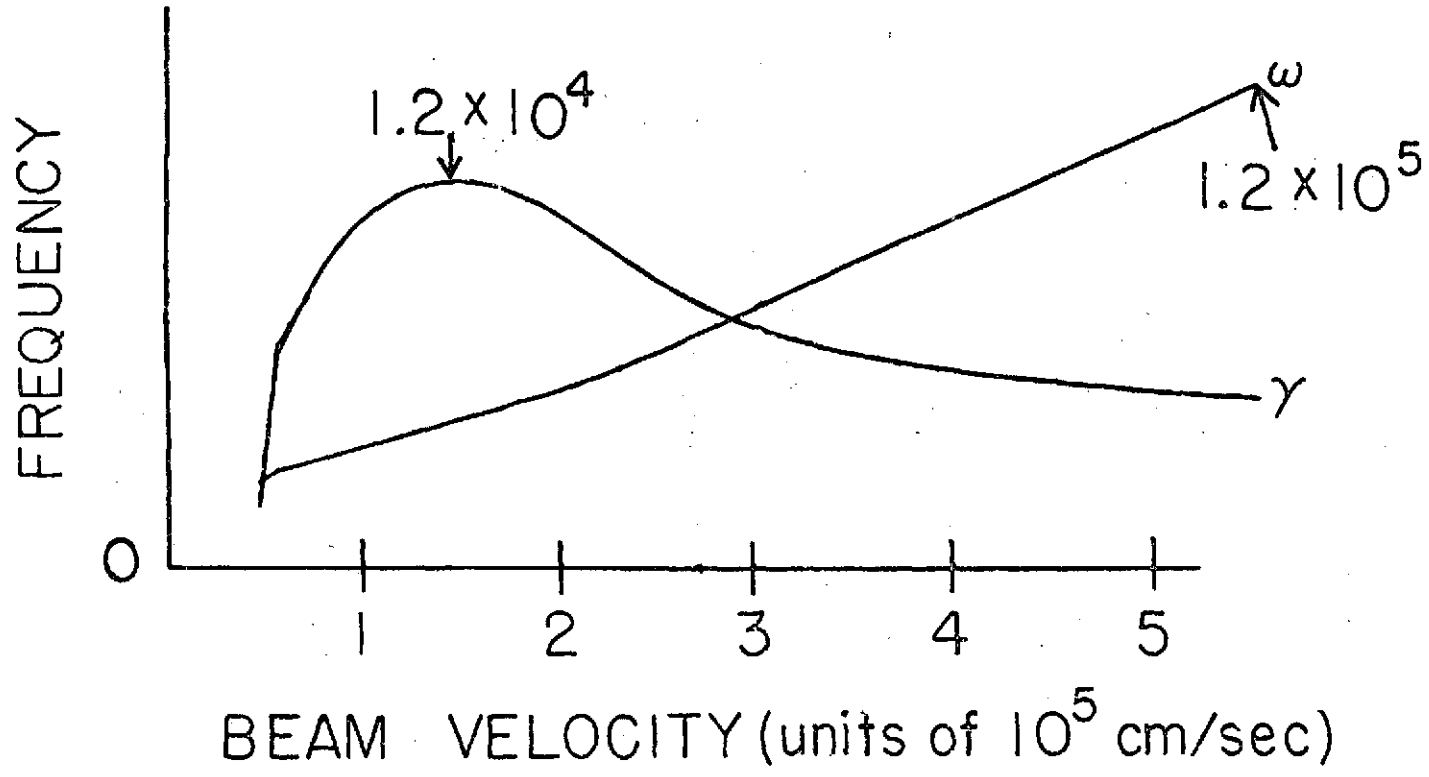
FREQUENCY
1.2 x 10^4
ω
1.2 x 10^5
γ
0
1
2
3
4
5
BEAM VELOCITY (units of 10^5 cm/sec)

Figure 28

Figure 29 Plot of α versus beam density where α is determined from $\omega = \alpha v_B k$ in the region of maximum growth rate. The values of α are determined from numerical solution of the dispersion relation for various values of beam density.

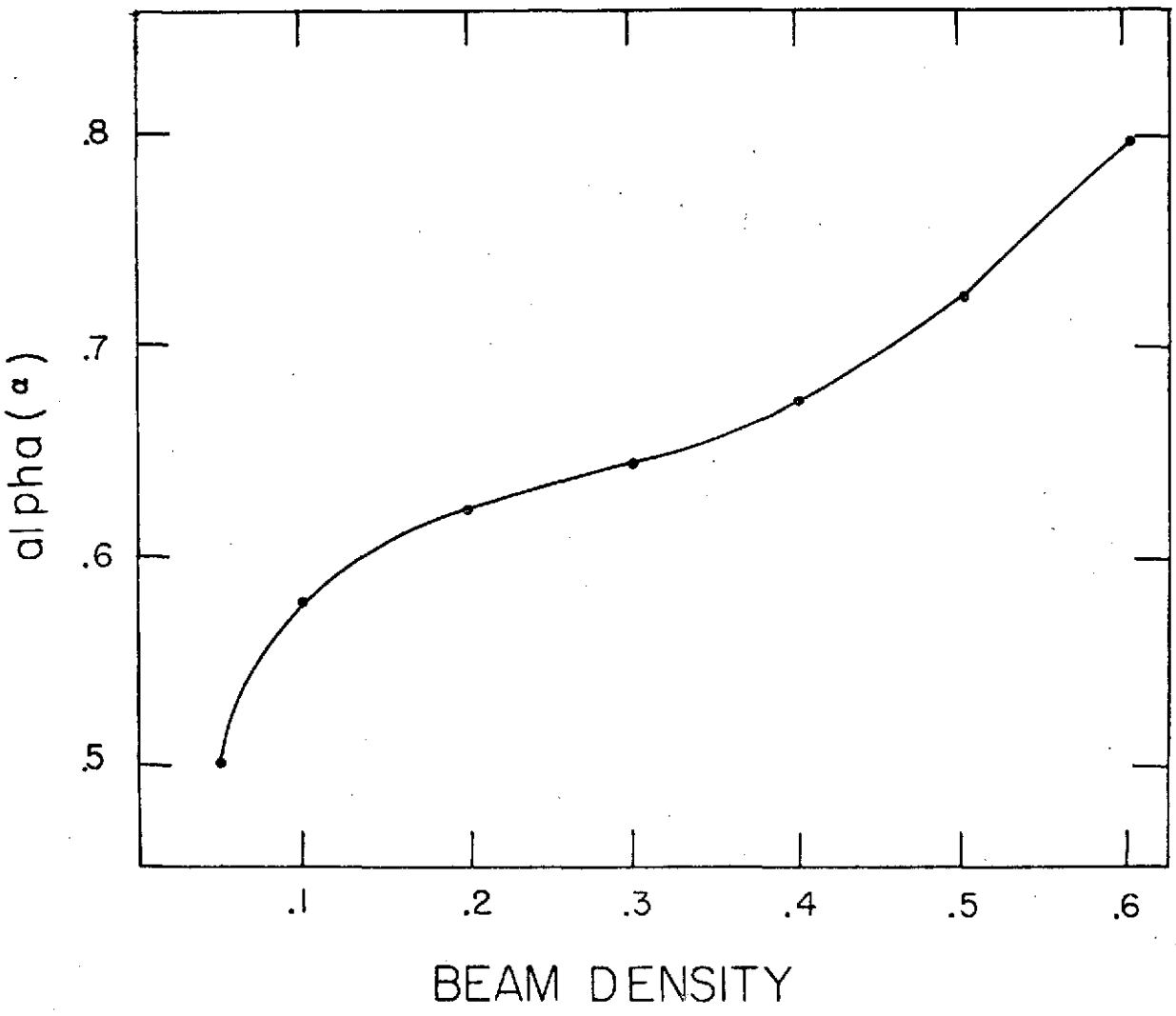

Figure 29

Figure 30 Memory allocation of data taking program.

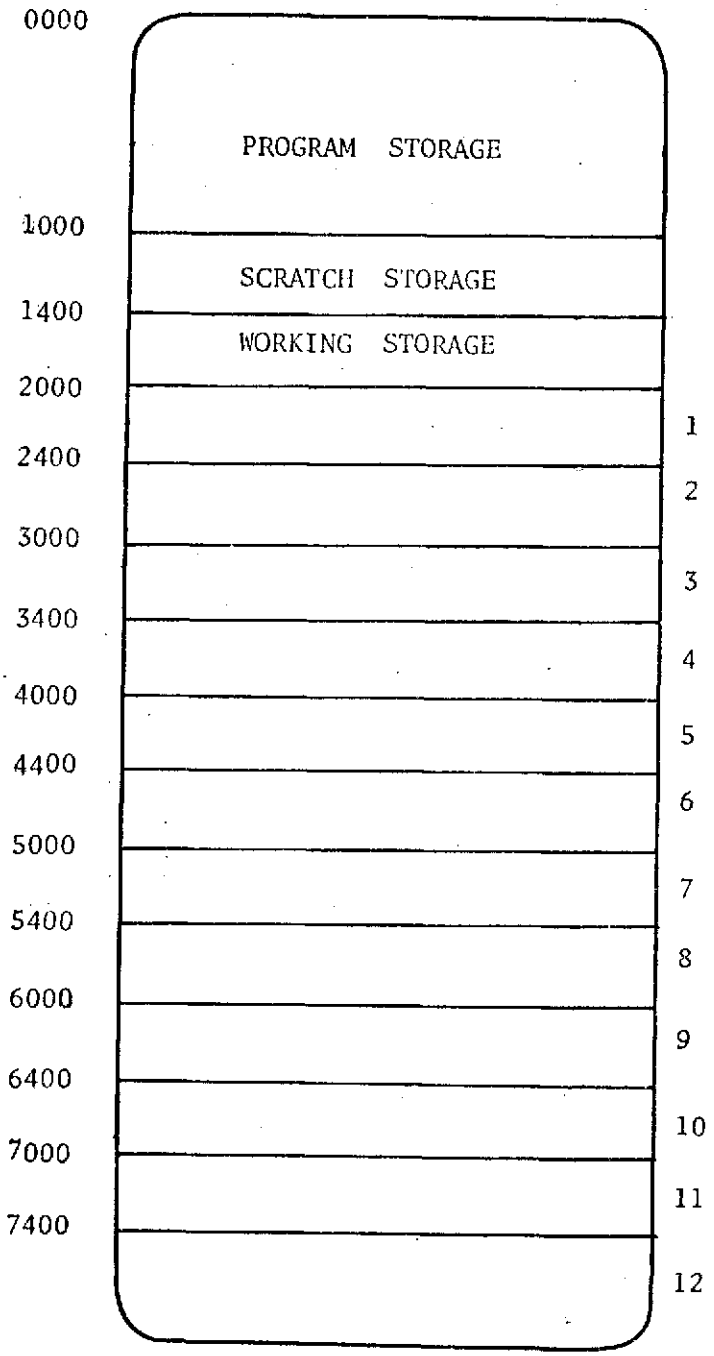
0000
PROGRAM STORAGE
1000
SCRATCH STORAGE
1400
WORKING STORAGE
2000
1
2400
2
3000
3
3400
4
4000
5
4400
6
5000
7
5400
8
6000
9
6400
10
7000
11
7400
12

Figure 30

Figure 31 Schematic of location of program control switches.

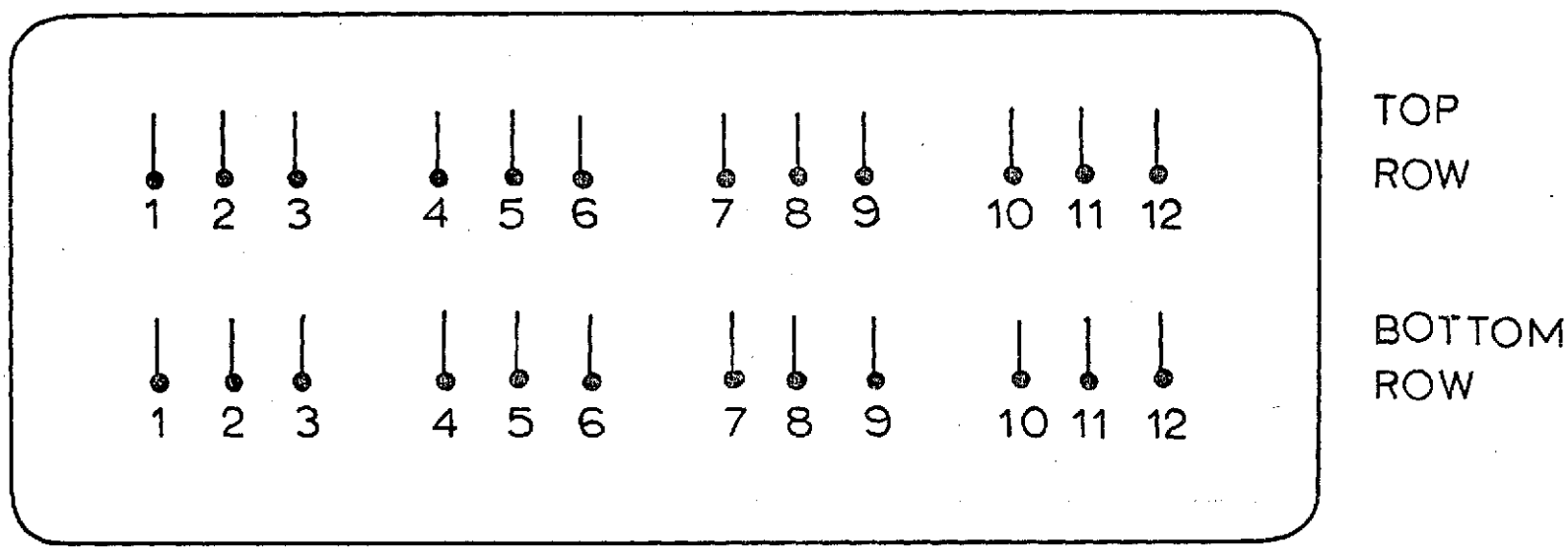

Figure 31

Figure 32 Chip placement diagram for fast buffer memory system.

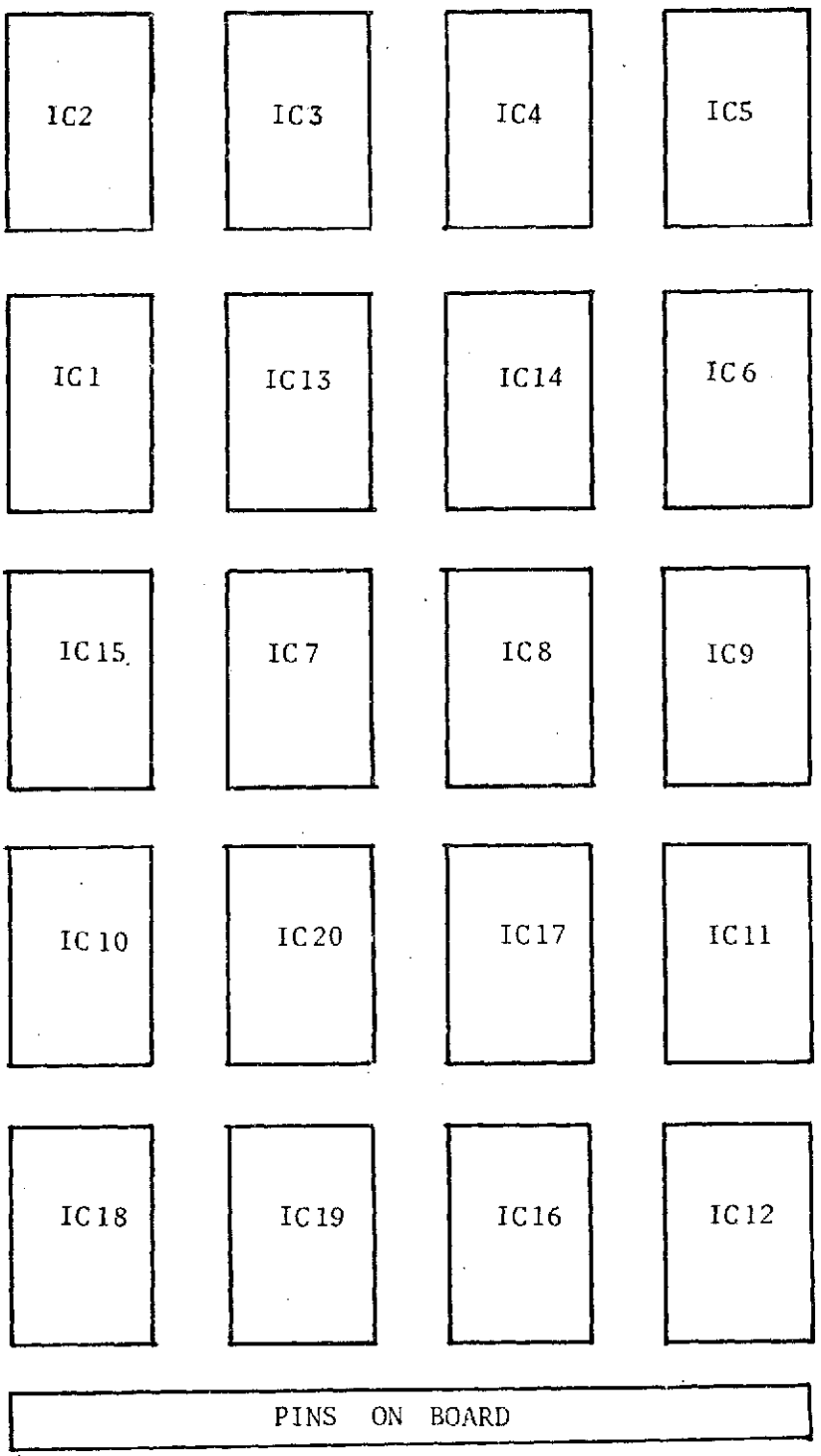

VIEW FROM BOTTOM

Figure 32

Figure 33 Circuit diagram for fast buffer memory system.

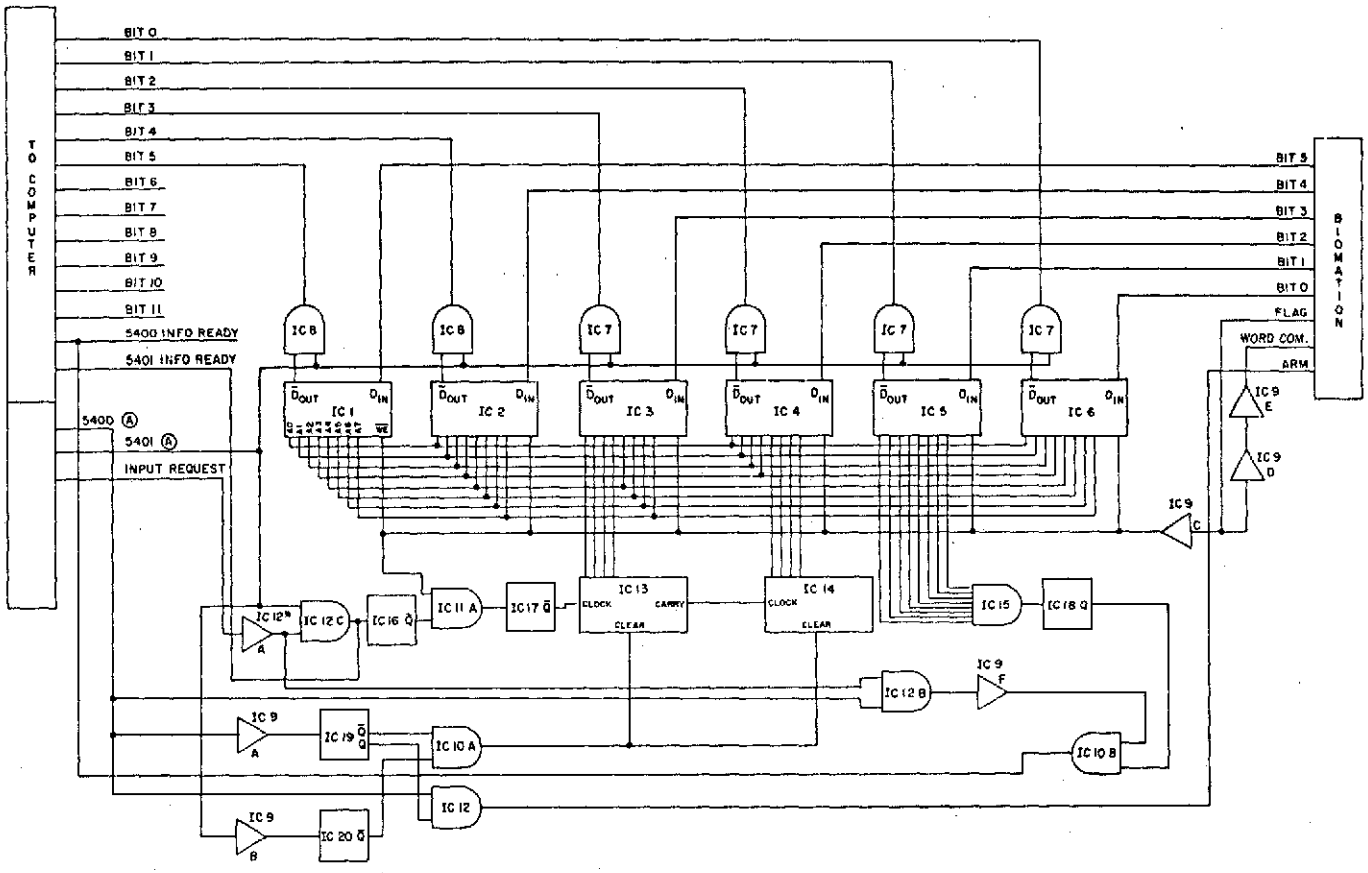

IC 1 - IC 6	745206	1 X 256 RAM
IC 7 - IC 8	7437	QUAD 2 INPUT NAND BUFFER
IC 9	7404	HEX INVERTER
IC 10 - IC 12	7400	QUAD 2 INPUT NAND
IC 13 - IC 14	54193	4 BIT SYNCHRONOUS BINARY COUNTER
IC 15	7430	8 INPUT NAND
IC 16 - IC 20	74121	MONOSTABLE MULTIVIBRATORS

* THIS TERMINAL OF IC 12 HAS INPUTS WIRED TOGETHER TO ACT AS INVERTER

Figure 33

APPENDIX

DIGITAL DATA TAKING SYSTEM

A. General Description

A versatile computer operated data taking system was constructed using equipment available at the University of Iowa. The system consists of a Control Data Corporation (CDC) 160 computer and associated peripheral equipment and an interface to the experimental apparatus. A Biomation 610B transient recorder, which serves as a fast analog to digital converter (ADC), digitizes the data and transfers it through the interface to the computer for processing. The Biomation 610B can digitize 256 data points with a resolution of 1 part in 64 and store them in its own internal memory for later readout by the computer. Data can be digitized at rates up to 100 nanoseconds per point.

The computer equipment presently on line with the system is:

1) CDC 160 Computer (4096 words of 12 bit memory)
2) CDC 163 Mag. Tape System (2 tape drives)
3) CDC 166 Line Printer (250 lines per minute)
4) CDC 161 Typewriter Station

In addition, the nuclear physics laboratory has a wide range of compatible CDC equipment, including a CDC 1604 computer system

with Fortran capability. Tapes can be generated by the CDC 160 to be processed on the 1604 system. The CDC 160 computer can be replaced with no changes to the interface by a CDC 160-A computer which has options for up to 32 k of memory.

Interaction of the experimenter with the computer and vice versa is accomplished by digital to analog converter (DAC) and by means of two rows of switches connected through the interface. Programs are generally written to scan the state of the switches. Changing the state of a switch will cause the program to branch to a predetermined routine. In this manner quite general purpose programs can be written. The DAC's are used to drive scope displays for the processed data to be displayed upon.

With the system described here, many useful functions are possible. Several of them are: For low amplitude signals or signals in which the noise is comparable to or greater than the signal, by digital addition of many passes the relative noise level is reduced and a clean signal is recovered. Even in the cases where the noise level is quite small, repeated addition of successive passes gives better resolution of the wave form. Precise measurements in time of flight experiments is possible with digital data. After repeated additions, the maximum (or minimum) is usually identifiable as one channel. For data for which an expected form is known a computer fit to the data is possible. An example of

this is seen in Fig. 21. Through the use of digital to analog converters, voltage levels from the computer can be fed to experimental apparatus, e.g. voltage controlled oscillators, remote programmable power supplies, and wave form generators, etc. With two Biomations correlation function measurements become possible.

With the existing equipment these and many more measurements are possible, limited only by the time resolution of the analog to digital converter (Biomation 610B).

The initial work on the interface from the Biomation to the CDC 160 computer was done by Dr. Stephen Wender [1973]. The wiring to convert the CDC logic levels (-18,0 volts) to the standard TTL logic levels (0,5 volts) and the logic circuitry necessary to decode the computer selection of devices was done first. Two rows of 12 switches each (used for program control) and circuitry for inputing from the Biomation were also completed by Dr. Wender. In his initial design there were 8 input ports that could be used. Two were used for program control switches and one was used for the initial Biomation 610B. A second Biomation has recently been added to the system. The four remaining parts can be used for any device with digital output (e.g., a digital voltmeter).

The author has extended the previous work to include provisions for 8 output ports. One digital to analog converter (DAC) can be connected to each port. This allowed for computer feedback of

of voltage signals to the experiment. The most standard use for the DAC is for scope displays of the digital data. They are also used to drive an x-y plotter for graphical copies of the processed data.

A fast buffer memory system was also designed and constructed to increase the transfer rate between the Biomation and the CDC 160 computer. The Biomation can output the digital data at a rate of either 2 microseconds per word or at a rate greater than 512 microseconds per word. The CDC 160 computer can input information at a rate of 4.8 microseconds per word. To obtain maximum transfer rate the Biomation dumps its memory into a buffer memory at 2 microseconds per word and when it is done the computer reads the buffer memory at 4.8 microseconds per word. This decreases the time for transfer of one data pass from a minimum of .13 seconds to .0015 seconds.

B. Program Description

1. Program

Data-Take, D-A, with Autoscale

2. Purpose

General purpose data taking program. Signal averaging by simple addition up to 64 times. Provisions for storing and viewing up to 12 data sets are included; data can then be dumped on magnetic

tape with an identifying header of up to 256 symbols. Program control is by means of the switch box.

3. Memory Usage

Locations 0000_8 to location 1000_8 are used for program storage. Locations 1000_8 to 1400_8 are used for scratch storage. Locations 1400_8 to 2000_8 are termed working storage. Locations 2000_8 to 7777_8 are divided into 12 storage areas of $400_8 = 256_{10}$ words (see Fig. 30).

4. Program Control Switches

Two rows of twelve switches are used for program control (Fig. 31). Each row represents one computer word and is grouped into four sets of three switches. Each set of switches represents one octal digit. Thus, any row of switches can be set to represent any number from 0000_8 to 7777_8. The three switches that represent an octal digit are a binary representation of that digit (e.g., on-off-on represents 5). A switch is given a 1 value by setting and leaving it toward the top.

Switches 1-6 on the bottom row are used for program control. The remaining 18 switches are used to feed information to the program as it executes. Switches 7-12 of the bottom row are used to tell how many times a signal should be averaged. They can be set from 1 to $77_8 = 64_{10}$.

Switch 1 on the bottom row is used to increase the versatility of the program. The role of switches 2-6 depends crucially on what position switch 1 is set to. For switch 1 = 0:

Switch 2: Causes retake of data when set to on position and then returned to off. Averaging will take place and a return to the display mode will be made. In the display mode the last data set taken is displayed. This is stored in the working storage area of Fig. 1.

Switch 3: When in display mode setting this switch on then off again causes the displayed data to be multiplied by a factor of 2.

Switch 4: When in display mode setting this switch on then off again causes the displayed data to be divided by a factor of 2.

Switch 5: This is used to store data into one of 12 availablve storage areas. The storage area is determined by the top row of switches. Switches 1-4 of the top row are used for this. The computer treats the remaining 8 switches as if they are zero, regardless of what they are set to be. The top row is then treated as the first word address to which the data is to be moved. This can take on any value from 2000_8 to 7400_8. Switches 1-3 are used to determine the first octal digit of the location, e.g., 2000, 4000, etc. The fourth switch is used to determine if the data is stored at $x000_8$ if the switch is zero, or at $x400_8$ if the switch is set. Caution. It is possible to destroy the program if a store is made to location 0000_8 or 0400_8!

Switch 6: This is used to view the 12 storage areas. Switches 1-4 of the top row select the appropriate storage area. They can be changed while switch 6 is set. The remaining 8 switches on the top row are used to zero one location for display purposes. This allows comparisons of different sets of data. These 8 switches can take on values from 0 to 377_8 corresponding to the 256 channels of the Biomation.

There are two 8 bit D-A converters available to the system. One of these is connected to the lower 8 bits of the 12 bit computer word while the other is connected to the upper 8 bits. Depending upon the number of times averaged, it may be more convenient to use one of these over the other. Provisions for this have been made in the program and a choice is implemented when switch 1 of the lower row is set to 1. Switch 1 set to 1:

Switch 2: Used to dump data onto magnetic tape. When switch 1 and switch 2 are thrown in that order, the input light on the typewriter station should come on. A header of up to 256 characters can then be typed in. The symbol "/" is not allowed as a valid symbol. At the end of the header a "/" is typed and this initiates the dumping of the header and the 12 storage areas in the computer onto magnetic tape. A return is then made to the display mode. Switches 1 and 2 should be returned to the zero position before typing in the header.*

---

*Tape to be written on must be loaded on a tape drive with unit number set to 1.

Switch 3: This selects the D-A converter that is connected to the upper 8 bits. The switch near the oscilloscope must also be in the correct position. To change from one to the other set the switch near the oscilloscope to the desired D-A converter and then flip switch 1 followed by either 3 or 4. Return both switches to off and the display should work.

Switch 4: This selects the D-A that is connected to the lower 8 bits. It is selected as described in the previous section.

5. To Run

Load program, clear and run from P = 0100. To initialize Biomation remove trigger signal, set to external trigger, clear computer and run from 0100. Light on left side of console should display static "IN". Remove from run, then clear and run from 0100. This assures that the first word input from the Biomation will be recognized by the computer as the first data point. It may be necessary to repeat this later if display indicates improper trigger. Connect trigger to Biomation and proceed to take data. If problems occur, run from 100 to take data or from 153 to go directly to display mode. (Note: If it is run from 0100, the first thing the program does is try to input data.)

6. Program

160 Data Plot

7. Purpose

To plot data that has been stored on magnetic tape.

8. Memory Usage

Locations 0000 to 1400 are used for program storage while locations 1400 to 7777 are used for storing data read in from magnetic tape.

9. Use

After loading program into computer run from location 0100, all switches on the switch box must be set to zero. The top row of switches is used to transfer information to the computer while the bottom row is used to control the program. The switches in the bottom row will be labeled from 1-12 staring from the left.

Switch 1: The left most switch is used to input data from the tape. Flipping the switch momentarily inputs one file from the tape and should type out the associated header. If switch is not returned to zero position, the tape will continue to read in.

Switch 2: Searches forward one file mark on the data tape.

Switch 3: Searches backward one file mark on the data tape.

Switch 4: Displays the data on the oscilloscope. It is used to display several sequential sets of data. The sets to be displayed are specified by the top row of switches. The left four bits specify the starting address. The program treats the left four bits as the uppermost bits of a word with all other bits set to 0.

The number of consecutive sets of data to be display is specified by the lowest four bits of the top row of switches.

Switch 5: Plots the data on the x-y plotter. The data to be plotted is specified in the same way as for displaying with switch 4. The upper four bits determine the first data set to be plotted while the lower four bits determine the number of plots to be put on the same page.

Switch 6: Plots a square to help in the alignment of the x-y plotter. The square plotted has the maximum range of x and y values possible and thus serves as a border for the paper.

Switch 7: Divides all of memory by 2. This is used in scaling to the correct height.

Switch 8: Multiplies all of memory by 2 in case the data is too small.

Switch 9: Displays locations 1400 to 2000 with the channel specified by the lower 8 bits of the top row set to zero. This can be used to follow the evolution of a waveform.

Switch 10: Used to exchange certain spectrum that are specified. The contents of locations 1400 to 2000 are exchanged with the data starting at the location specified by the left 4 bits of the top row.

Switch 11: Adds the amount specified by the lower 8 bits of the top row to the spectrum stored starting in location 1400. This is used to adjust the heights of different spectrum.

Switch 12: Displays both the contents of locations 1400 to 2000 but also the spectrum specified by the left 4 bits of the top row. This is used to compare the present data set to which one is adding set amount to the previously adjusted data set. With switch 12 set, any other switch can also be used. (Note: With switch 12 and switch 4 there is a slight problem with triggering of the oscilloscope. It is necessary to expand the trace with the time base slightly in order to get all of the traces displayed properly.)

C. High Speed Buffer Memory

In order to fully utilize the high speed characteristics of the Biomation 610B, it is necessary to build a high speed buffer memory. With this memory it is possible for the Biomation to read out its memory at 2 microseconds per word and then for the 160 computer to read the information at its highest possible operating speed.

This fast buffer memory is built on a card that fits into the original interface built by Dr. Stephen Wender. It makes use of the signals available from the interface. Figure 32 shows a diagram of the chip placement on the card. Figure 33 is a schematic circuit diagram with a list of the integrated circuits used.

The sequence of events that occur is described below. The computer executes a 7500 5400 instruction. When this happens, the 5400 A line from the computer makes a 0 to 1 transition. This

causes the output of IC9A to make a 1 to 0 transition. This fires the one-shot IC19. The Q output of this is used to arm the Biomation. The $\overline{Q}$ is fed into nand gate IC10A. The output of this is fed to the clear pin of the 4 bit counters IC13-14. After the Biomation is armed, it will be triggered and the flag will go high. The flag is inverted by IC9C and fed to the write enable memory chips where it causes the information putout by the Biomation to be written into the memory chips. This signal is also nanded through IC11A to the one-shot IC17. The firing of the one-shot advances the counters, so the next word from the Biomation will be read into the next memory location. The flag from the Biomation is also inverted twice by IC9D and E and fed to the word command on the Biomation. This causes the flag to be removed until the next word is available. After executing the 7500 5400 sequence a 7600 (input to A) is executed. The input request line from the computer makes a 1 to 0 transition. This, combined with the 5400 A line from the interface, is fed through IC12A and B and through IC9F to one input of IC10B. The other input of the nand gate IC10B comes from an 8 input nand gate where the inputs are hooked to the 8 address lines of the binary counters. It fires when the Biomation has read out all 256 channels. The output of IC10B is fed to the information ready and the computer resumes operation.

A similar procedure is followed to read the information from the memory chips to the computer. The computer executes a 7500 5401 which causes the 5401 A to make a 0 to 1 transition. This is fed through IC9B and fires the one-shot IC20. This is then fed to the clear inputs of the counters. The input request is inverted by IC12A nanded with 5401 A by IC12C. The output of this is then fed back to the information ready. It also fires the one-shot IC16. This is nanded through IC11A to fire the one-shot IC17 The purpose of IC16 is to put in a delay before IC17 fires to advance the counters. Input continues at the maximum rate possible for the computer.

Integrated Circuits Used

No.	Type	Description	Symbol
6	74s206	256x1 RAM Memory	IC1-6
2	54193	4 Bit Counters	IC13-14
2	7437	Buffered Nand	IC7-8
5	74121	Monostable Multi-vibrators	IC16-20
1	7430	8 Input Nand Gate	IC15
1	7404	Hex Inverter	IC9
3	7400	Quad 2 Input Nands	IC10-12

Note: The 54193 could be a 74193.

External resistors of 10 K are hooked between the outputs of the memory chips and +5 volts. These are described in the literature for the 74s206.

LIST OF REFERENCES

I. Alexeff, W. D. Jones and K. E. Lonngren, Phys. Rev. Letters 21, 878 (1968).

Yu. A. Berezin and V. I. Karpman, JETP 5, 1049 (1967).

N. Hershkowitz, T. Romesser and D. Montgomery, Phys. Rev. Letters 29, 1586 (1972).

N. Hershkowitz and T. Romesser, Phys. Rev. Letters 32, 581 (1974).

N. Hershkowitz, T. Romesser, G. Knorr and C. K. Goertz, Phys. Review Letters 33, 754 (1974)

M. Hudis, K. Chung and D. J. Rose, J. of Applied Phys. 39, 3297 (1968).

H. Ikezi, R. J. Taylor and D. Baker, Phys. Rev. Letters 25, 11 (1970).

H. Ikezi, Phys. Fluids 10, 1668 (1973).

K. R. MacKenzie, R. J. Taylor, D. Cohn, E. Ault and H. Ikezi, Applied Phys. Letters 18, 529 (1971).

S. Maxon and J. Viecelli, Phys. Rev. Letters 32, 4 (1974A).

S. Maxon and J. Viecelli, Phys. of Fluids 17, 1614 (1974).

R. Means, F. Coronitti, A. Wong and R. White, Phys. Fluids 16, 2304 (1973).

National Computational Laboratory, "Tables of Bessel Functions $Y_o(t), Y_1(t)$ for Complex Arguments," Columbia University Press, N. Y. (1950).

E. Ott and R. N. Sudan, Phys. Fluids 13, 1432 (1970).

E. Ott, Phys. Fluids 14, 748 (1971).

H. Schamel, J. of Plasma Physics 9, 377 (1973).

A. C. Scott, F. Y. F. Chu and D. W. McLaughlin, Proc. IEEE 61, 1443 (1973).

R. Stern and J. Decker, Phys. Rev. Letters 27, 1266 (1971).

F. D. Tappert, Phys. Fluids 15, 2446 (1972).

R. J. Taylor, H. Ikezi and K. R. MacKenzie, Proc. Inter. Conf. Phys. of Quiescent Plasmas, 8-13 Sept. (1969A) pp. 57-66

R. J. Taylor, D. Baker and H. Ikezi, Phys. Rev. Letters 24, 206 (1969B).

R. J. Taylor, K. R. MacKenzie and H. Ikezi, Rev. Sci. Instr. 43, 1675 (1972A).

R. J. Taylor and F. V. Coronitti, Phys. Rev. Letters 29, 34(1972B).

M. Q. Tran and P. J. Hirt, Plasma Physics 16, 617 (1974).

H. Washimi and T. Taniuti, Phys. Rev. Letters 15, 240 (1965).

S. Wender, Private Communication, (1973).

Observations of Ion-Acoustic Cylindrical Solitons

Noah Hershkowitz and Thomas Romesser*
Department of Physics and Astronomy, University of Iowa, Iowa City, Iowa 52242
(Received 24 January 1974)

Cylindrical solitons are seen to evolve from compressive cylindrical pulses in a collisionless plasma. The properties of these solitons are found to be consistent with the known properties of one- and three-dimensional solitons.

Soliton solutions are now well known for at least seven distinct *one*-dimensional wave systems.[1] In particular, the soliton solutions of the Korteweg–de Vries (KdV) equation have been extensively studied both theoretically and experimentally during the last decade and KdV is now known to approximately describe many systems which include nonlinear and dispersive effects.[1] Washimi and Taniuti[2] have shown that slightly nonlinear one-dimensional ion acoustic waves in collisionless plasmas with cold ions are described by KdV. In a recent Letter, Maxon and Viecelli,[3] following the procedure of Ref. 2, have derived a modified KdV equation for spherically symmetric ingoing waves. In this Letter we present experimental observations of cylindrical solitons in a collisionless plasma.

One-dimensional solitons have several distinguishing characteristics.[4-11] Among them are the following: (1) Arbitrary positive (compressive) density perturbations evolve after sufficient time into a superposition of spatially separated solitons (solitary pulses). (2) The number and amplitude of the solitons is determined by the solution of an appropriate time-independent Schrödinger equation with a potential well that is proportional to the initial spatial density perturbation. One soliton is formed for each bound state with soliton amplitude proportional to the energy eigenvalues. (3) The soliton velocity is given by $1+\frac{1}{3}(\delta n/n)]c_s$, where $\delta n/n$ is the maximum density perturbation of each soliton and c_s is the ion acoustic velocity. (4) The spatial widths are proportional to $(\delta n/n)^{-1/2}$, which implies that the product of the square root of the maximum soliton amplitude multiplied by the width is a constant. (5) Solitons retain their identity upon collision with other solitons.

All of these properties have recently been verified experimentally with collisionless plasmas. Linear double-plasma (DP) devices were used by Ikezi, Taylor, and Baker[12] to verify all but the second property, and by Hershkowitz, Romesser, and Montgomery[13] to verify the connection with the underlying Schrödinger equation [property (2)]. Cohn and MacKenzie[14] investigated solitons resulting from very large density perturbations produced by photoionization. A summary of much of the experimental evidence has been given by Ikezi.[15]

In the first work, which considers solitons of dimensionality greater than one, Maxon and Viecelli[3] have numerically determined that spherical solitons have the following four properties. First, an ingoing soliton increases in amplitude while decreasing in width, thus retaining its identity as a *single* soliton. Second, the product of the square root of the maximum soliton amplitude multiplied by the width is a constant. Third, a small residue develops and moves inward behind the soliton, taking up a measurable percentage of the total momentum; and fourth, the soliton velocity is somewhat greater than the velocity of a corresponding one-dimensional soliton.

In this Letter we present data showing that cylindrical solitonlike objects exist and that their properties are consistent with those of one- and three-dimensional solitons. These results are to our knowledge the first experimental evidence for solitons of dimensionality greater than 1.

Experiments were carried out using a cylindrical DP device which had previously been used to study the ion-ion beam instability of cylindrical beams and background plasma.[16] Two concentric

cylindrical plasmas (length 30 cm) are separated by two closely spaced, fine-mesh, concentric cylindrical screens with inner screen diameter equal to 20 cm. The outer screen is negatively biased to prevent the flow of electrons between the plasmas, and the inner screen is grounded. The ion density was approximately 10^9 cm^{-3} and the ion and electron temperatures were approximately 0.2 and 3 eV, respectively. Positive half-sine-wave pulses are applied to the outer plasma to launch cylindrical density perturbations in the inner plasma.

Signals are detected by a positively biased Langmuir probe which has variable radial position. No azimuthal dependence was observed. Figure 1(a) shows the perturbed electron number density as a function of time at several radial positions for both large and small initial density perturbations. For the small-amplitude pulse at $r=9$ cm we can identify an ingoing pulse, which is quite similar to the applied pulse, followed at a later time by a similar outgoing pulse that has propagated from the opposite side and through the center. As the probe is moved closer to the center the ingoing and outgoing pulses approach each other, merging at the center. For the large-amplitude compressive pulse at $r=9$ cm the ingoing pulse is seen to be similar to the applied pulse, but three solitons can be identified in the outgoing pulse. The traces at other radial positions indicate how the initial density perturbation evolves into the solitons. The increased velocity of the first two solitons compared to the ion acoustic velocity is evident. Once formed, the largest soliton is seen to be much narrower than the applied pulse. We find that the average velocity of the largest ingoing soliton is approximately $1.17c_s$. The application of a negative (rarefactive) density perturbation is not found to evolve into solitons.

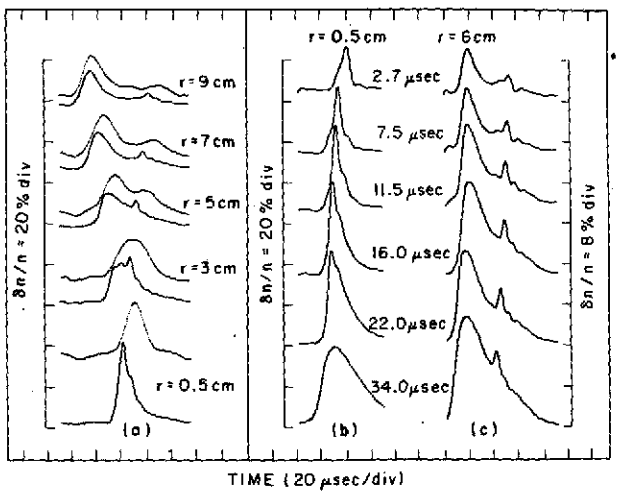

FIG. 1. (a) Perturbed electron number density as a function of time at several radial positions. Upper traces, linear ($\delta n/n < 1\%$) ion acoustic pulses (with amplitude adjusted for comparison). Lower traces, nonlinear pulses propagating, steepening, and breaking into solitons. (The received signals are digitized and stored on magnetic tape for later analysis. This is the cause of the observed steplike structure.) (b) Perturbed electron number density detected at $r=0.5$ cm labeled by the applied pulse widths. (c) Received signals at $r=6$ cm labeled by applied pulse width.

As in the one-dimensional DP device, the maximum applied voltage is limited by the electron temperature.[13] For applied voltages larger than the electron temperature (here ≈ 3 eV), particle bursts (pseudowaves) are detected. Data were taken with the largest initial density perturbathat could be obtained without launching pseudowaves. The width of the applied pulse was then varied to determine how the soliton number depended on the initial density perturbation (see Fig. 1). This procedure was identical to that followed in our earlier measurements (Ref. 13). Figure 1(b) shows how the signal received, $r=0.5$ cm, depends on applied pulse width. *Widening* the applied pulse results in increased amplitude, decreased width, and increased velocity in the received signal. In the top trace we see one well-defined soliton. In the second trace the first soliton has grown and narrowed and a second soliton is apparent. In the third trace the first two solitons have grown, narrowed, and speeded up. A third soliton is barely apparent. We find that the square root of the maximum amplitude multiplied by the width is constant to within 10% for the first four traces. In the fourth trace the third soliton is seen to grow as well. For further increases in width the solitons no longer have sufficient time to separate from the initial perturbation. Figure 1(c) shows the signals corresponding to the same six applied pulse widths as detected at $r=6$ cm.

For small applied pulse width it is possible to launch single solitons whose amplitude depends on the applied pulse width. The amplitude of an incoming soliton was found to be approximately constant over much of its trajectory as a result of a competition between damping and geometric growth (see Fig. 1). This simplified the determination of the amplitude dependence of the velocity. Figure 2 shows the soliton velocities, determined from individual soliton trajectories,

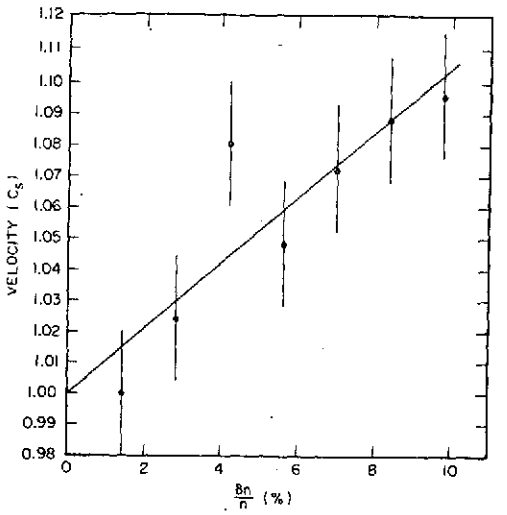

FIG. 2. Velocity of single solitons as a function of the maximum soliton amplitude.

versus soliton amplitude. The best least-squares fit to these data gives $v = [1 + a(\delta n/n)]c_s$, where $a = 1.05 \pm 0.20$. This is faster than a corresponding one-dimensional soliton.

This experiment differs from an idealized one in at least two respects. First, as in one-dimensional experiments, damping is present. After accounting for a geometric increase which goes like $(r_0/r)^{1/2}$, the ion acoustic pulse is seen to damp by about a factor of 3 in propagating 9 cm, and the soliton damps by a factor of 1.5. In the absence of damping, the geometrical growth factor (r_0/r) should only be expected to hold for linear ion acoustic pulses. Second, the density perturbation is not found to diverge at the center. We attribute this result in part to broadening of the received pulse as a result of variations in the radius of the cylindrical screens of the order of 0.3 cm and to finite size of the probe and of an insulating glass cylinder (0.5 cm) which covers all but the last centimeter of the probe.

We summarize the measured properties of *two*-dimensional solitons. Compressive density perturbations evolve into solitons. The number of the solitons is determined by the width and amplitude of the applied pulse. Rarefactive perturbations do not evolve into solitons. The solitons retain their identity after converging (colliding) at the center. All of these are well-known properties of *one*-dimensional solitons. In addition we find that the soliton width multiplied by the square root of the maximum soliton amplitude is approximately constant even though the amplitude, width, and velocity are functions of time. The velocity is somewhat greater than the velocity of a corresponding one-dimensional soliton. Both of these properties of three-dimensional solitons and the first holds for one-dimensional solitons as well.

Maxon has recently derived a modified KdV equation for cylindrical solitons.[17] Detailed comparison with numerical solutions of this equation will be presented in a later publication. Attempts will be made to compare the amplitude, width, and propagation speed as a function of time with numerical solutions of a modified KdV equation for cylindrical solitons which includes damping when such results become available.

We thank S. Maxon for helpful discussions and Alfred Scheller for construction of much of the apparatus.

*Work supported in part by the National Aeronautics and Space Administration under Grant No. NGL-16-001-043.

[1]A. C. Scott, F. Y. F. Chu, and D. W. McLaughlin, Proc. IEEE 61, 1443 (1973).

[2]H. Washimi and T. Taniuti, Phys. Rev. Lett. 17, 996 (1966).

[3]S. Maxon and J. Viecelli, Phys. Rev. Lett. 32, 4 (1974).

[4]N. J. Zabusky and M. D. Kruskal, Phys. Rev. Lett. 15, 240 (1965).

[5]N. J. Zabusky, Phys. Rev. 168, 124 (1968).

[6]C. S. Gardner, J. M. Greene, M. D. Kruskal, and R. M. Miura, Phys. Rev. Lett. 19, 1095 (1967).

[7]V. I. Karpman, Phys. Lett. 25A, 708 (1967).

[8]Yu. A. Beresin and V. I. Karpman, Zh. Eksp. Teor. Fiz. 46, 1880 (1964), and 51, 1557 (1966) [Sov. Phys. JETP 19, 1265 (1964), and 24, 1049 (1967)].

[9]R. Miura, J. Math. Phys. (N.Y.) 9, 1202 (1968); R. Miura, C. S. Gardner, and M. D. Kruskal, *ibid.* 1204 (1968); C. H. Su and C. S. Gardner, *ibid.* 10, 536 (1969); C. S. Gardner, *ibid.* 12, 1548 (1971); M. D. Kruskal, R. M. Miura, C. S. Gardner, and N. J. Zabusky, *ibid.* 11, 952 (1970).

[10]F. D. Tappert and N. J. Zabusky, Phys. Rev. Lett. 27, 1774 (1971).

[11]M. Wadati and M. Toda, J. Phys. Soc. Jap. 32, 1403 (1972).

[12]H. Ikezi, R. J. Taylor, and D. R. Baker, Phys. Rev. Lett. 25, 11 (1970).

[13]N. Hershkowitz, T. Romesser, and D. Montgomery, Phys. Rev. Lett. 29, 1586 (1972).

[14]D. B. Cohn and K. R. MacKenzie, Phys. Rev. Lett. 30, 258 (1973).

[15]H. Ikezi, Phys. Fluids 16, 1668 (1973).

[16]N. Hershkowitz and T. Romesser, Bull. Amer. Phys. Soc. 18, 1260 (1973).

[17]S. Maxon, private communication.

Ion-Ion Beam Instability in a Cylindrical Geometry

Noah Hershkowitz,* Thomas Romesser,† Georg Knorr,‡ and Christoph K. Goertz§
Department of Physics and Astronomy, The University of Iowa, Iowa City, Iowa 52242
(Received 21 January 1974)

The ion-ion instability is studied in a cylindrical double-plasma device. Low frequency cylindrical standing waves are found which are one-dimensional in character with frequency proportional to beam velocity. An approximate dispersion relation for the cylindrical standing waves is derived.

Double-plasma (DP) devices have recently been used to study the incoherent ion-ion two-beam instability produced by one-dimensional beams in unmagnetized plasmas.[1-5] This turbulence is found to be *three*-dimensional in character in agreement with the linear theory of the ion-ion instability[6-9] which predicts that the instability depends on $\vec{k}\cdot\vec{v}_b$, where $\vec{k}$ is the *plane*-wave propagation vector and $\vec{v}_b$ is the beam velocity. Although there is an upper limit on v_b beyond which the *one*-dimensional ion-ion instability will not grow, there always will be oblique directions for which the projection of $\vec{v}_b$ on $\hat{k}$ will give growing modes in *three* dimensions. Means *et al.*[10] have recently argued that the observation of turbulence in experiments with *one*-dimensional electrostatic ion acoustic shocks depends fundamentally on this *three*-dimensional property of the instability.

In this Letter we report the production of a coherent ion-ion instability which is essentially one-dimensional in character. This has been accomplished by generating cylindrical *standing* waves which are resonant with ingoing and outgoing beams in a cylindrical DP device at the University of Iowa. This device differs from convential DP devices[1-5] in that the cylindrical boundary of the plasma plays a dominant role. A grounded cylindrical screen through which the beam in injected, serves as a well-defined boundary condition (vanishing potential) for the standing waves. In conventional devices[1-5] the dimensions were such that wave and particle phenomena were *not* significantly affected by the presence of boundaries. The dimensions of those devices were *large* compared to the ion charge-exchange length, the e folding distance for ion-acoustic waves, and all wavelengths of interest. In the cylindrical DP device described here the diameter of the plasma is comparable to these lengths.

A description of these standing waves is derived from the Vlasov equation in a cylindrical geometry. The dependence of the frequencies ω of the instabilities on the beam velocity is shown to be remarkably similar, but not identical, to the results for a strictly one-dimensional ion-ion instability.

The cylindrical DP device, which has recently been used to study cylindrical solitons,[11] is shown in Fig. 1. Two *concentric* argon plasmas are separated by an outer negatively biased screen and an inner screen *held at ground potential.* Plasma within the inner cylinder is produced in an adjacent connected chamber. Typical operating parameters were electron temperature $T_e \approx 1$ eV, ion temperature $T_i \approx 0.1$ to 0.2 eV, average plasma density $n_i \sim 10^8$ to 10^9 cm^{-3}, and pressure $\approx 2\times10^{-4}$ Torr. A steady-state radially ingoing cylindrical beam is formed by raising the plasma potential in the outer cylinder. Beam density ratios $\eta \equiv n_b/n_i$ are controlled by varying the concentric discharges. The ion charge-exchange length was greater than the inner-cylinder radius.

Energy distribution functions in the inner plasma (region A in Fig. 1) are measured with two energy analyzers with depth-to-area ratios great-

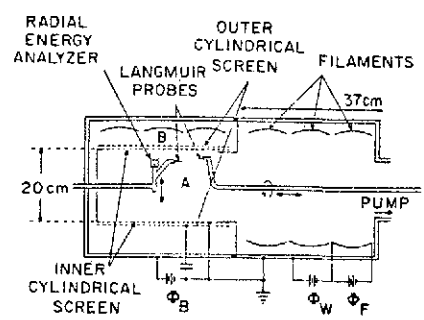

FIG. 1. Cylindrical DP device with two insulated concentric plasmas. The inner plasma is produced in the right half of the device. Beam energy is controlled by varying Φ_B. Φ_F, filament supply voltage; Φ_W filament-to-wall voltage; Φ_B, applied bias voltage. $T_e = 1.0$ eV; $T_i \lesssim 0.2$ eV; $N_0 = 10^8$–10^9 cm^{-3}; pressure, 2×10^{-4} Torr.

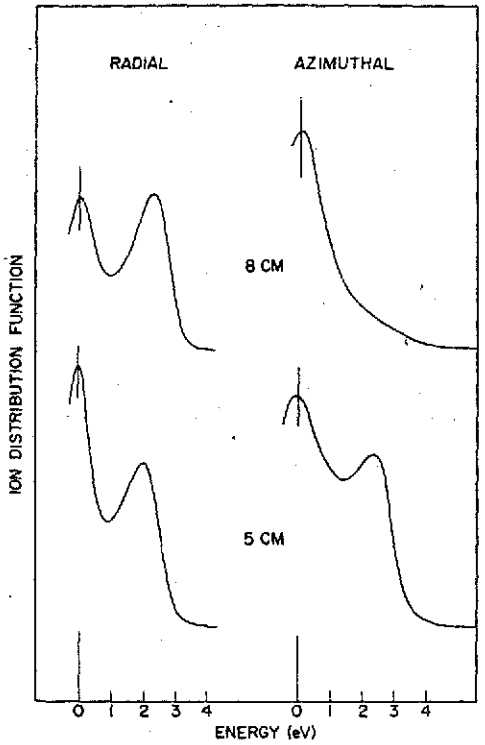

FIG. 2. Typical radial and azimuthal energy-analyzer traces at 5 and 8 cm are shown. Similar traces are observed for radii less than 6 cm indicating the presence of a ring distribution function in velocity space. The absence of an azimuthal beam at 8 cm is apparent. Azimuthal traces are found to be independent of φ. Broadening of these traces is instrumental.

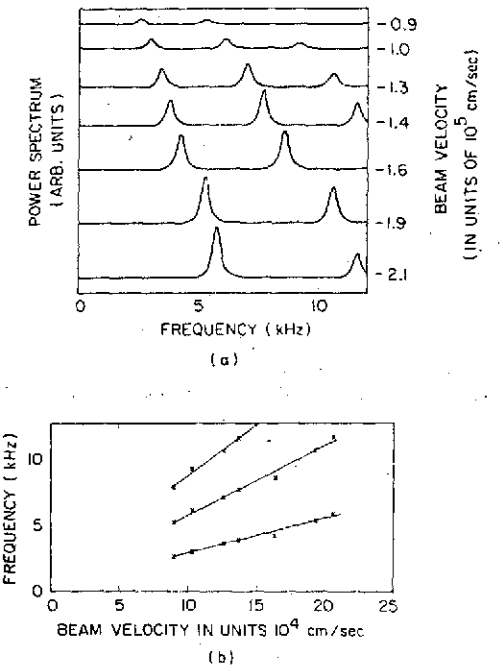

FIG. 3. (a) Power spectra showing the first three harmonics as a function of beam velocity. (b) Frequency versus beam velocity for the three lowest harmonics. No growing modes are observed for $v_b < 0.9 \times 10^5$ cm/sec and for $v_b > 2.2 \times 10^5$ cm/sec.

er than 1, whose radial coordinates can be varied. One energy analyzer measures the energy distribution function of particles with velocities in the radial direction, another observes the energy in the φ direction. A third measures outgoing energy distribution functions in the outer plasma (region B in Fig. 1). Typical energy-analyzer traces are shown in Fig. 2. Near the inner screen the beam is seen to be radial. For radii less than 7 cm we find approximately equal radial and azimuthal beam components, indicating that the beam forms a ring in velocity space. The spatial region over which the ring distribution function exists is determined by the beam velocity, and the separation and mesh size of the two concentric screens. The region increases for smaller energies. The presence of a ring distribution function rather than a purely radial beam results in a uniform beam density ($r < 7$ cm) with no steady-state electric field. This facilitates a theoretical description of the instability.

Instabilities are detected by positively biased Langmuir probes oriented in the axial direction and by the energy analyzers. One Langmuir probe is variable in the radial direction and the other is variable in the φ and axial directions. Langmuir probes indicate that relatively uniform background plasma and beam densities are achieved in this device. Langmuir-probe measurements within the inner cylinder (region A in Fig. 1) showed no φ or z dependence (except near the cylinder ends).

A comparison of signals simultaneously obtained at different positions showed that the instability was *in phase* throughout the inner plasma, demonstrating that standing waves were produced. Therefore it is meaningful to consider power spectra. Typical instability power spectra as a function of beam velocity are shown in Fig. 3(a). For high beam velocities we observe *no instability*. The onset of the instability is seen for a beam energy of approximately 1.0 eV. For beam energies less than approximately 0.2 eV the instability disappears. As the plasma potential of the outer plasma is made less than the potential of the inside plasma we observe incoherent instabilities between the outer cylindrical

screen and the outer walls of the chamber (region B in Fig. 1).

Measurements of the power spectra in the radial direction show that the three lowest frequencies correspond to resonant modes with no nodes, one cylindrical node, and two cylindrical nodes, respectively, further demonstrating cylindrical standing waves. Figure 3(b) shows that ω is roughly proportional to v_b for the first three harmonics. In addition, the second and third harmonics have approximately 2 and 3 times the frequency of the first. This suggests that $\omega/k_n = \alpha v_b$, with α constant, describes all three modes, with k_n varying approximately with the mode number.

These results can be understood by considering the linear Vlasov equation in cylindrical geometry. The Vlasov equation can be written for one component (ions or electrons) in the following way:

$$\frac{\partial f}{\partial t} + v_r \frac{\partial f}{\partial r} + v_\varphi \frac{\partial f}{r\,\partial \varphi} + \left(\frac{e}{m}E_r + v_\varphi^2 r^{-1}\right)\frac{\partial f}{\partial v_r} + \left(\frac{e}{m}E_\varphi - v_r v_\varphi r^{-1}\right)\frac{\partial f}{\partial v_\varphi} = 0. \tag{1}$$

For a stationary homogeneous equilibrium distribution $f_0(r, v_r, v_\varphi)$ with $\vec{E}=0$, we find $v_\varphi r^{-1}(v_\varphi\,\partial f_0/\partial v_r - v_r\,\partial f_0/\partial v_\varphi)=0$. This means that the zeroth-order distribution function depends only on the magnitude of the velocity, $f_0 = f_0(v) = f_0[(v_r^2+v_\varphi^2)^{1/2}]$; i.e., the distribution is *concentric* in velocity space and the beam must be a ring. Experimentally, we find such a distribution function extending from the center to within 3 cm of the inner screen for beam energies less than 2 eV.

Perturbing the plasma, we write $f(\vec{r}, \vec{v}, t) = n_0 f_0(v) + f_1(\vec{r}, \vec{v}, t)$, where $f_1(\vec{r}, \vec{v}, t)$ is given by

$$f_1(\vec{r}, \vec{v}, t) = \int_0^t dt_0\, \nabla\Phi(\vec{r}_0(\vec{r}, \vec{v}, t-t_0), t_0)\cdot \partial f_0(v)/\partial \vec{v}, \tag{2}$$

with Φ being the electrostatic potential. The time integral is taken along the straight-line orbits of the unperturbed state. In evaluating the time integral we consider the plane-propagating waves $\Phi(\vec{r}, t) = \Phi_0 \exp[i(ax+by-\omega t)] = \Phi_0 \exp\{i[kr\cos(\varphi-\alpha)-\omega t]\}$. Then the integral in Eq. (2) can be performed to give

$$f_1(\vec{r}, \vec{v}, t) = \frac{e}{m}\Phi(\vec{r}, t)\frac{kv\cos(\theta-\alpha)}{kv\cos(\theta-\alpha)-\omega}\frac{\partial f_0(v)}{v\,\partial v}. \tag{3}$$

In writing Eq. (3) and the potential we have used the following definitions:

$$x = r\cos\varphi, \quad y = r\sin\varphi, \quad v_x = v\cos\theta, \quad v_y = v\sin\theta, \quad a = k\cos\alpha, \quad b = k\sin\alpha.$$

When calculating the density from Eq. (3) by integrating over v and θ, we note that the dependence of $\cos(\theta-\alpha)$ on α can be suppressed because θ is integrated over all angles. Thus we obtain for the density

$$n(\vec{r}, t) = \int_0^\infty v\,dv \int_0^{2\pi} d\theta\, f_1 = (e/m) n_0 \Phi(\vec{r}, t) k^2 G(\omega/k, f_0), \tag{4}$$

with

$$G\left(\frac{\omega}{k}, f_0\right) = k^{-2}\int_0^\infty v\,dv \int_0^{2\pi} d\theta \frac{\cos\theta}{\cos\theta - \omega/kv}\frac{\partial f_0(v)}{v\,\partial v}. \tag{5}$$

In order to express the density in cylinder functions we let Φ_0 depend on α, $\Phi_0(\alpha) = (\Phi_\nu/\pi)\exp(i\nu\alpha - \nu\pi/2)$, and integrate over α. A change of the variable α to $w = A+\varphi$ and an appropriate extension of the limits of the integral to infinity produces the integral representation of the Hankel or Bessel functions $Z_\nu(kr)\exp(i\nu\varphi)$. Thus we can write

$$n(r, t) = (e/m)\Phi_\nu Z_\nu(kr)\exp(i\nu\varphi) G. \tag{6}$$

The densities have to be inserted into Poisson's equation,

$$-\nabla^2\Phi = 4\pi\textstyle\sum_j e_j n_j. \tag{7}$$

We note that $Z_\nu(kr)\exp(i\nu\varphi)$ is an eigenfunction of the Laplacian. This shows that cylinder functions are eigenfunctions of the beam-plasma system. For the boundary conditions of the experiment, $\Phi=0$ on boundary, we obtain directly $\nu=0$, $kR = \alpha_{0\mu}$, where $\alpha_{0\mu}$ is the μth zero of the Bessel function $J_0(\rho)$. It is important to notice that these are the only nonsingular solutions and they represent standing

waves. The dispersion relation is found from Eqs. (7), (6), and (5):

$$D(k,\omega)=1-\sum_j \omega_{pj} G_j = 1-\sum_j \omega_{pj}^2 k^{-2}\int_0^\infty v\,dv\int_0^{2\pi} d\theta \frac{kv\cos\theta}{kv\cos\theta-\omega}\frac{\partial f_{0j}(v)}{v\,\partial v}=0. \tag{8}$$

Note that $k=\alpha_{0\mu}/R$. k is not a *plane*-wave propagation vector.

We consider now a background plasma with Maxwellian ion and electron distributions with $T_e \gg T_i$. In addition we have a radial influx of ions of velocity v_b, which can approximately be described by $f_b(v)=(n_b/2\pi v_b)\delta(v-v_b)$. From the Penrose criterion it follows that for small v_b the system is stable as well as for very large v_b. Both effects have been observed experimentally [compare Fig. 3(b)]. From the assumed distribution functions we find for very small ion beam density ($\eta \ll 1$) and for $v_b \neq (kT_e/m_i)^{1/2} \equiv c_s$

$$\omega = +kv_b\left[1+\tfrac{1}{2}\eta^{2/3}\exp(2\pi i/3)c_s^{4/3}(v_b^2-c_s^2)^{-2/3}\right].$$

For the case of resonance ($v_b = c_s$) we find $\omega = +kv_b\left[1+\tfrac{1}{2}\eta^{2/5}\exp(2\pi i/5)\right]$. The experimental proportionality of ω with v_b is evident from Fig. 3(b) which corresponds to $\eta \approx 0.2$.

In conclusion we have shown that low-frequency cylindrical standing waves which depend only on r are produced by the ion-ion beam instability in a cylindrical DP device. We have shown that their frequency is roughly proportional to the beam velocity. We believe that this is the first time that a coherent ion-ion beam instability has been observed. We ascribe this to the high symmetry of the experiment which substantially reduces the off-axis modes. We have derived a dispersion relation for the coherent cylindrical-standing-wave instability from the appropriate Vlasov equations for the cylindrical geometry. This predicts unstable standing waves with ω/k_n proportional to v_b rather than traveling waves.

We are indebted to David Montgomery for advice, assistance, and enlightening discussions. We are grateful to Professor I. Alexeff for a very thorough and critical discussion of this paper. We would like to acknowledge helpful discussions with Professor G. Joyce. In addition we thank Alfred Scheller for construction of much of the apparatus.

---

*Present address: Department of Physics, University of California, Los Angeles, Calif. 90024.

†Work supported in part by the National Aeronautics and Space Administration under Grant No. NGL-16-001-043.
‡Work supported in part by the U. S. Atomic Energy Commission under Contract No. AT(11-1)-2059.
§Work supported in part by the National Science Foundation under Grant. No. GA-31676.

[1]R. J. Taylor, D. R. Baker, and H. Ikezi, Phys. Rev. Lett. 24, 206 (1970).
[2]R. J. Taylor, K. R. MacKenzie, and H. Ikezi, Rev. Sci. Instrum. 43, 1675 (1972).
[3]A. Y. Wong and R. W. Means, Phys. Rev. Lett. 27, 973 (1971).
[4]R. A. Stern and J. F. Decker, Phys. Rev. Lett. 27, 1266 (1971).
[5]R. J. Taylor and F. V. Coroniti, Phys. Rev. Lett. 29, 34 (1972).
[6]B. D. Fried and A. Y. Wong, Phys. Fluids 9, 1084 (1966).
[7]T. M. O'Neil and J. H. Malmberg, Phys. Fluids 11, 1754 (1968).
[8]D. W. Forslund and C. R. Shonk, Phys. Rev. Lett. 25, 281 (1970).
[9]S. Abas and S. P. Gary, Plasma Phys. 13, 262 (1971).
[10]R. W. Means, F. V. Coroniti, A. Y. Wong, and R. B. White, Phys. Fluids 16, 2304 (1973).
[11]N. Hershkowitz and T. Romesser, Phys. Rev. Lett. 32, 581 (1974).